SCIENCE CHINA
Chemistry

•INVITED REVIEWS•

November 2024 Vol.67 No.11: 3515–3577
https://doi.org/10.1007/s11426-024-2218-8

Recent progress of radionuclides separation by porous materials

Yinghui Xie[1,2,3], Long Yu[1], Long Chen[4], Cheng Chen[5], Li Wang[6], Fenglei Liu[2], Yun Liao[7], Peng Zhang[8], Tao Chen[9], Yihui Yuan[10], Yuexiang Lu[11], Boyang Huang[12], Hui Yang[3*], Suhua Wang[1*], Shuao Wang[4*], Lijian Ma[5*], Feng Luo[6*], Yunhai Liu[6*], Baowei Hu[2*], Hongqing Wang[7*], Duoqiang Pan[8*], Wenkun Zhu[9*], Ning Wang[10*], Zhe Wang[11*], Liang Mao[12*], Shengqian Ma[13*] & Xiangke Wang[1,3*]

[1]*Guangdong Provincial Key Laboratory for Green Agricultural Production and Intelligent Equipment, School of Environmental Science and Engineering, Guangdong University of Petrochemical Technology, Maoming 525000, China;*
[2]*School of Life Science, Shaoxing University, Shaoxing 312000, China;*
[3]*College of Environmental Science and Engineering, North China Electric Power University, Beijing 102206, China;*
[4]*State Key Laboratory of Radiation Medicine and Protection, School for Radiological and Interdisciplinary Sciences (RAD-X) and Collaborative Innovation Center of Radiation Medicine of Jiangsu Higher Education Institutions, Soochow University, Suzhou 215123, China;*
[5]*College of Chemistry, Sichuan University, Chengdu 610064, China;*
[6]*School of Chemistry and Materials Science, East China University of Technology, Nanchang 330013, China;*
[7]*School of Chemistry and Chemical Engineering, University of South China, Hengyang 421001, China;*
[8]*Frontiers Science Center for Rare Isotopes, Lanzhou University, Lanzhou 730000, China;*
[9]*State Key Laboratory of Environment-friendly Energy Materials, National Co-innovation Center for Nuclear Waste Disposal and Environmental Safety, Sichuan Civil-military Integration Institute, School of National Defence & Nuclear Science and Technology, Southwest University of Science and Technology, Mianyang 621010, China;*
[10]*State Key Laboratory of Marine Resource Utilization in South China Sea, Collaborative Innovation Center of Marine Science and Technology, Hainan University, Haikou 570228, China;*
[11]*Institute of Nuclear and New Energy Technology, Tsinghua University, Beijing 100084, China;*
[12]*State Key Laboratory of Pollution Control and Resource Reuse, School of the Environment, Nanjing University, Nanjing 210093, China;*
[13]*Department of Chemistry, University of North Texas, Denton, TX 76201, USA*

Received May 30, 2024; accepted July 23, 2024; published online September 26, 2024

The separation of radionuclides is critical for the sustainable development of nuclear energy. It is urgent to design and prepare functionalized materials for efficient radionuclides separation. Porous materials are considered excellent candidates for the separation of radionuclides under complex conditions due to their high specific surface areas, tunable pore structures and controllable functionalities. In this review, we summarized the design, preparation and functionalization of porous materials and their application for separation of radionuclides in the past five years, discussed the separation performance and analyzed the structure-activity relationship between various radionuclides and porous materials, and systematically clarified their characterization and mechanism of different type porous materials. We also introduced the detection, irradiation and chemical toxicity of different reflective radionuclides.

porous materials, radionuclides, detection, separation, radiotoxicity, interaction mechanism

Citation: Xie Y, Yu L, Chen L, Chen C, Wang L, Liu F, Liao Y, Zhang P, Chen T, Yuan Y, Lu Y, Huang B, Yang H, Wang S, Wang S, Ma L, Luo F, Liu Y, Hu B, Wang H, Pan D, Zhu W, Wang N, Wang Z, Mao L, Ma S, Wang X. Recent progress of radionuclides separation by porous materials. *Sci China Chem*, 2024, 67: 3515–3577, https://doi.org/10.1007/s11426-024-2218-8

*Corresponding authors (email: h.yang@ncepu.edu.cn; wangsh@gdupt.edu.cn; shuaowang@suda.edu.cn; ma.lj@hotmail.com; ecitluofeng@163.com; yhliu@ecut.edu.cn; hbw@usx.edu.cn; hqwang2001cn@126.com; panduoqiang@lzu.edu.cn; zhuwenkun@swust.edu.cn; wangn02@foxmail.com; wang2023@tsinghua.edu.cn; lmao@nju.edu.cn; shengqian.ma@unt.edu; xkwang@ncepu.edu.cn)

CONTENTS

1 Introduction

Nuclear energy, as a safety, clean, economical and reliable energy, plays an important role in building low-carbon emission and efficient energy systems [1]. Effectively solving the two problems of front uranium fuel supply and tail spent fuel reprocessing is a key way to ensure the sustainable development of nuclear energy [2,3]. The proven uranium reserves on land cannot meet the demand for nuclear power generation for a long time, which has become one of the main factors restricting the sustainable development of nuclear energy [4]. In addition, the rapid development of nuclear power inevitably leads to a sharp increase in the total amount of spent fuel, and the separation of valuable radionuclides is of great significance for improving the utilization of nuclear resources [5,6]. It is of great scientific significance to develop the technology of uranium extraction from seawater and the separation of useful radionuclides from spent fuel [7]. The concentration of uranium in seawater is about 3.3 ppb, and there are large numbers of competitive ions and marine microorganisms. Thereby, the development of high selectivity, high extraction efficiency, effective resistance to marine biological fouling, and low-cost seawater uranium extraction technology are crucial to meet the actual application requirements [8,9]. Revealing the interaction mechanism between the structures of functional materials and uranyl ions clarifies the influencing factors and the structure-activity relationship, which is important to guide the design and synthesis of new porous materials and optimize the process of uranium extraction from seawater [10,11]. In the spent fuel reprocessing process, high acidity, irradiation and ionic strength bring many difficulties to the separation of radionuclides in the reprocessing process [12]. The selective separation of target radionuclides has the following difficulties and challenges, *i.e.*, to overcome the problems of poor selectivity, slow adsorption rate and low adsorption capacity in complex environments such as high acid, alkali and ionic strength, and to achieve selective separation of radionuclides [13]. Moreover, nuclear accidents cause leakage of radionuclides, and they have chemical toxicity and radiotoxicity, which enter the ecosystem through environmental migration processes and cause long-term harm to soil, water, atmosphere and human health [14,15]. In general, actinide elements and long-lived fission products are the core scientific problems of nuclide separation (Figure 1). Their position in the periodic table determines the physicochemical properties of the elements, which is important to guide the synthesis of porous materials for nuclide separation.

It has become a focus of research to develop efficient and operable methods for the separation of radionuclides [16,17]. At present, the methods for radionuclide separation include adsorption [18–22], solid phase extraction [23], ion exchange [24–26], electrochemistry [27–29], photocatalysis [30], and biological treatment [31,32]. In addition, the combination of multiple methods, such as adsorption-photocatalysis and adsorption-electrocatalysis [33–36], firstly captures the target ions, then catalyzes for conversion of the radionuclides and provides a new path for the separation of radionuclides. Extracting target nuclides from the complex environment requires the design of novel functional materials with high adsorption capacity, selectivity, reusability and stability. Traditional materials are difficult to be used for efficient separation of nuclides owning to the poor porosity, low capacity and selectivity [37]. In recent years, porous materials have been widely studied for the separation of radionuclides due to their large specific surface area, adjustable pore size, high adsorption capacity and specific functional groups [38–40]. Metal-organic frameworks (MOFs) [41–44], covalent organic frameworks (COFs) [45–

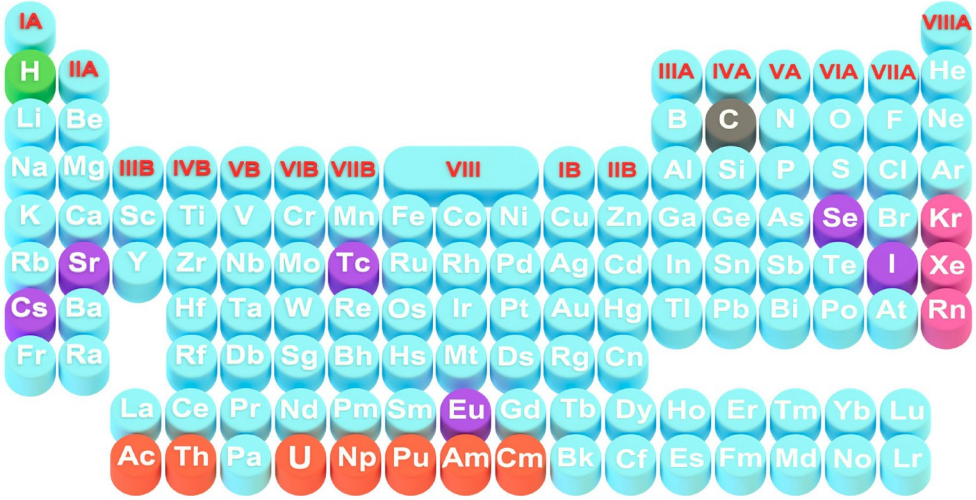

Figure 1 Actinides and long half-life fission products in the periodic table of elements (color online).

53], porous organic polymers (POPs) [54–57], graphene-based materials [58], porous carbon [59,60], carbon quantum dots (CQDs) [61–63], graphitic carbon nitride (g-C_3N_4) [64,65], MXenes [66,67] and biomimetic materials (BIMs) [68,69] have been developed for radionuclides extraction. Through careful structural design, it has special physical and chemical properties to enhance the uptake of target radionuclides, which provides a new solution for radionuclides separation.

Recently, the extraction of radionuclides by novel porous materials has been extensively studied and reported, but most reviews mainly focus on the separation of one kind of radionuclides or by one type of material, and systematic reviews of novel materials are still lacking on the separation of radionuclides [70–75]. In this review, we summarized the optimal design of porous materials and provided effective strategies for the efficient separation of radionuclides. We aim to cover a variety of different porous materials for radionuclides extraction, which is suitable for detecting and separating different classes of radionuclides (such as Sr, Cs, I, Kr, Xe, Tc, U), classify and summarize the design and synthesis methods of different porous materials and their performance evaluation, focusing on the key factors for the separation of target radionuclides, including (i) structural relationship between materials and target radionuclides, (ii) characterization of porous materials and evaluation of separation properties, (iii) extraction mechanism of target nuclides by porous materials. At the same time, we also discuss the effective strategies to improve the selectivity extraction of target nuclide, and to analyze the challenges and perspectives of porous materials. Moreover, we systematically describe the toxicity of different radionuclides and the degree of radiation damage to human health. We believe that it is of great significance for the long-term development of nuclear energy to review the emerging applications of new porous materials in the separation of radionuclides.

2 Radionuclide detection

Porous materials exhibit excellent optical, magnetic, electronic, physicochemical, and adsorption properties, making them widely applicable for detecting persistent pollutants, heavy metal ions, radioactive nuclides, and other environmental contaminants [67,76–78]. Among these, porous materials are primarily employed for sensing and detection applications, including MOFs, COFs, and carbon-based materials (such as graphene and CQDs) (Figure 2). Before delving into the application of porous materials in the removal of radionuclides, we will first summarize their current applications in the rapid detection of such nuclides. MOFs, which are documented for their high porosity, stability, large surface area, and tunability, have emerged as one of the most

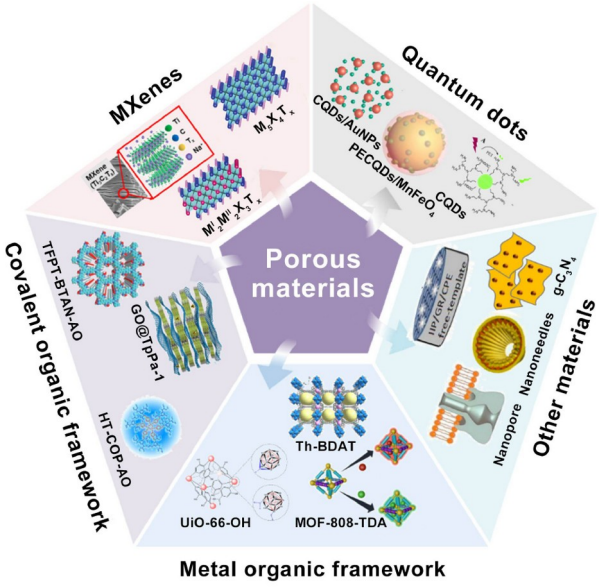

Figure 2 Common porous materials for the detection of radionuclides [61,78,79,91–98] (color online).

promising materials across various applications. Moreover, targeted MOFs can be synthesized and structurally tailored by intentionally modifying metal ions, ligands, or functional groups.

Due to these advantages, MOFs have garnered popularity across diverse research fields and have recently attracted intensive interest in the field of analytical detection (Figure 3). Ju *et al*. [79] devised a pioneering Th-based MOF (Th-MOF) for detecting radioiodine, boasting a detection limit of 1.367 μM. Following interaction with radioiodine, the luminescence quenching of Th-MOF could be discerned by the naked eye, rendering it promising for practical applications. Liu *et al*. [80] innovatively synthesized a luminescent MOF-based probe exhibiting exceptional selectivity and immunity to interference, capable of detecting Th(IV) across a wide concentration range from 24.2 μg/L to 300 mg/L.

COFs are 2D or 3D crystalline porous materials constructed from organic monomers *via* robust covalent bonds [81–83]. As porous and crystalline materials, COFs and their composites exhibit significant promise for radionuclide detection [84]. In contrast to MOFs, COFs offer atomic or molecular scale tunability and greater predictability [85]. COF-based fluorescence sensors have found widespread use in detecting heavy metal ions [86], ensuring food safety [87], identifying viruses [88], and more. Among these, the detection of radionuclides has garnered considerable attention due to their strong association with cancer. Niu *et al*. [89] synthesized a fluorescent COFs (TFPPy-BDOH) with an ultrafast fluorescence response (2 s) and an ultralow detection (8.8 nM), demonstrating its potential practical application. Cui *et al*. [90] successfully fabricated a 3D COF with

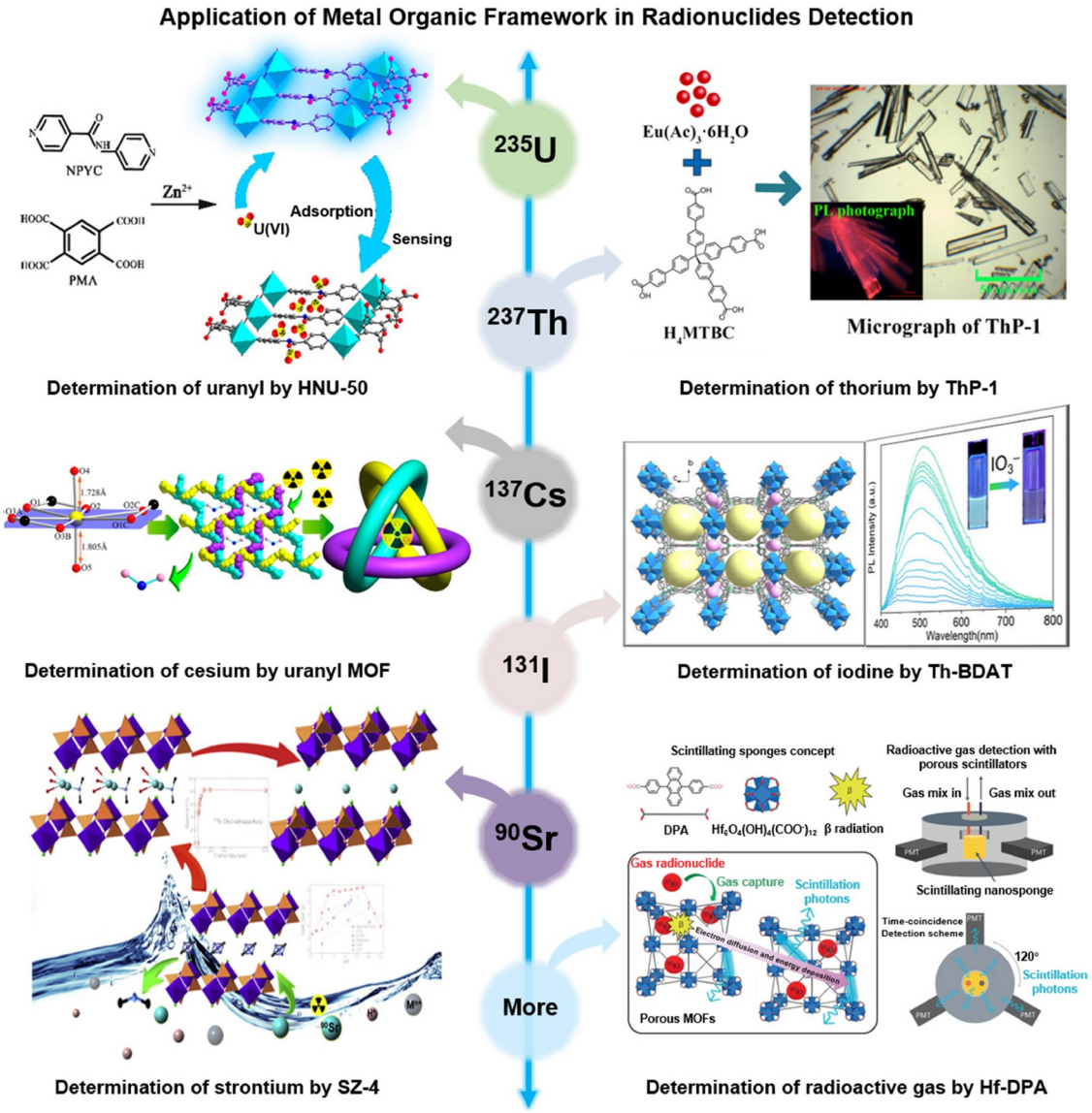

Figure 3 Application of various MOFs in radionuclides detection [79,80,109–112] (color online).

strong fluorescence and interconnected pore channels, enabling trace detection of UO_2^{2+} with a detection limit of 4.08 nM.

Carbon-based materials also provide an enticing platform for constructing innovative radionuclide detection due to their cost-effectiveness and stability [99]. Graphene, the latest generation of carbon materials, exhibits tremendous potential for radionuclide detection [100]. Lin *et al.* [101] prepared a novel graphene-based material complex (GO-UO_2^{2+}), which was capable of catalyzing the H_2O_2-TMB system to display a dark blue color, thereby establishing a sensitive uranyl sensor *via* a colorimetric method. With a detection limit of 4.7 μM, this approach was effectively applied to detect uranyl in environmental water samples. Li *et al.* [102] designed an ion-imprinted carbon material electrochemical sensor by modifying H_4L-ion polymers with graphene oxide (GO) to detect trace uranyl ions, achieving a detection limit as low as 1.32 nM. Dewangan *et al.* [103] synthesized graphene quantum dots (GQDs) for qualitative and quantitative analysis of U(VI) based on their fluorescent properties, with a detection limit as low as 1.5 ppb. The functional groups of GQDs, such as the hydroxyl groups, bind with U(VI), and the coordination is responsible for the fluorescence quenching process. 2D transition metal carbides, nitrides, and C_3N_4, collectively known as MXenes [104], represent a newly emerging class of 2D functional materials. They are considered ideal materials for nuclear wastewater treatment due to their outstanding chemical stability, high hydrophilicity, abundant surface functional sites, high resistance to intense radiation, and environmental friendliness [105,106]. Various types of MXenes with different structures have been synthesized in recent years for the

detection and selective adsorption of radionuclides, such as Sr, Th, Cs, Tc, and others [67,107]. The current study primarily focuses on the selective adsorption of various ions by MXenes. In the future, it may be possible to incorporate fluorescent materials onto MXenes to enable fluorescence-based detection and adsorption visualization, thereby allowing modified MXenes to achieve simultaneous detection and removal ability, offering significant advantages for radioactive nuclides treatment.

In addition to the aforementioned porous materials, other common materials utilized for detecting radioactive nuclides include ionic liquid membranes, nanopores, and nanoneedles. Depauw *et al*. [108] integrated calixarene sensors into microfluidic sensor chips, enabling the detection of Cs (I) ions in water samples at parts per billion (ppb) levels. Roozbahani *et al*. [91] developed a fast, real-time, and label-free nanopore sensor for Th(IV) detection. The aspartic acid-containing peptide was used as a chelating agent to adjust the electrolyte solution pH to control the net charge of the peptide ligand and its metal ion complexes. This method exhibited high sensitivity with a detection limit of 0.45 nM. Gomaa *et al*. [92] designed a novel fluorescent ligand named CFBS, which was grafted onto mesoporous γ-Al_2O_3 nanoneedles (CFBS@AlNNs). Fluorescence detection of Th(IV) ions using CFBS-ligands achieved a detection limit as low as 0.19 ppm. Despite the effectiveness of these methods, MOFs remain the most widely investigation and utilization. Therefore, we specifically examine the applications of MOFs in various radionuclide detections, including uranium, iodine, thorium, cesium, and strontium.

2.1 Detection of uranium (UO_2^{2+}) by rare-earth MOFs

Uranium, a major naturally occurring radionuclide, is utilized as a crucial raw material for various sectors within the nuclear industry, encompassing nuclear energy, weaponry, and medicinal applications [113,114]. However, due to unsustainable exploitation, nuclear waste from power plants and incidents such as nuclear accidents, radioactive and toxic uranium gradually leak into water, soil, and atmosphere, ultimately entering the biosphere and posing a significant threat to human health [115,116]. Uranium chemical and radiological toxicity can result in damage to the kidneys, lungs, liver, and potentially skeletal effects [117]. Uranium can exist in four oxidation states in aqueous solution, including +3, +4, +5, and +6, with uranyl (UO_2^{2+}) being the most common and stable species [118]. The U.S. Environmental Protection Agency (USEPA) mandates a maximum uranium content of 1.3×10^{-7} mol/L in drinking water to safeguard environmental and human health [119]. Hence, rapid and sensitive detection of uranium is paramount for ensuring environmental and human safety.

In recent years, porous materials have provided researchers with significant opportunities to detect and remove uranyl ions effectively. Li *et al*. [120] prepared a europium MOF (Eu-MOF) using a one-step hot solvent method. The Eu-MOF demonstrated characteristic fluorescence of trivalent Eu^{3+}, which was remarkably quenched by the combination of uranyl ions and the abundant nitrogen atoms in ligands. The detection limit for uranyl ions using the Eu-MOF was 0.9 μM. Chen *et al*. [121] synthesized a robust 3D pcu Co(II) MOF with exposed pyramidal Lewis base sites, which emitted light and could be quenched by low-concentration uranyl ions, with a detection limit of 0.7 μM. This study demonstrated the practical application of MOF-based fluorescent sensors through ligand tailoring to achieve low detection limits. To further improve the sensitivity, Hou *et al*. [122] successfully prepared a carboxyl-functionalized Zn(II) MOF, which was capable of sensing UO_2^{2+} in aqueous solutions through fluorescence quenching for resonance energy transfer, achieving a detection limit of 0.4 μM. Similarly, Qin *et al*. [110] synthesized a fluorescent zinc-based MOF (HNU-50) for simultaneous detection and removal, with fluorescence quenching resulting from U(VI) adsorption, allowing for more selective and sensitive detection of UO_2^{2+} with a detection limit of 1.2×10^{-8} M (12 nM). Furthermore, Zhang *et al*. [123] successfully developed a MOF-based ratiometric fluorescent sensor incorporating Eu(III), which exhibited excellent turn-on fluorescence sensing for uranyl ions with a limit of detection at 3 nM, significantly lower than the standard level for drinking water. In addition, the probe also demonstrated high selectivity for UO_2^{2+} even in the presence of multiple environmental interfering substances.

Meanwhile, MOFs can be combined with other materials to improve and enhance their sensing performance. For example, to address the weak affinity of Au atoms for uranyl, Wang *et al*. [115] modified ZIF-8 porous structures onto a magnetic surface-enhanced Raman spectroscopy (SERS) substrate, resulting in a magnetic MOF substrate which was capable of detecting uranyl and removing radioactive substances. It has been shown that the addition of ZIF-8 coating had minimal impact on the detection performance, maintaining a detection limit of 5×10^{-9} M (0.5 nM).

2.2 Detection of iodine by bifunctional MOFs

During nuclear fuel cycle reprocessing, numerous iodine isotopes are emitted, notably short-lived ^{131}I and long-lived ^{129}I [52,124]. The iodine isotope ^{129}I, characterized by its significantly extended half-life, poses considerable toxicity, particularly in the form of anionic iodate ions (IO_3^-), which are extremely water-soluble and mobile in aquatic environments [125]. Radioactive iodine can exert long-term impacts on soil and water within the environment. Moreover, it can accumulate in the thyroid gland, directly affecting human

metabolic processes and potentially causing thyroid cancer [126]. Consequently, it is urgent and imperative to develop rapid detection methods for radioactive iodine.

In recent years, numerous researchers have utilized MOFs to develop fluorescent probes or components for electrochemical sensors, enabling rapid and sensitive detection of radioactive iodine [79,127–129]. Based on previous studies, Ju *et al*. [79] utilized actinide to hydrothermally synthesize a Th-based MOF (Th-BDAT), serving as a bifunctional platform for both iodide ion adsorption and iodate detection. Th-BDAT conjugated aromatic π-electrons and high porosity facilitate electron transport between host and guest, thereby increasing iodine adsorption capacity. The abundant coordination geometry of Th^{4+} and the availability of 5f orbitals enable the creation of diverse topologies, offering it remarkable photo-switching capabilities for iodate detection *via* fluorescence burst, achieving a detection limit of 1.367 μM. Small *et al*. [130] coated ZIF-8 onto a platinum cross-electrode to develop a solid-state sensor with a direct electrical response to iodine gas. This all-solid-state sensor device exhibited a prolonged signal lifespan [131]. They evaluated the sensor sensitivity and structural integrity under various temperature and duration time conditions. It has been demonstrated that a change in impedance of at least 10^5 upon exposure to I_2 was observed. The MOF-based sensors showed exceptional selectivity and low reaction time under all conditions and variables, enabling direct electrical detection of the target gas.

2.3 Detection of thorium by La-based MOFs

Thorium (Th), a naturally occurring radioactive heavy metal, finds common use in gas hoods, kerosene lamps, welding operations, and refractory materials. It is also considered a potential nuclear fuel for molten salt reactors [93,132,133]. However, significant quantities of radioactive thorium waste, which is predominantly in the form of Th(IV), are often released into the environment during mining and processing, leading to Th(IV) contamination [134]. This contamination poses a threat to human health through ecological cycles or the food chain. Research has shown that Th(IV), when inhaled or ingested, can cause liver and lung diseases, urinary tract disorders, or various types of cancers, highlighting the importance of detecting and monitoring Th(IV) content in the environment [135–137].

Song *et al*. [138] successfully synthesized a 3D luminescent lanthanide organometallic framework (compound **1**), which showed excellent water stability and sensitivity for detecting Th(IV) ions. Compound **1** exhibited high stability even in low-pH systems. The sensitive response to Th(IV) was mainly achieved through direct interaction with the emission center, inducing energy transfer and competitive absorption of excitation light, with a detection limit of 3.49×10^{-5} mol/L. Meanwhile, complete adsorption of Th (IV) was also achieved during the detection process. Liu *et al*. [80] utilized rare earth elements (Eu(III)) to prepare a self-calibrating fluorescent probe (ThP-1). This probe effectively eliminated measurement interference caused by internal factors, enabling sensitive detection of Th(IV) within a wide range concentration (24.2 μg/L–300 mg/L) and achieving a detection limit of 24.2 μg/L. This limit was far lower than the maximum contamination standard for Th (IV) in drinking water (246 μg/L) regulated by the World Health Organization (WHO) [139]. The selective uptake and efficient enrichment of Th(IV) were elucidated by intrasphere coordination between the ThP-1 backbone and Th (IV) through XAS and DFT calculations.

2.4 Detection of cesium by In-based MOFs

Cesium (^{137}Cs), a radioactive thermal radiation element, represents one of the primary sources of contamination in nuclear waste. It emits strong β-γ radiation with a half-life period of 30.17 years and a high fission rate (6.3%) [70,140]. Moreover, Cs^+ exhibits chemical properties similar to Na^+ and K^+, enabling it to block Na^+/K^+ channels or gradually accumulate in the soft tissues of animals, leading to kidney, central nervous system, or liver damage [141]. Hence, it is urgent to develop a convenient way to monitor and detect Cs (I) rapidly.

Gao *et al*. [142] successfully synthesized an In-MOF (FJSM-InMOF) with exceptional resistance to β and γ radiation. This material could be easily prepared *via* a one-step solvent-thermal method and exhibited a high ion-exchange capacity. Investigations into the ion exchange mechanism revealed a single-crystal to single-crystal structural transition of the material during Cs^+ ion exchange, facilitating the potential detection and adsorption of Cs^+ *via* ion exchange. The FJSM-InMOF has demonstrated a maximum adsorption capacity of 198.63 ± 10.62 mg/g and exhibited high selectivity for Cs^+ adsorption, even in the presence of NaCl and $NaNO_3$, establishing a solid foundation for the development of environmentally friendly Cs^+ detection and capture methods.

2.5 Detection of strontium and radioactive gas by oxidic MOFs

Strontium (^{90}Sr) is one of the main radioisotopes with a half-life period of 28.9 years, and ranks among the primary radioisotopes in nuclear waste [77]. It stands as a major source of radioactive toxicity in nuclear fuel and was notably released into seawater during the Fukushima accident in 2011. Zhang *et al*. [109] found an unusual oxidic ion-exchange material, SZ-4, which effectively detected and removed ^{90}Sr in acidic solutions and seawater. The SZ-4

exhibited a distinctive two-step intercalation mechanism, revealing a novel type of selectivity towards soft cations, which was used as a soft N-donor ligand through the collaborative coordination of the oxide layer and the dimethylamine intermediate layer.

Anthropogenic radionuclides stemming from fission (^{133}Xe and ^{85}Kr) and activation (^{3}H) products demand careful and continuous monitoring. Orfano *et al*. [112] demonstrated the capability of Hf-based MOFs containing DPA as a scintillating ligand for gas-radioactivity detection. These MOFs displayed rapid scintillation, a fluorescence yield of approximately 40%, and accessible porosity suitable for hosting inert gas atoms and ions. The device based on MOF material exhibited excellent sensitivity in the detection and adsorption of ^{85}Kr, ^{222}Rn, and ^{3}H radionuclides, surpassing the limits of commercial systems. Furthermore, Mauree *et al*. [143] proved that MOFs could serve as a highly effective material for detecting radioactive gases and could be utilized as both porous gas sponges and scintillators. A unique TDCR was established to test the three most crucial radioactive gases (^{85}Kr, ^{222}Rn, and ^{3}H), offering a practical solution to the challenge of radioactive gas measurements and outperforming commercial detectors with its compact, cost-effective, and easy-to-handle architecture.

From this, it can be inferred that the current applications of porous materials in radioactive nuclide detection are still evolving, and there is ample room for advancement. Integrating the capabilities of existing porous materials for removing radioactive nuclides can offer valuable insights for further enhancing the sensitivity and selectivity of nanoscale porous probes in the future.

3 MOFs for radionuclides separation

The effective management and remediation of uranium (U), thorium (Th), and their fission products, including cesium (Cs), strontium (Sr), technetium (Tc), iodine (I), krypton (Kr) and xenon (Xe) are crucial for ensuring the safe running of nuclear reactors and reprocessing of spent fuel. MOFs constructed from inorganic metal ions or metal oxide clusters with various organic building blocks, have attracted significant concern for their potential in efficient separation of the abovementioned radionuclides. This interest stems from their high specific surface area, finely adjustable pore size, and favorable chemical stability. Chemical modifications and charge adjustments impart pristine MOFs and MOF-based composite materials with exceptional adsorption capacity and selectivity. In this section, we highlight representative works on functional MOFs for radionuclides capture since 2019, summarizing both the adsorption performances and interaction mechanisms.

3.1 Uranium

The construction of MOF materials for selective extraction of U(VI) from seawater is pivotal to supplying the strategic element. Inspired by the spatial structures in superb-uranyl binding protein, Yuan *et al*. introduced 4-aminoisophthalic acid into UiO-66 and constructed selective nano-pockets for uranyl capture (Figure 4a). Given the carboxyl and amino groups in the confined pores, the MOF shows an adsorption capacity of 6.85 mg/g from natural seawater (Figure 4b) [144]. Two years later, the same group fabricated an adaptive nanocage for U(VI) extraction by a MOF *via in-situ* molecular imprinting. Due to the combination of the coordination interaction of four oxygen atoms in the material with U(VI) and the hydrogen bonds between the phenolic hydroxyl groups and axial oxygens of uranyl, the adsorbent demonstrates an enhanced adsorption capacity of 7.35 mg/g for U(VI) from seawater [145]. Apart from pristine MOFs, Wang's group [146] at Hainan University also prepared a MOF-based composite for U(VI) extraction from seawater. They elaborately synthesized a cellulose nanofiber aerogel anchored with the UiO-66-NH_2/black phosphorus quantum dots heterojunctions (BP@CNF-MOF). The good photocatalytic activity not only provides a decent adsorption capacity of 6.77 mg-U per g-Ads *via* uranyl reduction, but also endows it with excellent antibacterial properties due to the *in-situ* generation of reactive oxygen species.

U(VI) capture is also significant for environmental protection. Wang's group [147] at Soochow University synthesized a rare polyoxometalate (POM)-organic framework (SCU-19) for the efficient removal of uranyl with three synergic mechanisms of ligand complexation, chemical reduction and photocatalytic reduction (Figure 4c). With the rational screening of five phenolic hydroxyl group-containing organic ligands, Luo's group [148] proved that 1,3,5-triformylphloroglucinol exhibited extraordinary U(VI) removal performance with *in-situ* formation of π-f conjugated 2D uranium-organic framework (Figure 4d). 1,3,5-Triformylphloroglucinol can extract U(VI) from high and low uranyl solutions (50 or 1 ppm) to below 0.15 ppb. The excellent removal depth is also evidenced by the 97% uranyl trap from natural seawater with an unprecedented removal efficiency of 0.64 mg/(g d). In addition, the high binding affinity endows the superior separation selectivity in a mixed solution containing 21 competitive ions. *Via* a post-modification approach, Diwu's group [149] synthesized UiO-66-$(COOH)_4$-180 with a high density of carboxyl groups. Due to the partial accumulation of this MOF material in kidneys and femurs, UiO-66-$(COOH)_4$-180 can remove 55.4% and 36.5% uranyl in two organs respectively by *in-vivo* mice experiments.

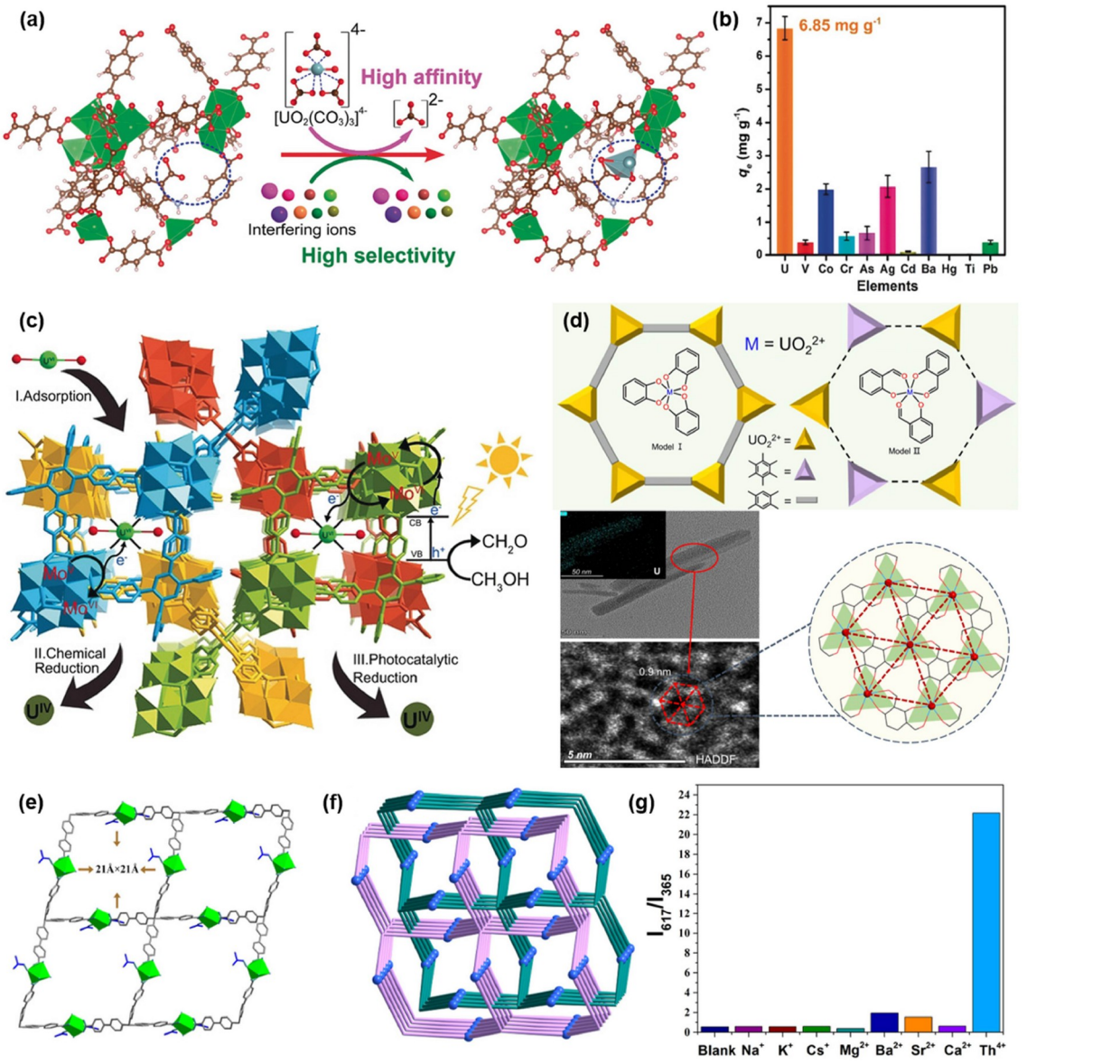

Figure 4 (a) The selective capture of uranyl in the nano-pocket in MOFs. (b) Uranyl selectivity in natural seawater [144]. (c) The synergic mechanisms of adsorption, chemical reduction and photocatalytic reduction for uranyl separation by SCU-19 [147]. (d) The proposed structure of 2D uranium-organic framework and TEM-HADDF images of UOF-TFP [148]. (e) Single layer of the structure of ThP-1 and (f) topological structure. (g) luminescence response of ThP-1 [80] (color online).

3.2 Thorium

In 2019, Wang's group [80] prepared a luminescent Eu-based MOF material (ThP-1) for the sensitive detection of Th(IV) ions. Owing to the self-calibrated sensing approach and the inner-sphere coordination with the framework, ThP-1 shows a detection limit as low as 24.2 μg/L coupled with superior anti-interference capabilities (Figure 4e–g). Sun's group [150] designed and synthesized a Zn-based 4-fold interpenetrated MOF material (**1a**) with mixed carboxyl and pyridyl-based ligands containing O^- and amide groups, respectively. On account of the high binding affinity of O^- groups with Th(IV), **1a** achieves a high uptake capacity of 165.61 mg/g and distribution coefficient of 3.16×10^5 mL/g. In addition, **1a** exhibits high selectivity to various metal ions, such as Sm(III), La(III), Ho(III), Cd(II) and K(I). Recently, Qiu *et al*. [151] developed a fluorescent MOF (DBT-DHTA-Cd) with unique thorium nanocavity traps including azole and hydroxyl groups. The synergistic effect of the appropriate pore size and dense hydroxyl-N traps results in extremely low binding energy (E_{ads} = –602.7 kJ/mol) for Th (IV). DBT-DHTA-Cd achieved fast adsorption kinetics (30 min) and rapid fluorescence response (1 min) toward Th (IV).

3.3 Strontium

In 2019, Wang's group [109] developed a layered oxidic coordination polymer SZ-4 for efficient capture of ^{90}Sr from both acidic solution and seawater with a distinct selectivity against hard cations such as H^+, Na^+, and Ca^{2+}. The ion-exchange material demonstrates an ultrahigh uptake capacity (117.9 mg/g) and elevated distribution coefficient (4.06×10^6 mL/g) (Figure 5a). The X-ray crystallography analysis combined with DFT calculations revealed a unique two-step intercalation mechanism. The conspicuous removal performance is attributed to the synergic coordination of O and F atoms in the host layer and the interlayer dimethylamine (DMA) acting as a soft N donor (Figure 5b). Peng *et al.* [152] introduced sulfate and oxalate to MOF-808, respectively. The introduction of trapping groups leads to high

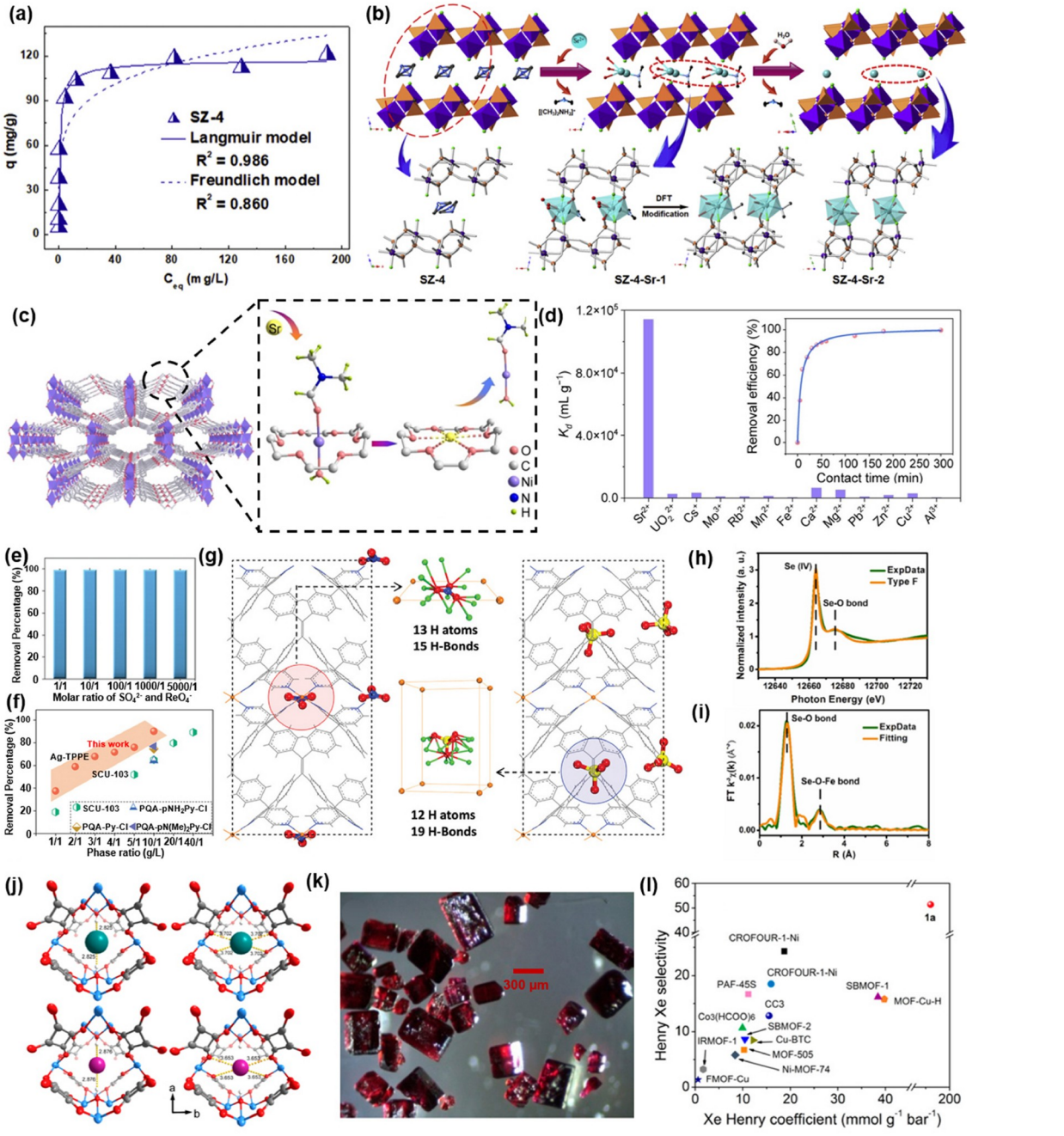

Figure 5 (a) Adsorption isotherm of Sr(II) by SZ-4. (b) The ion exchange process of Sr(II) removal by SZ-4 [109]. (c) The adsorption mechanism of Sr by MOF-18Cr6. (d) The selectivity K_d value for removing Sr(II) and inset is the removal kinetics of MOF-18Cr6 [153]. (e) Removal of TcO_4^- by Ag-TPPE in the presence of SO_4^{2-}, (f) simulated SRS tank waste, (g) DFT calculations hydrogen interaction in Ag-TPPE [44]. (h, i) XANES spectra of Fe-MIL-101-SeO_3^{2-} and the theoretical spectra of type F [155]. (j) The Xe and Kr atom interacts with H atoms from the hydroxyl group and O atoms from organic ligands. (k) Microscope images of single crystals **1a** treated at pH 1. (l) Thermodynamic Xe/Kr separation performance [156] (color online).

adsorption capacities of 176.46 and 206.34 mg/g for MOF-808-SO_4 and MOF-808-C_2O_4, respectively.

Unlike the common strategy of attaching functional groups on the pore wall, Yuan and coworkers [153] decorated 18-crown-6-ether into the channel walls of a Ni-based MOF (MOF-18Cr6), which avoids the blockage of the spatial space and facilitates the transport of metal ions (Figure 5c). Given the elaborate structural design, the 1D channel was formed by using an 18-crown 6-ether ligand as the channel wall for the separation of Sr(II). In contrast to the traditional MOFs designed by grafting functional chelating group in the framework pores, this MOF adsorbent possessed 18-crown-6-ether cavities on the channel walls as functional binding sites for strontium ions, which not only facilitated the transport and uptake of Sr(II) ions through the channels, but also prevented occlusion of the channels following the adsorption of Sr(II) ions. Consequently, the functional sites are fully utilized to achieve a high Sr(II) removal rate of 99.73% in simulated nuclear wastewater (Figure 5d). For the removal of Sr(II) from strong alkaline solutions, Wang's group [154] constructed an ultra-stable MOF material SZ-7 (SZ = Suzhou) combined with the enhanced coordination bond between zirconium and phosphonate, as well as the employment of hydrophobic phenyl groups. Thus, SZ-7 can remove Sr(II) ions from 1 M NaOH solution with a high adsorption capacity of 183 mg/g and K_d value of 3.9×10^5 mL/g.

3.4 Cesium

Due to the high affinity of ferrocyanide (FC) to Cs, Le and Cho [157] combined FC with a zeolitic imidazolate framework (ZIF-8), resulting in a composite adsorbent ZIF-8-FC. ZIF-8-FC exhibits an outstanding adsorption capacity of 422.42 mg/g, which is 15.9 times higher than that of pristine ZIF-8. In addition, Asgari *et al*. [158] synthesized a stable Nd-based MOF, which displays modest capacities of 86 and 58 mg/g for Cs^+ and Sr^{2+}, respectively.

3.5 Palladium

The extraction of palladium (Pd) from radioactive waste solution is beneficial not only for the safe processing of high-level liquid waste but also for providing another supply of Pd. Lin *et al*. [159] compared the $PdCl_4^{2-}$ adsorption performance of various Zr-based MOFs, namely MOF-802, UiO-66 and MOF-808. Among these MOFs, due to the presence of plentiful binding sites, MOF-808 shows the largest adsorption capacity of 163.9 mg/g. In addition, MOF-802 exhibits the highest adsorption affinity for low concentration of $PdCl_4^{2-}$ on account of the largest binding energy of pronated amine with $PdCl_4^{2-}$. Tang *et al*. [160] designed and prepared a new Zr-based MOF for Pd capture, in which the pre-modified ligand contains both hydroxyl and imine groups. The MOF displays a superior capacity of 242.5 mg/g, mainly attributing to the synergetic coordination and the reduction effect of the two functional groups. Hu *et al*. [161] reported rare earth elements (REEs) nanotrap that feature dense uncoordinated carboxyl groups and triazole N atoms in a two-fold interpenetrated MOF (named NCU-1). NCU-1 showed high selectivity toward light REE, a high separation factor of $SF_{Pr/Lu}$ = 796 and $SF_{Nd/Er}$ = 273. This strategy achieved efficient and selective separation of REEs from mine tailings.

3.6 Technetium

Wang's group [162] synthesized a robust SCU-102 (SCU = Soochow University) for the efficient remediation of ReO_4^-/TcO_4^-. The cationic MOF achieves a high uptake capacity of 291 mg/g for ReO_4^-. More importantly, SCU-102 can almost quantitatively remove ReO_4^- in the presence of 6,000 times SO_4^{2-}. The ultrahigh selectivity was ascribed to the hydrophobic pockets within the channels, which exhibit a higher binding energy compared with competing ions. To further improve the selectivity, Xiao's group synthesized a fourfold interpenetrated MOF material Ag-TPPE (TPPE = 1,1,2,2-tetrakis(4-pyridylphenyl)ethylene), which can be fast synthesized within 1 min at room temperature *via* mixing, stirring or sonicating. Ag-TPPE exhibits superior selectivity at 1,000-fold NO_3^- or 5,000-fold SO_4^{2-} (Figure 5e). In addition, the MOF shows an outstanding removal percentage from simulated Hanford or Savannah River Site tank waste compared with reported adsorbents at the same solid-to-liquid ratio (Figure 5f). The DFT calculations (Figure 5g) demonstrated that the extraordinary selectivity derives from the entrance of TcO_4^- into the framework by breathing effect and capture in the channel *via* multiple hydrogen bonds [44]. A cationic MOF (TJNU-216, TJNU = Tianjin Normal University) synthesized by Du's group [163] shows a high adsorption capacity of 417 mg/g and excellent selectivity in the presence of excess SO_4^{2-} (20,000 times). The trapped perrhenate (ReO_4^-) was anchored by three hydrogen bonds between the protons in imidazolyl groups and the oxygen in ReO_4^-, evidenced by the single crystal structure.

In order to increase the MOFs uptake capacity, Zhao's group [164] prepared a radiation-resistant MOF material under the assembly of $[Th_{48}Ni_6]$ nanocages. The adsorbent shows an outstanding capacity of 807 mg/g, which was attributed to the anion exchange and adsorption of $[Th_{48}Ni_6]$ nanocages. Xiong's group [165] developed a MOF composite material with ionic liquids (ILs) to improve the adsorption performance. *Via* the immersion grinding coupled with *in-situ* polymerization, a bisimidazolium-based IL was loaded inside and outside of the MOF matrix. The composite shows enhanced capacity of 673 mg/g compared with the

pristine poly(ionic liquid)s (215 mg/g).

The stability of MOFs is important for their practical applications. Wang's group [166] constructed a Ni-based 2D MOF material (SCU-103) for the extraction of TcO_4^- from an alkaline solution. Due to the concave-convex layered structure thwarting the attack of OH^-, the alkaline-stable MOF can remove more than 90% TcO_4^- in a pH 12 solution. In addition, SCU-103 shows an extraction percentage of ~90% at the solid-liquid ratio of 40 mg/mL from actual Savannah River Site high-level waste streams. For the sensitive detection of TcO_4^-, Xiao's group [167] rationally synthesized a fluorescent ZJU-X8 (ZJU = Zhejiang University) with the employment of tetraphenylethylene pyrimidine as the aggregation-induced emission (AIE) ligands. Different from the common anions, the addition of TcO_4^- or ReO_4^- could cause an obvious color change from brilliant blue to flavovirens, which indicates a macroscopic recognition for TcO_4^-.

3.7 Selenium

Ghosh's group [168] synthesized a cationic MOF for selenate removal. The MOF material can selectively capture selenate (SeO_4^{2-}) and exhibits an extraordinary adsorption capacity of 100 mg/g. Yang's group [155] prepared a Fe-based MIL-101 with numerous free coordination sites and large pore structures for SeO_3^{2-} adsorption. The high uptake capacity (183.7 mg/g) and outstanding selectivity are attributed to the formation of Fe-O-Se bond, as evidenced by the DFT calculations and EXAFS analysis (Figure 5h, i). In addition, Ghosh's group [169] rationally designed and synthesized a cationic MOF (iMOF-3C) as an effective scavenger for both SeO_3^{2-} and SeO_4^{2-}. The iMOF-3C displays a superior distribution coefficient value of larger than 10^6 mL/g for both selenium species, which is ascribed to the relatively high binding energies of these oxo-anions with the framework of iMOF-3C.

3.8 Iodine

Moissette's group [170] compared the iodine adsorption performance of UiO-66 with different Zr or Hf ratios (0, 51% and 100% Hf). The uptake capacities of these UiO-66s are ranked as follow: UiO-66(Hf) (285 g/mol) > UiO-66(51% Hf) (250 g/mol) > UiO-66(Zr) (230 g/mol). The higher acidity of Hf^{4+} could stabilize I_3^- in the $BDC^{\bullet+}$ (BDC = 1,4-benzenedicarboxylic acid) radical. Zhang's group [171] investigated a series of Zr-based MOFs constructed with $Zr_6(\mu3\text{-}O)_4(\mu3\text{-}OH)_4$ cluster and different organic ligands for iodine removal, including UiO-66, UiO-67, MOF-808, MOF-867, and NU-1000. Among these MOFs, MOF-808 displays the highest adsorption capacity of 2.18 g/g at 80°C, which is ascribed to the high binding affinity of the terminal hydroxyl groups with I_2 (−54 kJ/mol). Even though the electron-donating imidazole or pyridine groups have improved affinity to iodine, the incorporation of these groups in MOF-808/NU-1000 decreases the adsorption capacity due to their low stability and smaller pore volume.

In addition, various MOF-based composites have also been synthesized for iodine capture. Zhao *et al.* [172] prepared Cu-BTC@poly(ether sulfone) composite beads (BTC = 1,3,5-benzenetricarboxylate). When doping 71.9% Cu-BTC, the composite bead achieves a capture capacity of 639 mg/g. *Via* modifying nanoscale ZIF-8 to polyphenylene sulfide (PPS) nonwoven fabric, Xu's group [173] synthesized two functional membranes (PPS-ZIF-8 and PPS-ZIF-8-BSA), which showed the maximum adsorption of 2.51 and 2.07 g/g, respectively.

3.9 Rare gases (krypton, xenon, and radon)

The capture of radioactive rare gases such as ^{85}Kr, ^{133}Xe, and ^{222}Rn from complex atmospheric environments remains a formidable challenge due to their weak interactions with host materials and ultra-low concentrations. Tailored MOFs, achieved through fine regulation of pore size/shape and channel polarization, demonstrate high affinity for these rare gases with varying kinetic diameters and polarizability [174–184]. Data-driven computational modeling and screening have proven invaluable in discovering efficient adsorbents for rare gas separation. For instance, with the guidance of theoretical screening alongside thermodynamic and kinetic equilibrium principles, ZIF-7-Im with a quasi-open aperture exhibits superior Rn capture performance under normal temperature and pressure, surpassing commercialized activated carbon [185]. Additionally, benefiting from the suitable pore size and polar hydroxyl groups decorating in the channel surface, a stable squarate-based MOF selectively discriminates Xe over Kr (Figure 5j, k), showcasing an ultrahigh Xe Henry coefficient (192.1 mmol/(g bar)) and Xe/Kr Henry selectivity (54.1) (Figure 5l) [156].

In summary, MOFs have emerged as promising porous adsorbents for the removal of various radionuclides. Common strategies include decorating coordination groups and ion-exchange sites for efficient removal of ionic radionuclides. For rare gases, selective capture can be achieved by pore size match and enhanced channel polarity. The booming deep machine learning (ML) algorithms provide new avenues for developing effective MOFs tailored to specific requirements. To improve the practical applications of MOFs in real-world scenarios, their stability must be further elevated, particularly under severe acid and radiation conditions. Additionally, addressing the low availability of powdery MOFs necessitates easy and feasible approaches to shape modification while maintaining their exceptional adsorption performances.

4 COFs for radionuclides separation

4.1 Introduction of COFs

In 2005, Yaghi's group [186] applied topological design to synthesize porous organic polymers linked by reversible chemical bonds and reported the first group of COF materials (COF-1 and COF-5). On a fundamental level, COFs are 2D or 3D crystalline materials formed by the combination of a variety of organic building monomers, which are connected by covalent bonds and form a long-range ordered extended structure whose backbone is composed entirely of light elements (B, C, N, O, Si). The intrinsic structures and the tailorable organic monomers endow COFs with high surface area, tunable pore size, and facilely-tailored functionality, attracting increasing interest in multidisciplinary areas, including heterocatalysis, gas storage and separation, energy storage, pollutant removal and optoelectronic applications [187–189]. With the development of COFs, researchers are working on the design and preparation of COFs with a variety of different connecting bonds, including imine, hydrazone, triazine, vinylene, *etc*. (Figure 6a). The topological diagram makes it possible to design COFs with different skeletons and pore structures, which is the source of COF diversity (Figure 6b). In the topology diagram, COFs with different functions are designed by suitable monomer structure matching and realize efficient selective separation of different radionuclides, which greatly enriches the types of functional materials for radionuclides separation.

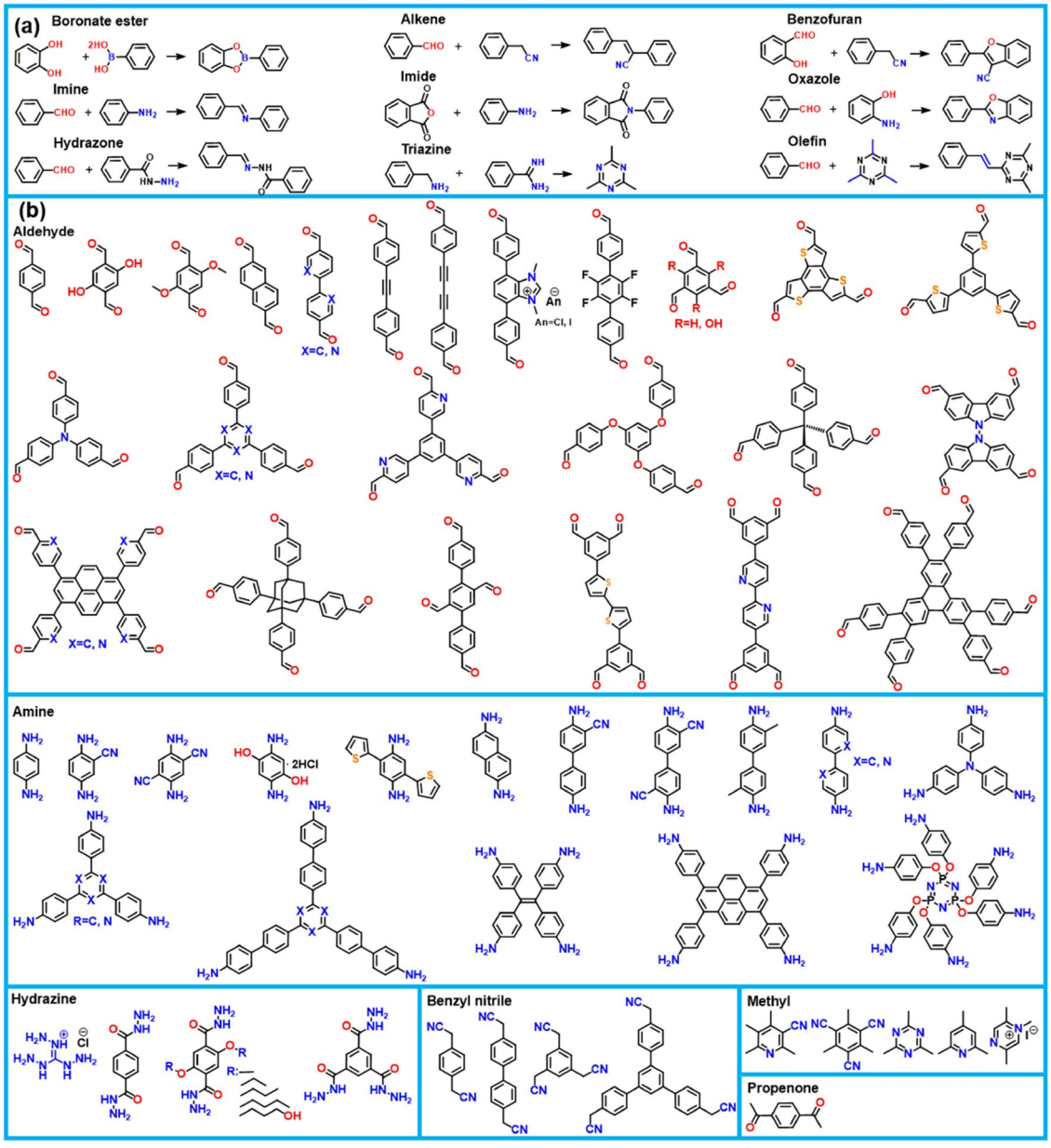

Figure 6 (a) Synthesis strategies of COFs with typical covalent linkages. (b) The diagram of the building blocks for radionuclides separation (color online).

4.2 Synthetic methods

COFs are regularly constructed *via* strong dynamic covalent bonds from simple organic ligands. Regulating the thermodynamic equilibrium in the formation of covalent bonds is the key to forming highly ordered covalent networks [188]. Polymerization conditions, including reaction time, pressure, temperature, solvent, pH, catalyst, oxygen-free and monomer concentration, should be considered in the formation of thermodynamically stable polymeric crystalline architectures [190].

4.2.1 Solvothermal synthesis

The solvothermal method is one of the most commonly used techniques for the synthesis of COFs, which needs to be completed in a closed system at a certain temperature [188]. The organic monomers, solvents, and catalysts are placed in Pyrex tube and degassed through several freezer pump-thawing cycles. The tube is then sealed and heated to an appropriate temperature for a certain reaction time (72 h for most of the time). The product is collected, washed with several suitable solvents, and dried under vacuum to obtain fluffy, powdered COFs. The reaction conditions of this kind of synthesis method are highly dependent on the reactivity, solubility and reversibility of the condensation reaction of the organic building monomer. In addition, reaction time, temperature, solvent type, catalyst type and monomer concentration are all important factors to be considered in the preparation of COFs by solvothermal method [191,192].

4.2.2 Interfacial synthesis

Interfacial polymerization is a widely used approach for the preparation of polymer thin films. Compared to COF powder obtained by traditional solvothermal methods, this method is mainly used to prepare COF nanosheets (CONs), which has the advantage of easy control of thickness. The nanosheets are able to grow gradually in an independent form without any support, and can be transferred to any matrix. Dey *et al*. [193] introduced the water-organic interface to prepare CONs for the first time. Two monomers were dissolved in different solvents (amine monomer dissolved in aqueous solution, and aldehyde monomer dissolved in CH_2Cl_2). The two solvents were insoluble to each other, and an obvious interface was formed at the junction of the two solvents. The COF growth is limited to the confined interface region, leading to the formation of thin films with good thermal stability, and high crystallinity. The interface method is beneficial in expanding the application of 2D COFs and also realizes the transformation of polymer materials such as COFs from powder to film.

4.2.3 Microwave synthesis

Microwave synthesis is a promising method of integral heating. Ritchie *et al*. [194] developed a high-performance method for the preparation of COF-5 and COF-102 in a microwave reactor, and the reaction speed of this method was 200 times higher than that of solvothermal. Microwaves can effectively improve the reaction rate and solve the problem of long reaction times in traditional solvothermal synthesis. In addition, it can remove residues and impurities from the framework more effectively, resulting in higher porosity. Therefore, microwave synthesis is expected to become the most effective method for industrial fabrication of COFs in the future.

The traditional synthesis processes of COFs are harsh and cumbersome (high temperature and pressure, long reaction time), and they are difficult to adapt to industrial production. High-energy ionizing radiation (electron beams and γ-rays) can be used to prepare and modify COFs. Compared with the traditional solvothermal method, electron beam irradiation ultrafast synthesis can reduce energy consumption, and the whole process can be completed in a few minutes. Zhang *et al*. [195] used a traditionally unperceived strategy to synthesize highly crystalline COFs by controlling electron beam irradiation of the received dose. This irradiation synthesis can be completed in minutes under ambient conditions, and the process can be used for large-scale production (Figure 7a).

4.2.4 Other synthesis methods

In addition to the above-mentioned methods for the preparation of COFs, rapid preparation methods such as the grinding method [196], ultrasonic method [197], photocatalysis method and ionothermal synthesis method [198,199] have been developed one after another. Large-scale and rapid preparation of high-quality COFs is a precondition for actual applications. Current synthesis methods of COFs are far from meeting the requirements of practical applications in terms of economic cost, time and yield [200]. Thus, strategies for scale-up and rapid preparation of COFs should be explored in further study.

4.3 Functional design of COFs

4.3.1 Bottom-up strategy

Bottom-up means that monomers are modified before COF preparation to obtain functional monomers, and then COFs are prepared by polymerization. Monomer modification is a general bottom-up synthesis strategy. Since the successful preparation of COF using alkyl functionalized monomers, this bottom-up method has been widely proved to be a simple and effective strategy for the synthesis of functionalized COFs [201,202].

So far, various COFs modified with monomer functional groups have been widely reported [203–207]. The significant advantage of this method is that functional groups could be

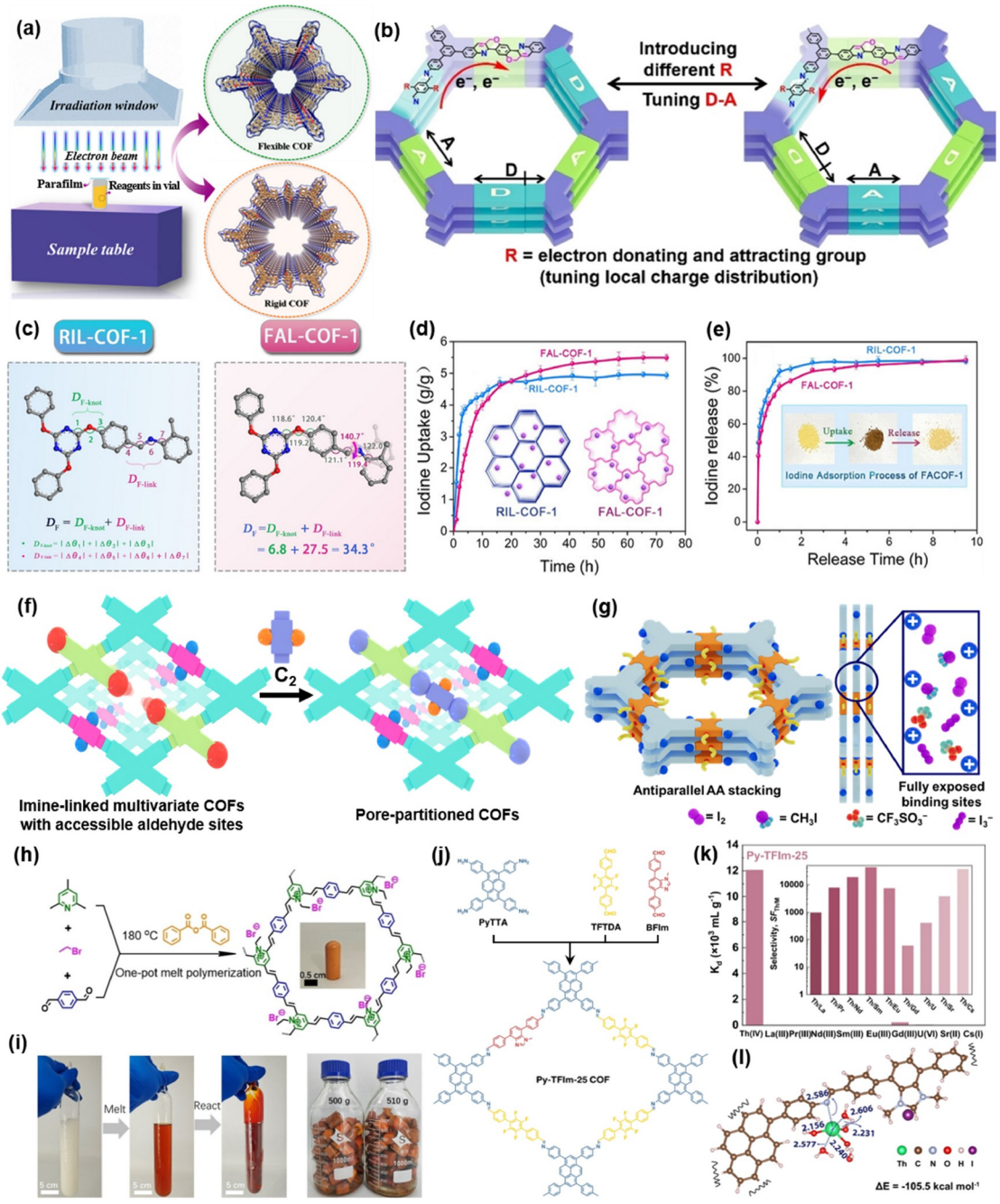

Figure 7 (a) COFs synthesized by electron beam irradiation [195]. (b) Construction of D-A systems by introducing functional building blocks in multivariate COF photocatalysts [225]. (c) The degree of flexibility, (d) iodine uptake and (e) controlled release of FAL-COF-1 and RIL-COF-1 [226]. (f) Pore partition strategy in imine-linked multivariate COFs [227]. (g) Antiparallel AA stacking COFs for constructing a multi-N nano trap [228]. (h) One-pot synthesis NKCOF-42-Br^- and (i) photos graph of synthesis NKCOF-41 on the kilogram scale [229]. (j) Synthesis of Py-TFIm-25 COF, (k) the distribution coefficients of Th(IV) and (l) DFT calculation on $[Th(OH)_3(H_2O)_3]^+$-Py-TFImI-25 COF [230] (color online).

evenly dispersed on the COF skeleton, and the number of active sites can be precisely controlled by adjusting the number of building monomers [208,209]. However, for some specific applications, it is difficult to synthesize functional monomers. Sometimes, specific functional monomers have been successfully prepared, but it is difficult to synthesize COFs with sufficient crystallinity. In addition, the active part of the functionalized monomer may need to be protected to avoid side reactions with other active sites in the structure. These problems hinder the formation of long-range ordered frameworks, and thus limit the application of bottom-up synthesis strategy.

4.3.2 *Top-down strategy*

The top-down strategy refers to the introduction of additional functional groups on the COF skeleton to improve its phy-

sical and chemical properties. In 2011, post-synthetic modification of COFs was first reported [210], and researchers introduced azides into the COF skeleton, after various alkynes can be reacted by clicking reactions, and large functional groups such as pyrene units can be further introduced into the framework. The amount of groups introduced after synthesis can be controlled by adjusting the proportion of azide fed in the first step [211]. In addition, changing the connecting bonds of COFs through oxidation and reduction is also a common post-functionalization strategy. Yaghi's group [212] reported the conversion of COF-connecting bonds from imines to amide bonds by direct oxidation. In addition to changing the connecting bond, cyclization reaction between the connecting bond and the adjacent group is also a commonly used method, leading to good crystallinity, improved stability and multiple functionalities [213–219].

Compared with the bottom-up strategy, the top-down strategy has several advantages, such as the fundamental COF can be simply prepared, the crystallinity can be guaranteed, and the suitable monomer combination can be selected according to the actual demand. However, active sites may not be fully exposed due to overlapping accumulation structures, resulting in incomplete functionalization.

4.4 COFs for radionuclides separation

4.4.1 COFs for uranium extraction

Nuclear energy is widely considered to be one of the cleanest energies. However, the development of nuclear energy has given rise to the excessive exploitation of U(VI) and the improper disposal of nuclear waste, resulting in a significant amount of U-containing waste [220]. Anchoring functional groups in adsorbent pores is an effective approach for preparing materials with specific adsorption properties [221]. Wu *et al*. [222] synthesized amidoxime-functionalized antibacterial COFs (AF Anti-COF). They attached the broad-spectrum antibiotic kanamycin to a stable sp^2 carbon coupling framework for gaining antibacterial properties. The AF Anti-COF, which was decorated with antibiotics, showed an excellent anti-biofouling property. The saturation adsorption capacities of AF Anti-COF were 406 mg/g in simulated seawater and 6.64 mg/g in natural seawater. Meanwhile, with fully π-conjugated frameworks, the material showed excellent luminescence properties. Thus, sensitive detecting of UO_2^{2+} could be achieved with the detection limit of 6.13 nM.

The competitive adsorption of V(V) and Cu(II) ions in seawater increases the difficulty of U(VI) extraction. Wang's group designed a series of COFs adsorbents with alternative chelating strategies, including hydrazine-carbonyl sites and assistant groups to enhance U(VI) adsorption. Among them, COF-R_5 containing hydroxypropoxy assistant groups showed fast U(VI) adsorption kinetics and as high uptake capacity of 11.3 mg/g with a distribution coefficient exceeding 9.2×10^5 mL/g in seawater [223]. Based on reticular chemistry, Chen *et al*. [224] constructed a class of isoreticular hydrazine-based COF photocatalysts. The photoelectric properties and local pore characteristics of COFs were adjusted by different hydroxyl linkers. Batch experiments and theoretical calculations explored the excited state electron distribution and transport pathways at the molecular level. COF-4 has significant excited state electron utilization efficiency and charge transfer performance, and achieves photocatalytic U(VI) extraction performance of ~6.84 mg/(g·d) in natural seawater. This study brings a new way to operate COF-based photocatalysts, guiding the development of new COFs for U(VI) extraction from seawater.

Benefit from the π-π stacking between the obviously ordered columnar array and 2D sheets, there is great promise for COFs to exhibit exceptional potential in the field of photocatalysis [231–234]. Recently, Li *et al*. [235] synthesized an amino-functionalized benzodiimidazole COF (BBCOF) *via* one-step cyclization and aromatization. The introduction of benzodiimidazole rings significantly enhanced the stability of BBCOF, leading to unchanged crystallization in both extreme acid and base solutions. At the same time, the enhanced conjugation degree and free amino groups endowed BBCOF with an efficient photocatalytic reduction to remove U(VI). The removal rate of U(VI) by BBCOF reached up to 96.6% in the single-ion system without sacrificial agents. In addition, the BBCOF exhibited a high selectivity of 85.3% towards U(VI) in a multi-ion system containing 11 coexistent ions (Co, Ni, Sr, Nd, Sm, Gd, *etc*.) with K_d as high as 4.9×10^2 L/g. Yang *et al*. [225] created novel intramolecular donor-acceptor systems by turning the charge separation of the framework. Among their synthesized COFs, COF 4P demonstrated an extremely high U(VI) uptake capacity of 8.02 mg/(g·d) in natural seawater (Figure 7b). COFs also show great potential in adsorption-electroextraction of U(VI) from seawater. Zhang *et al*. [236] designed a novel stable sp^2 carbon-linked 3D COF (TFPM-PDAN-AO). The regular 3D pore channel of 7.12 Å provides a specific channel for uranyl diffusion, amidoxime group exhibits high selectivity and fast kinetics for U(VI) adsorption, applying alternating voltages between −5~0 V for U(VI) electroextraction. Uranyl migrates to the electrode of TFPM-PDAN-AO, then inducing the electrodeposition of U(VI) compounds to form the charge neutral species ($Na_2O(UO_3H_2O)_x$) with an unprecedentedly high adsorption capacity of 4,685 mg/g.

Membrane-based processes have the potential to push rare earth separation towards sustainable and environmentally friendly development owing to the associated energy-efficiency, eco-friendliness, ease of operation and excellent separation efficiency [237]. In the past decade, COF-based membranes, with the advantages of pore-ordered structure, porosity, and functionality, have attracted continuous atten-

tion [187,238,239]. Xiong *et al*. [240] prepared a sulfonated-based COFs $[NH_4]^+[COF\text{-}SO_3^-]$. The mixed matrix membrane was fabricated by mixing polysulfone with $[NH_4]^+[COF\text{-}SO_3^-]$, and for the first time, the membrane-based separation experiments of Th(IV) from U(VI) and rare earth elements. In a multi-ion system containing Th, U, Eu, Ce (Th and other metal ions with a concentration ratio of 5 ppm/25 ppm), the removal rate of this COF-based membrane for Th(IV) was 72.4%, with much lower removal rates for U (28.5%), Ce (16.5%) and Eu (19.2%). The selectivity was calculated as $S_{Th/U}$ = 6.9, indicating that COF-based membranes had tremendous potential in the separation of nuclides. To design multifunctional COF composites for U(VI) separation, Liu *et al*. [241] prepared bifunctional photocatalyst MOF525@BDMTp by *in-situ* covalent bridging method. MOF525@BDMTp achieved the simultaneous reduction of U(VI) on BDMTp and the oxidation of CP on MOF525, owning to the BDMTp interacted with S and N atoms in CP to promote its hydrolysis and oxidation by h^+ and $\cdot O_2^-$, MOF525@BDMTp had a U(VI) removal capacity of 625.0 mg/g and CP removal rate of 99.8%. Furthermore, Bi *et al*. [242] used a Ti-MOF as the core and *in-situ* growing COF DATp shells on its surface, which was used for simultaneous photocatalytic reduction of U(VI) and oxidation tetracycline. The staggered energy levels between Ti-MOF and DATp create a Z-Scheme heterojunction through covalent bonds and promote the charge and hole transfer. Ti-MOF@DATp can effectively accomplish the simultaneous photocatalytic removal of 96% U(VI) and 90% tetracycline of their mixture. These bifunctional MOF/COF photocatalysts offer an effective approach to tackling complex radionuclides separation.

4.4.2 COFs for iodine capture

In 2017, Yin *et al*. [243] synthesized a hollow spherical hetero-pore COF (SIOC-COF-7) connected by imine bonds. As the first case for COF-based iodine adsorbent, SIOC-COF-7 exhibited highly volatile iodine capture capacity. Under the combined action of rich aromatic rings and high N-content, pore-orderly framework and inner cavities of the hollow shell structure, an iodine uptake capacity of 481 wt% was achieved. It is confirmed from plenty of studies on the adsorption of iodine by COFs that there are strong charge transfer interactions between electron-rich functional groups and iodine. Specific electron-rich functional groups such as free amine groups, alkynes and acetylene-imine bonds can effectively enhance the adsorption capacity of materials for volatile iodine [244–246]. Shreeraj *et al*. [247] explored two N-rich COFs, TTPA-COF and TAPT-COF, with vapor phase iodine saturation adsorption capacities of 4.43 ± 0.01 g/g and 3.70 ± 0.017 g/g, respectively. The iodine adsorption of TTPA-COF was better than that of TAPT-COF, which can be attributed to the presence of pyridine functional groups. As an additional adsorption site for iodine, it has been reported that electrons transfer from N in the pyridine part to iodine, resulting in a strong interaction between the pyridine group and iodine [248,249], which was consistent with the higher nitrogen content in TTPA-COF in elemental analysis. Zhai *et al*. [250] developed two cationic COFs (C-TP-PDA-COF and C-TP-BPDA-COF) through post-synthetic modification. The iodine capture capacity of modified COF was 1.3 times higher than that of unmodified neutral COF. Mechanism studies showed that I_2 and I_3^- signals appeared simultaneously in X-ray photoelectron spectroscopy (XPS) of cationic COF, while only I_2 signals appeared in the corresponding neutral COF, indicating that cationic COF was the result of the synergistic effect of physical and chemical adsorption, by contrast, it was typical physical adsorption for the neutral COF. The problem of non-destructive processing of powders, such as COFs, into macroscopic materials with a wealth of structural and functional is still a challenge [251]. Li *et al*. [252] improved the preparation method, with Sc $(OTf)_3$ introduced as the catalyst, and pure COF aerogels with layered interconnected pore networks were prepared. The iodine uptake capacity of COFA-1 was 8.15 g/g in the static experiment and 4.53 g/g in the dynamic condition, both were over 30% higher than that of powder COFP-1. The authors also carried out iodine adsorption experiments in saturated I_2 aqueous solution, KI/I_2 aqueous solution and *n*-hexane, the adsorption capacities of COFA-1 were 6.78, 7.13 and 6.90 g/g, respectively. In addition, a homemade purifier was designed to evaluate the iodine adsorption capacity of COFA-1 under simulated industrial conditions. As a result, a recorded iodine uptake of 269 mg/g was achieved, confirming the promising potential of COFA-1 in practical applications.

Zhang *et al*. [226] first reported a series of flexible amine-linked COFs with high crystallinity synthesized by formic acid as a catalyst. In the process of imine bond formation, the reaction mechanism is asynchronous *in-situ* reduction. The flexibility of COFs makes them adaptable to guest molecules and improves the iodine adsorption capacity. By comparing the structural characteristics, it is found that the flexibility of FAL-COF-1 comes from the rotation of the chemical bond of the knot unit and the linker unit (Figure 7c). Since both FAL-COF-1 and RIL-COF-1 are rich in N elements and have ordered and abundant active sites in the pore structures, the two materials exhibit a high ability for iodine capture. Compared with RIL-COF-1, the adsorption rate of FAL-COF-1 is slower, but its iodine adsorption capacity is significantly improved (Figure 7d). The stronger host-guest interaction also makes the desorption rate of FAL-COF-1 slower than that of RIL-COF-1 (Figure 7e). This may be because the flexible framework of FAL-COF-1 has certain elasticity and adaptability, self-regulation and adaptive structural adjustment for the entry of guest molecules, thus

enhancing the adsorption capacity.

The pore structure and specific binding sites of COFs are crucial for iodine capture. Hao *et al*. [227] reported a specific strategy for partitioning the micropores/mesopores of multi-component COFs by pre-designing and synthesizing multi-component COFs, immobilizing aldehyde groups in COF pores through an imine condensation reaction and then inserting additional symmetrical building blocks (with C2 or C3 symmetry) as pore partition agents (Figure 7f). This method allows tetragonal or hexagonal pores to be partitioned into two or three smaller micropores, respectively. Based on the pore size matching and complexation of I_2 and CH_3I molecules with COFs, the pore size and the introduction of functional groups were precisely regulated, achieving directional I_2 and CH_3I capture. Furthermore, Wang's group [228] synthesized antiparallel stacked COFs with pyridine-N and hydrazine groups, and converted pyridine-N sites to cationic pyridinium moieties, yielding a cationic framework, showing high adsorption capacity for I_2 and CH_3I and efficiently capture I_3^- from contaminated water, and quickly purify iodine-contaminated groundwater to reach drinking water levels (Figure 7g).

4.4.3 COFs for other nuclides separation

As a man-made radionuclide, ^{177}Lu is extremely difficult to isolate from ^{176}Yb because of physicochemical properties of Yb^{3+} and Lu^{3+} and huge content gap between ^{176}Yb and ^{177}Lu ($\geqslant 10^5$:1) [253]. Peng *et al*. [254] introduced alkyl chain with different length in 2D COF holes. As a guest molecule, 2-ethylhexylphosphonic acid mono-2-ethylhexyl ester (P507) was introduced into the channels by the host-guest self-assembly. Dynamic column experiments showed that efficient separation of Yb/Lu can be achieved by employing 1.0 M HNO_3 as eluent, in which ERCOF-1@P507 has the highest decontamination factor (DF) of 18.10, and the recovery rate of Lu^{3+} is 98.05%.

Yang *et al*. [255] developed an electro-adsorption strategy in which carboxy-functionalized COF-1 and cationic COF-2 were loaded onto the cathode and anode surfaces, respectively. With the existence of electric field, the simultaneous adsorption of cations and anions was realized through the design of asymmetric electrode, and the maximum uptake capacities were 411 and 984 mg/g for U(VI) and Re(VII), respectively, which were both more than twice higher than the physical chemical adsorption. Hao *et al*. [256] developed a cationic pyridinium salt-based COF (PS-COF-1) with a high surface area of 2,703 m^2/g. Well-defined nanochannels, chemical stability, and radiation resistance endowed PS-COF-1 with exceptional adsorption performance toward ReO_4^- (1,262 mg/g) and $^{99}TcO_4^-$ from aqueous solution. According to the consequence of DFT calculations, there was a strong affinity between ReO_4^-/$^{99}TcO_4^-$ and framework, which facilitated the adsorption of low charge density anions rather than other anions (*e.g*., Cl^-, NO_3^-, SO_4^{2-}, CO_3^{2-}). Large-scale and low-cost prepared COFs for industrial radionuclides separation remains formidably challenge. Zhang *et al*. [229] prepared a series of highly crystalline olefin chain COFs by melt polymerization using 2,4,6-collidine as monomer (Figure 7h). This method enables the manufacture of kilogram-level self-shaped monolithic robust foams. The cost of COFs is extremely low (50 USD/kg). In addition, neutral COFs were easily converted into ionic COFs by one-pot or post-modification method, which can be used as efficient ion exchange adsorbents for ReO_4^- adsorption (Figure 7i).

Recently, Zu *et al*. [257] synthesized a COF with β-ketoenamine structure (Tp-DTA), which had a saturation adsorption capacity of 145.4 mg/g for Sr^{2+}. The Tp-DTA COF exhibited high selectivity towards Sr^{2+} in multi-ion system containing (Na^+, K^+, Cs^+, Mg^{2+}, *etc*.) with the removal efficiency of Sr^{2+} as high as 97%. Liu *et al*. [230] synthesized an ionic COF (PyTFImI-25 COF) and its deionization analog COF (Py-TFIm-25 COF), to investigate the influence of N sites on the adsorption capacity and selectivity of Th(IV) (Figure 7j). The introduction of TFTDA enhanced the molecular interlayer interaction between fluorinated building blocks and other building blocks, thereby improving the crystallinity and chemical stability of COFs. The selectivity of Py-TFIm-25 COF for Th(IV), in the presence of competing ions including U(VI), Sm(III), Nd(III), La(III), Gd (III), Eu(III), Sr(II), and Cs(I), exhibited a distribution coefficient of 1.21×10^4 mL/g for Th(IV), the separation factors $SF_{Th(IV)/M}$ were 10^2–10^5 for Th(IV) compared to other competing ions (Figure 7k). The DFT calculation revealed that $Th(OH)_3(H_2O)^+$ episode interacted with the $N_{-C=N-}$ in Py-TFIml-25 COF, with the calculated Th-N bond distance of 2.586 Å and binding energy of –105.5 kcal/mol, which is comparable to the case of Th(IV) interaction with Py-TFImI-25 COF. The absolute binding energies of Py-TFIm-25 COF are greater than the corresponding energies of Py-TFImI-25 COF (Figure 7l). This work provides insight into the relationship between the structures and properties of thorium COF adsorbents. For the recovery of Pd(II) from waste streams, Xie *et al*. [258] used a "single-ion trap" strategy to synthesize an antiparallel stacked COF (ACOF-1) with hydrazine-carbonyl sites and pyridine sites for efficiently recovering Pd(II) from super acidic wastes. The constructed Lewis base site single ion trap had high affinity for Pd(II) and achieved Pd(II) capture in a wide pH range. The developed ACOF-1 adsorbent demonstrated fast kinetics, excellent selectivity, and a high uptake capacity of 412.9 ± 14.2 mg/g for Pd(II) in 3 M HNO_3 solution. The results provide ideas and methods for material design and functionalization for the directional separation of target nuclides in nuclear power decontamination wastes.

Jia *et al*. [259] adjusted the pore size of COFs to match the

diameter of Xe *via* multi-site alkylation strategy. Two original COFs and their corresponding functionalized products were successfully prepared, named TFB-TAPA and TFP-TAPA, TFB-TAPA-Bu and TFP-TAPA-Bu, respectively. TFP-TAPA-Bu, as a typical case, exhibited the highest adsorption and separation performance for Xe/Kr, the maximum adsorption capacity for Xe was up to 85.6 cm^3/g, and the Xe/Kr selectivity can reach to 9.7. In addition, the synthesized products had good irradiation stability, indicating that TFP-TAPA-Bu was a promising adsorbent for Xe/Kr adsorption and separation.

4.5 Mechanism of COFs for radionuclides separation

The introduction of functional groups, which can coordinate with certain elements, into the structure of COFs can improve the adsorption performance, for instance, phosphate ester groups [260], carboxyl groups [261,262] and amidoxime groups [263,264]. Charge-transfer interaction is the most widely reported mechanism of iodine adsorption. Electron-deficient iodine molecules are partially or completely converted to iodine ions after adsorption with the presence of electron rich donors, such as free amine groups, alkynes and imine bonds, thus the strong electrostatic interaction between the adsorbent and iodine ions allows the iodine to be effectively capture [265,266]. In addition to coordinate with functional groups, electrostatic attraction/repulsion of ions is also a separation mechanism, the charged side chain of ion COFs allows them to capture the target ions by electrostatic force. The semiconductor properties of COFs endow them excellent photocatalytic performance [231], and there have been many studies on UO_2^{2+} enrichment and separation. Finally, the pore size of COFs can be adjusted through the selection of building blocks and the modification of pore walls, which is also the reason why COFs have outstanding advantages in adsorption and separation applications.

4.6 Prospect of COFs for radionuclides separation

The research on the application of COFs in the separation of radionuclides has only begun in recent years. COFs are booming in the field of radionuclide removal. The practical separation applications with advantages are difficult to achieve with traditional methods. Up to now, the reported COFs and the types of radionuclides involved are not systematic and comprehensive enough. Besides, the basic research and mechanism exploration of COFs are still limited to the laboratory stage, and there is still a long way to go before they can be used in the separation of radionuclides in a real environment. With regard to future studies, we believe that:

(1) In terms of structure and performance, the flexible and adjustable structural units, connection modes and pore size of COFs can be used to design and find new COFs with functional components suitable for the separation of specific radionuclides. On the other hand, COFs can also be used as functional platforms, and corresponding functional groups can be used for post-modification according to different separation objects. In addition, in order to apply such materials in extreme environments such as high acidity, high temperature, and strong radiation in the nuclear fuel cycle process, the physical and chemical stability of the materials must be considered while taking into account the selectivity and adsorption capacity of the target radionuclides.

(2) In terms of practical application, COFs in powder form are difficult to handle and recycle, which may cause potential pollution and further result in obstacles to the practical application of COFs in the separation of nuclides. On the premise of maintaining excellent adsorption capacity, shaping COFs into films, foams, or aerogels may overcome this obstacle to some extent. In addition, column separation is also an effective means of using COF powder as a stationary phase in the chromatographic column. Different distribution coefficients of radionuclides between the stationary phase and the mobile phase can achieve effective separation of various radionuclides.

(3) In terms of economy, in order to promote the wide application of COFs in the separation of radionuclides in practical applications, great efforts need to be paid to exploit strategies for large-scale and rapid preparations of COFs in simple, mild and cheap paths.

5 Porous organic polymers for radionuclides separation

POPs are usually constructed by repeating one or several structural units by connecting each other through strong covalent bonds to form large relative molecular masses. Recently, polymers have been widely used in separation of radionuclides due to the following aspects. (1) POPs usually have high thermal stability and excellent acid-base resistance properties. (2) POPs exhibit high adsorption capacity and selectivity for radionuclides. (3) The economic cost of preparation offers the possibility of large-scale production. (4) Functionalized POPs offer enhanced application potential. To meet the demands for removing different radionuclides, various polymers were constructed, such as hyper-cross-linked polymers (HCPs), porous aromatic frameworks (PAFs), porous polymer networks (PPNs), polymers of intrinsic microporosity (PIMs), and conjugated microporous polymers (CMPs).

5.1 POPs for uranium extraction

Uranium is an important fuel for the production of nuclear

energy [267–271]. Among the strategies for U(VI) treatment, adsorption was proved to be an effective approach to separate radionuclides. The most important factor affecting adsorption is the adsorbent. Recently, various solid adsorbents have been development for U(VI) extraction from wastewater and seawater. Usually, the essence of U(VI) extraction by adsorption, photocatalytic, or electrocatalytic method relies on the active sites between ligand and uranyl ions. Many groups, such as hydroxyl, carboxyl, amidoxime, phosphate, and imidazole are conductive for interacting with uranyl ions, enhancing U(VI) extraction (Figure 8) [272–277].

Li *et al*. [278] prepared a highly phosphorylcholine (PC)-functionalized fibrous (PAN-PC) as U(VI) adsorbent. Benefiting from the strong coordination and electrostatic interactions, PAN-PC exhibited a remarkable adsorption capacity of 2,658 mg/g for uranyl ions. Yue *et al*. [279] synthesized novel phosphate-based hypercrosslinked polymers (HCPs). U(VI) can be extracted by HCPs with the maximum sorption capacity of 302 mg/g at pH = 7. Amidoxime functional group was considered another efficient group for U(VI) extraction. Normally, this group is derived from the reaction of cyano-containing substances with hydroxylamine. Ahmad *et al*. [280] produced amidoxime-modified polymer (POP-AOF), exhibiting the maximum U(VI) adsorption capacity of 725 ± 3 μg/g. Tian *et al*. [281] reported amidoxime-functionalized HCP-AO, the maximum U(VI) sorption capacity was 234.46 mg/g in pH = 7 solution owing to the strong coordination between amidoxime groups and U(VI). Zhang *et al*. [282] developed an imidazole-functionalized polymer (PDVB-VIM) and the U(VI) adsorption capacity reached 689.9 mg/g, attributing to the high content of accessible imidazole ligands. Xu *et al*. [283] constructed three perylene-containing conjugated microporous polymers (PeMe, PeEt and PePy) and post-modified by sulfonation reaction. The results showed that the PePy-SO_3H exhibited U(VI) adsorption capacity of 579.0 mg/g owing to the strong affinity toward U(VI). Li *et al*. [284] constructed a novel malonamide-carboxyl bifunctional crosslinked polymer (MCFCP), affording the largest adsorption capacity of 239.6 mg/g for U(VI) at pH = 4.0. Exploring excellent functional materials for U(VI) extraction and detection is highly desired. Leng *et al*. [285] synthesized a series of amidoxime-functionalizing covalent organic polymers (COPs) for U(VI) extraction and detection (Figure 9a). The tPF-AO showed a theoretical maximum adsorption capacity of 578.9 ± 15.2 mg/g with compact steric structure, and U(VI) selective binding sites endow tBPF-AO with selective detection ability for U(VI). The detection limit is 24.2 nmol/L, which is much lower than the WHO standard of U(VI) in drinking water.

Photocatalytic U(VI) reduction from seawater and nuclear waste is considered one of the novel, efficient and non-pollutant technologies. Under sunlight irradiation, the photocatalyst obtains a certain amount of energy, and the electrons (e^-) at the internal valence band position directionally transfer to the conduction band, leaving an equal number of holes (h^+) in the corresponding valence band. The electrons and holes transfer to the surface of the catalyst, and the adsorbed U(VI) on the catalyst surface will be reduced to U(IV) by electrons. The generated holes can further synergistically oxidize organic matter in water [94,224,286,287].

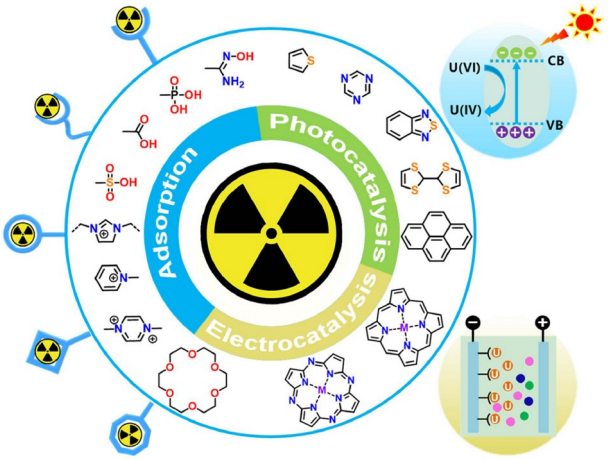

Figure 8 Polymer functionalization strategies for radionuclides processing (color online).

At present, research on photocatalytic U(VI) removal mainly focuses on the development of new photocatalysts. Constructing the highly polymerized donor-acceptor and donor-acceptor-acceptor (D-A-A) motifs in polymers to improve exciton dissociation and promote the separation of electron-hole pairs has been popularly deemed as one of the effective measures. Liang *et al*. [288] used perylene as the donor and two different acceptors (9H-fluoren-9-one and dibenzo[b,d]thiophene 5,5-dioxide) to prepare two different polymers (ECUT-CO and ECUT-SO). The results showed that ECUT-SO performed high reduction efficiency up to 97.8% within 60 min compared with ECUT-CO (72.2%). The high reduction efficiency for ECUT-SO was mainly due to the strong acceptor enhanced visible-light absorption and improved interface electron-hole separation and transfer. Yu *et al*. [289] used two acceptors, dibenzothiophene-*S*,*S*-dioxide (SO) and benzothiadiazole (TH), to design a series of D-A-A polymers, achieving a photocatalytic U(VI) reduction of 99.2% within 120 min in 50 ppm solution. Moreover, they also developed conjugated microporous polymers (CMPs) with D-A_1-A_2 terpolymers for exciton U(VI) photoreduction (Figure 9b). CMPs have large dipole moments and a built-in electric field, which can inhibit charge recombination and promote charge separation. Therefore, PTrSO-2 with feed molar ratio 0.75/1.0/0.75 achieved 99.5% photocatalytic U(VI) reduction efficiency within 120 min [290]. Since most of the photocatalysts show comparatively

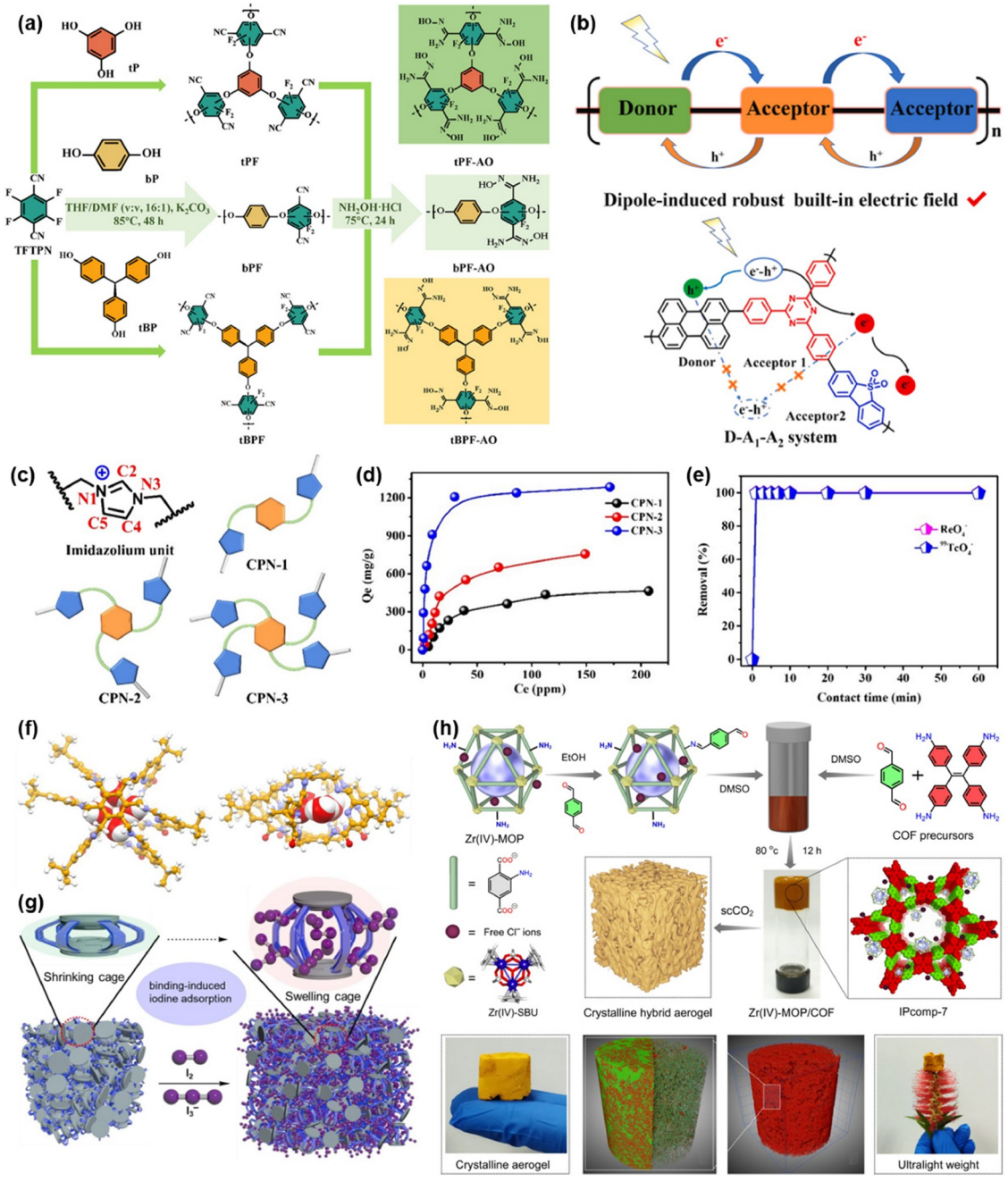

Figure 9 (a) Synthetic strategy of COPs [285]. (b) D-A_1-A_2 system in the photoinduced electron-transfer process [290]. (c) Imidazolium unit and the repeating units in CPNs; (d) sorption isotherm and (e) kinetics of the CPNs for $^{99}TcO_4^-$/ReO_4^- uptake [56]. (f, g) Mechanisms of the iodine adsorption with NAS materials [304]. (h) Fabrication procedure and various characteristics of the composite [305] (color online).

poor stability in highly acidic environments, Wang *et al.* [291] synthesized a new polymer (CTATP-DHBA) to realize the reduction of U(VI) in pH = 1 solution. The results exhibited the removal efficiency of 83.27% in 200 ppm solution. Chen *et al.* [287] designed a new D-A polymer (pTTT-Ben) to realize the photocatalytic reduction of U(VI) in a strongly acidic solution.

5.2 POPs for TcO_4^- extraction

Technetium ($^{99}TcO_4^-$), belongs to β radionuclide substance and is mainly derived from nuclear fission processes of ^{235}U and ^{239}Pu in nuclear weapons and power plants [292–294]. When Tc element is exposed to the environment, it mainly exists stably in the form of high $^{99}TcO_4^-$ with weak oxidizing power. Due to its extremely high solubility (11.3 mol/L) and good fluidity, $^{99}TcO_4^-$ can easily migrate through soil and groundwater [292,295,296]. Therefore, the removal of

$^{99}TcO_4^-$ is considered a significant task. However, this task is difficult and challenging because $^{99}TcO_4^-$ is usually located in high salinity aqueous solutions and a large number of coexisting anions such as NO_3^-, SO_4^{2-}, and CO_3^{2-} interfered with its removal. In addition, the waste liquid containing $^{99}TcO_4^-$ also has extremely high ion strength and strong ionizing radiation, which raised the requirements for the stability and selectivity of separation materials. Therefore, the synthesis of high-stability materials for removing $^{99}TcO_4^-$ has become a hot topic. Since $^{99}TcO_4^-$ is radioactive, it is risky to use in common laboratories. Rhenium (Re) element is in the same group as Tc and it has a similar atomic radius, ionic radius and extranuclear electron distribution similar to Tc. In addition, ReO_4^- also has a similar physical structure and chemical properties to $^{99}TcO_4^-$. Therefore, ReO_4^- is often used as a substitute for $^{99}TcO_4^-$ in experiments to avoid radioactivity and toxicity [297,298]. At present, several technologies, such as ion exchange, oxidation-reduction, extraction, and precipitation, are developed to remove $^{99}TcO_4^-$ in large-scale processes [15,299,300]. Among these, ion exchange is considered an effective method for removing $^{99}TcO_4^-$ from large amounts of nuclear waste due to its simple operation and high-efficiency recovery rate. In this section, we will focus on the removal of $^{99}TcO_4^-$ using the ion exchange method.

Cationic organic polymers, especially those containing imidazole, pyridine and methyl groups, are helpful for $^{99}TcO_4^-$ removal according to the ion exchange. Zhou *et al.* [301] synthesized an imidazolyl-based polymer TIB-TBPB, exhibited a high capacity of 882 mg/g and rapidly removed ReO_4^- from solution within 20 min, 80% of ReO_4^- was removed in a short time of ~5 min. In addition, the selectivity, recyclability and working ability of TIB-TBPB in 3 M HNO_3 and the Hanford LAW simulated nuclear waste were also excellent. Yang *et al.* [57] constructed a serious of ionic COPs with cationic imidazolium sites (iCOP-1, 2, 3). The parent iCOP-1 showed fast kinetics and high adsorption capacities (up to 1,434.1 ± 24.6 mg/g). In addition, iCOP-2, which is prepared by introducing F groups, exhibited high ReO_4^- removal efficiency up to 58% within 60 min in 3M HNO_3 solution. Further, Br groups were also introduced to prepare iCOP-3. It was found that iCOP-3 could remove ReO_4^- from the alkaline nuclear waste stream. This work hints that the halogenation strategy could remove $^{99}TcO_4^-$ in a wide pH range. Sun *et al.* [302] prepared a series of pyridine-functionalized POPs. Among them, PQA-pN(Me)2Py-Cl possessed a sorption capacity of 1,127 mg/g and 95.3% removal was achieved after 5 min for ReO_4^-. Li *et al.* [294] synthesized a cationic polymeric network (SCU-CPN-1-Br) and then immersed it into a saturated NaCl solution to replace toxic Br^- with Cl^- (SCN-CPN-1). The results showed that SCU-CPN-1 had a high removal rate (99% of $^{99}TcO_4^-$ from aqueous solution in less than 30 s) and high selectivity from highly acidic solutions even in the existence of competing anions. Yi *et al.* [303] reported a methyl-rich cationic polymer network (TBT-TCB), exhibiting the high removal efficiency of $^{99}TcO_4^-/ReO_4^-$ (85%) in 1 M NaOH and 84% in 1 M H_2SO_4 because the introduction of methyl groups could enhance its hydrophobicity. Wang *et al.* [56] designed CPN-3 (CPN denotes cationic polymeric nanotrap) for selectively removing $^{99}TcO_4^-$ from concentrated alkaline nuclear wastes (Figure 9c). It is worth noting that the adsorption capacity of CPN-3 for ReO_4^- in simulated Hanford and Savannah River Site waste streams reached a record value of 1,052 mg/g (Figure 9d), CPN-3 also had excellent stability in harsh alkaline and radioactive environments as well as had fast kinetics, achieved rapidly sorption equilibrium within 1 min, with a removal rate exceeding 99.9% (Figure 9e).

In addition, guanidine and viologen-based cationic polymers were also applied to $^{99}TcO_4^-$ removal. Da *et al.* [306] reported that a guanidine-based cationic covalent organic nanosheets (iCON) had a high uptake of 437 mg/g towards $^{99}TcO_4^-$ with the prominent distribution coefficient of 5.0×10^5. $DhaTG_{Cl}$ showed ultrafast adsorption kinetics for ReO_4^- (initial concentration of 25 mg/L) with rapid removal of 98.0% within 5 min. Zhao *et al.* [307] also constructed guanidine-based cationic covalent polymers (TG-TPAL-H), which exhibited the sorption capacity to 549 mg/g for ReO_4^-. Ding *et al.* [308] prepared a viologen-based cationic organic polymer (VBCOP). VBCOP obtained the removal efficiency over 99% after 30 s in $^{99}TcO_4^-$ confirmatory experiment, about 99.9% of $^{99}TcO_4^-$ was removed after 5 min. Besides, the K_d of $^{99}TcO_4^-$ was calculated as high as 7.2×10^5 mL/g. To improve the stability and adsorption capacity of viologen-based polymer, Huang *et al.* [309] used 4,4′-bipyridine and tetraphenylmethane to design the diamond-like topology structure of TZ-PAF, showing fast sorption kinetics and high sorption capacity (982 mg/g for ReO_4^-) due to the high density of sorption sites.

3D polymers are also synthesized to remove $^{99}TcO_4^-/ReO_4^-$. Yuan *et al.* [310] reported a 3D fluorinated pyridinium-based COP (TBPM-Fpz), which possessed ultrafast sorption kinetics for ReO_4^- (equilibrium within 3 min). The uptake capacity reached to 833.01 mg/g towards ReO_4^-. Qi *et al.* [311] constructed a 3D ionic olefin-linked polymer (TFPM-EP-Br). It can not only act as a fluorescent sensor for $^{99}TcO_4^-$ according to the electron transfer from TFPM-EP-Br to $^{99}TcO_4^-$, but also remove $^{99}TcO_4^-$ with adsorption capacity of 345.68 ± 10.37 mg/g.

5.3 POPs for iodine capture

Radioactive iodine (^{129}I, ^{131}I) has become one of the pollutants that should be given special attention in the nuclear fuel cycle [246,312–315]. Radioactive iodine mainly exists in the form of organic iodine and inorganic iodine when escaping

into nature. Organic iodine is represented by CH_3I, while inorganic iodine is represented by I_2, I^-, and IO_3^-, all of which have active chemical properties. Therefore, filtration and purification treatment must be carried out before its discharge [126,316]. Polymers are usually connected by irreversible covalent bonds. Therefore, they can be applied in extreme environments such as strong acid and alkali conditions. In recent years, using polymers to adsorb radioactive iodine has attracted widespread attention. The iodine adsorption by polymers is influenced by their pore structures. For example, polymers with a highly specific surface area and appropriate pore size are helpful for iodine adsorption. On the other hand, the affinity sites of iodine, including π-conjugated structures such as aromatic rings, double bonds, triple bonds and heteroatom groups containing electrons (N, O, and S) are also considered important factors for iodine adsorption due to the improving host-guest interaction between the network of polymers and iodine [317–319].

Pourebrahimi *et al*. [320] synthesized two conjugated covalent triazine frameworks (CTF-DPA and CTF-TS) through a facile Friedel-Crafts alkylation reaction. The iodine vapor capture capacity reached to 5.12 g/g for CTF-DPA, higher than CTF-TS (3.75 g/g). In addition, the authors found that C≡C was more effective in adsorbing and stabilizing the (poly)iodide species than C=C. Therefore, CTF-DPA exhibited a more efficient platform for capturing iodine. Wang *et al*. [321] constructed two hyper-crosslinked polymers (PIHCP-1 and PIHCP-2) *via* the Friedel-Crafts alkylation reaction of the polyimides. The iodine uptake capacity for PIHCPs reaches 6.73 g/g due to the great contribution of hydroxyl groups and multiple electron donor sites in polyimide skeleton. Wang *et al*. [322] obtained a novel electron-rich hyper-crosslinked polymer (HCP) *via* a simple photocycloaddition of the cinnamoyl-containing polyimide precursor. The material exhibited high iodine vapor capture up to 5.28 g/g.

As we mentioned above, introducing heteroatom groups is helpful for iodine adsorption. Zhang *et al*. [323] prepared a thiourea-modified PET derivative (PEI-SIA) with abundant N/S/O-heteroatoms and aromatic molecular fragments. Experimental results showed that iodine vapor adsorption capacity reached 6.48 g/g. Liu *et al*. [324] synthesized two aniline-based hyper-crosslinked polymers (AHCPs), exhibited the physical capture of iodine 2.5 g/g due to the rich primary amine group. Li *et al*. [325] constructed HCP using 2,4,6-triphenyl-1,3,5-triazine and pyrrole. The nitrogen-enriched HCP possessed 2.57 g/g iodine uptake capacity, which was ascribed to the synergistic interactions between iodine and the lone pair electrons on nitrogen as well as extended π-conjugations. Zhao *et al*. [326] constructed three porous organic polymers through Schiff base condensation reactions. Among them, POP-PDTE exhibited high I_2 adsorption (3.81 g/g). Xie *et al*. [327] fabricated six calix[4]pyrrole-based POPs based on Sonogashira-Hagihara cross-coupling reactions. Among them, C[4P-BTP constructed by calix[4pyrrole and bithiophene exhibited the largest iodine uptake both in vapor (3.38 g/g) and aqueous source (3.24 g/g in KI/I_2 solution). Wang *et al*. [328] used carbazole as the electron-rich center to construct a new porous organic polymer (CTF-CAR) based on Schiff-base polymerization. CTF-CAR exhibited an uptake capacity of 2.86 g/g for iodine vapor due to the strong electron donor ability and heteroatom binding sites. Huan *et al*. [329] constructed two cyclophosphazene-based inorganic-organic hybrid conjugated polymers (CPP-Tp and CPP-Pyr), which were equipped with dual electron-enriched π-conjugated blocks, exhibited iodine capture capacity up to 3.46 and 2.97 g/g, respectively. Niu *et al*. [330] presented a series of bisimidazole-based POPs (BisImi-POP@1-6). Among them, BisImi-POP@1 performed high iodine capture capacity up to 9.5 g/g, ascribing to a large number of imidazole N-heterocycle units in the skeletons.

Recently, Zhou *et al*. [304] reported two covalent organic superphane cages as non-porous amorphous adsorbents for the capture of iodine from water. In the static adsorption system, the cage showed up to 8.41 and 9.01 g/g iodine absorption capacity in I_2 aqueous solution and I_3^- (KI/I_2) aqueous solution, respectively, with a record-breaking iodine adsorption capacity. The single-crystal structure of SUPE-py-Imine-Cage showed that the water tetramer ($4H_2O$) was encapsulated in the lumen of the lantern-like superphane cage (Figure 9f). The expansion of the cage can further generate more intermolecular voids to capture more iodine (Figure 9g). This is reminiscent of the balloon blowing event. A limited gap is found inside and between the flat balloons, but a large gap can be seen inside between the blowing balloons. Fajal *et al*. [305] utilized a unique hybridization synthetic strategy and fabricated an amino-functionalized stable cationic discrete metal-organic polyhedra with dual-pore containing imine-functionalized COFs (Figure 9h). The ultra-light hybrid composite crystalline aerogel had a large surface area, hierarchical macro-micro pores and multi-functional binding sites. The adsorption capacities of the prepared adsorbents for iodine in the gas phase and water phase under static conditions were 9.98 and 4.74 g/g, respectively.

5.4 Mechanism and expectation

Compared with traditional inorganic porous materials such as zeolite and activated carbon, polymers have the advantages of cheap synthetic materials, lower skeleton density, larger specific surface area, good physical and chemical stability, and reusability, making them a promising class of porous materials in the removal of radionuclides in recent years. As mentioned above, it can be seen that the polymers can effectively separate radionuclides based on coordination

reaction and ion exchange process. Therefore, different organic building units can be selected based on the different effects of designing different functional polymers. For example, introducing relevant functional groups can improve the adsorption and selectivity of materials. After the design and synthesis, batch experiments, advanced spectroscopy analysis and theoretic calculations are used to check the effect and disclose the mechanism. In addition, in the process of designing polymers, full consideration should be given to the harsh environments required for practical applications, such as strong acids and base and complex competition ions. Since more and more attention is paid to removing radionuclides, it is believed that polymers will play a crucial part in the future.

6 Mxenes for radionuclides separation

6.1 Synthesis of MXenes

The deepening research on MXene synthesis mainly developed top-down and bottom-up methods, ranging from the use of acid etching of MAX phase precursors and other ternary layered carbides to non-etching methods, including chemical vapor deposition (Figure 10a) [331]. In 2011, Naguib *et al.* [332] used the etching agent HF for the first time to selectively etch Al atoms of Ti_3AlC_2 and synthesized multilayer Ti_3C_2. The MAX powder was added to the HF solution and stirred for a certain time. After centrifugation, it was washed with ultra-pure water several times to keep the pH between 4 and 6. Ghidiu *et al.* [333] first etched Ti_3AlC_2 with LiF and HCl to prepare Ti_3C_2 MXenes and Ti_3C_2 MXenes could readily be layered into flaked monolayer materials by handshaking with Li^+ insertion. The bottom-up method for preparing MXene includes CVD and atomic layer deposition. Halim *et al.* [334] displayed the method of Ti, Al, and C deposited Ti_3AlC_2 MXene thin film using direct current magnetron sputtering. The preparation of MXenes can lead to differences in morphology and surface terminations. The same MXene composition, after different post-treatment, modification of functional groups, annealing and chemical oxidation, can produce MXenes with different morphologies (Figure 10b) [335]. The formation of MXenes with different functional groups, interlayer spacing and oxidation stability is affected by the concentration of etchant, reaction temperature and time, reaction atmosphere and etching process (Figure 10c) [336]. MXenes are explored as promising candidates for radionuclides separation owing to their interesting physicochemical properties such as high surface area, abundant adsorption sites, high ion exchange capacity, good hydrophilicity and controllable interlayer space.

6.2 MXenes for uranium separation

As a new class of 2D materials, MXenes have relatively negative Zeta potential, abundant end groups and unique layered structure (Figure 11a) [337,338]. Based on this feature, researchers discussed the adsorption behavior and action mechanism of different types of MXenes on U(VI) from the perspective of the structure and composition of MXenes materials and found that the structure, composition and

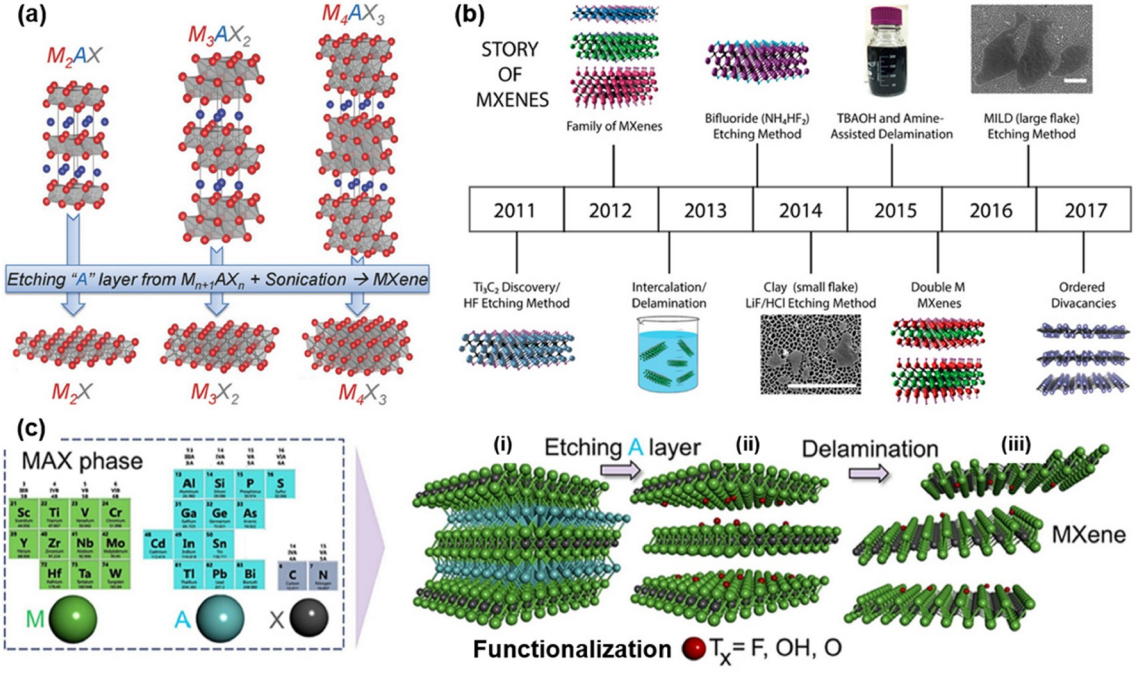

Figure 10 (a) Structure of Mxenes [331]. (b) Timeline of the preparation process for MXenes [335]. (c) The composition of MXenes phase elements and synthesis of few-layer XMenes strategy [336] (color online).

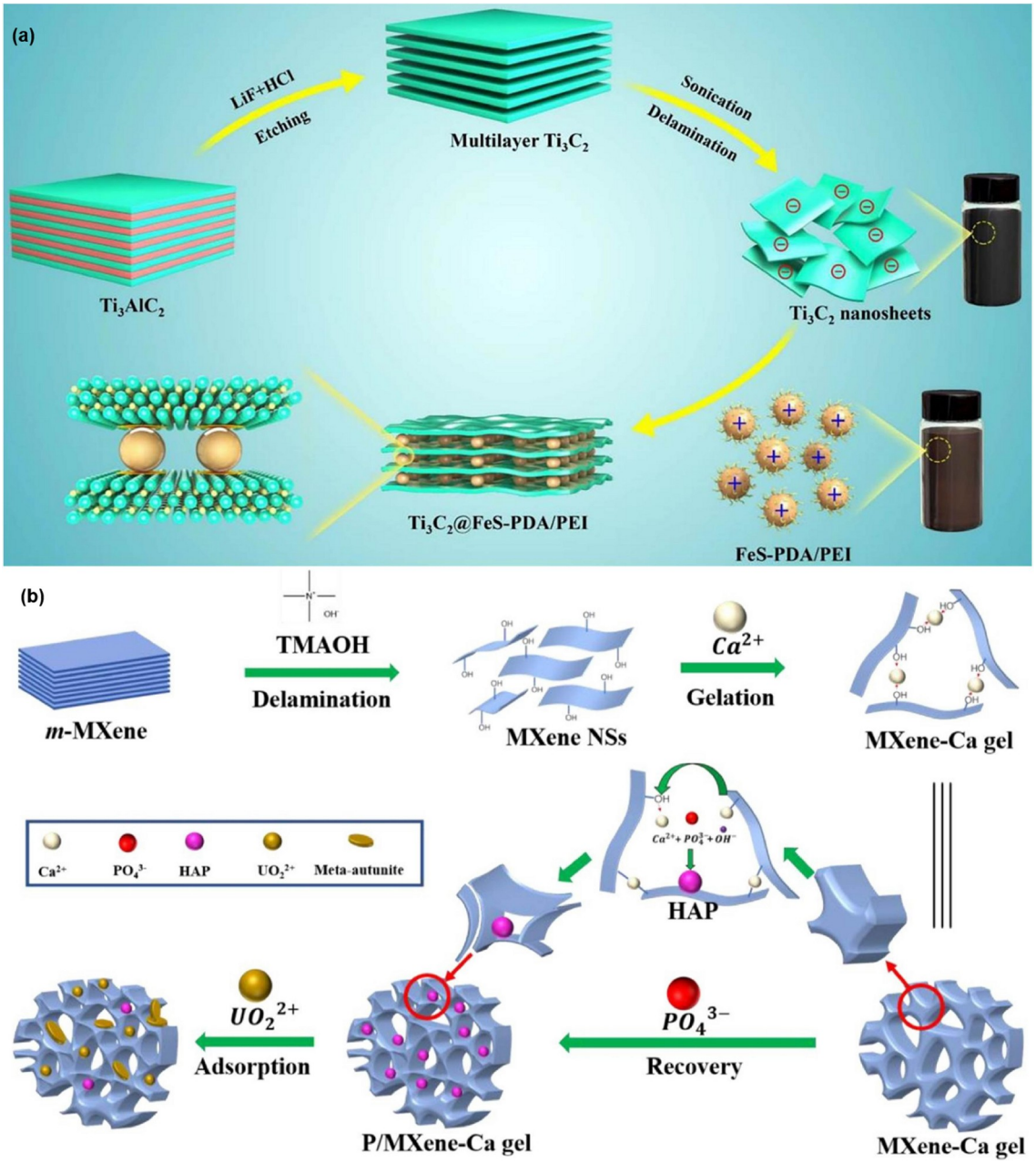

Figure 11 (a) Etching process of multiple-layer Ti_3AlC_2 [337]. (b) Schematic diagram synthesis and post-modification of MXene-Ca gel [341] (color online).

surface functional group content of MXenes played important roles in the process of removing radionuclides [339,340]. However, as an adsorption material, the structure of MXenes still has some shortcomings: the surface functional groups of MXenes itself are not very rich, and the active sites with special recognition functions are limited, resulting in poor selectivity for target pollutants. Due to the van der Waals and electrostatic force, the interlayer spacing of MXenes is small, which is not conducive to the mass transfer and diffusion of target pollutants, thereby affecting the adsorption performance. To solve this problem, the researchers used surface modification strategies to graft carboxyl, amino, amidoxime and other functional groups on the surface of MXenes to enhance the adsorption capacity and selectivity of MXenes to U(VI) ions. He *et al*. [341] developed a 3D porous MXene gel for the removal of U(VI), and MXene gel had excellent adsorption for U(VI) by 3D porous structure and rich adsorption sites (Figure 11b). Liu *et al*. [342] constructed a magnetic amidoxime-functionalized MXenes. The isotherm and kinetics data demonstrated that the elimination of radionuclides was a single-layer chemical adsorption process, and the calculation of thermodynamic data showed that adsorption was a spontaneous endothermic process.

6.3 MXenes for other radionuclides adsorption

MXenes can also be used to separate radionuclide Sr(II) from low-level radioactive wastewater. Shahzad *et al*. [343] exfoliated the Ti_2AlC MAX phase by a green hydrothermal alkalization approach to prepare various materials, which were used for Sr(II) adsorption and unveiled a maximum adsorption capacity of 296.46 mg/g. Zhang *et al*. [344] investigated the adsorption behavior of Sr(II) by multilayer Ti_3CNT_x MXene in wastewater. It was found that Ti_3CNT_x showed rapid kinetics and a broad active pH range of 3–12 (Figure 12a). Meanwhile, the adsorption capacity of Ti_3CNT_x was better than that of $Ti_3C_2T_x$ under the same conditions. Jun *et al*. [67] investigated the adsorption performance of Sr (II) on $Ti_3C_2T_x$ MXene from model wastewater (Figure 12b). This MXene exhibited outstanding uptake capacity and fast kinetics for Sr(II). XPS and FTIR analysis revealed that MXene adsorbed Sr(II) *via* ion exchange and inner-sphere complexation.

Europium (Eu) is one of the main fission products produced during the nuclear fuel cycle. As a typical trivalent lanthanide element, even low doses can seriously endanger human health. Zhang *et al*. [345] reported the preparation of hier-archical titanate nanostructures (HTNs) by *in-situ* chemical conversion strategy using 2D MXene crystal precursor (Figure 12c). These HTNs are very stable and can efficiently remove Eu(III) from the solution, owing to well-maintained layered structures and abundantly exchangeable guest cations. Liu *et al*. [346] reported the phytic acid-decorated MXenes@MOFs composites for the elimination of Eu(III) from water, and results showed that the developed adsorbent exhibited a maximum capture capacity of 368.1 mg/g for Eu (III), the elimination process happened on monolayer and dominated by chemisorption. The characterization analysis revealed that the interaction mechanism of Eu(III) on Nb_3C_4 @UiO-66-NH_2-PA was related to surface complexation and electrostatic attraction (Figure 12d). Furthermore, Shahzad *et al*. [347] developed a Prussian blue-coated MXene aerogel sphere by a simple synthesis method. The synthesized microspheres have special internal structures and high porosity. The oxygen functional groups on the surface of $Ti_3C_2T_x$ provide binding sites for the selective adsorption of Cs(I). Hassan *et al*. [66] developed hydroxyapatite ceramics as a host matrix, and used MXenes for green immobilization to simulate Cs(I) adsorption. Compared with pure MXenes, MXenes composites showed obvious thermal stability. The immobilization process used a low-temperature cold sintering method to prevent possible oxidation and chemical degradation of adsorbent. Compared with ^{238}U, the use of ^{232}Th produces fewer long-lived actinide fission products and would satisfy the world's energy demands for a longer period. However, the toxicity of Th(IV) can cause harmful diseases and serious effects on physiological functions, even

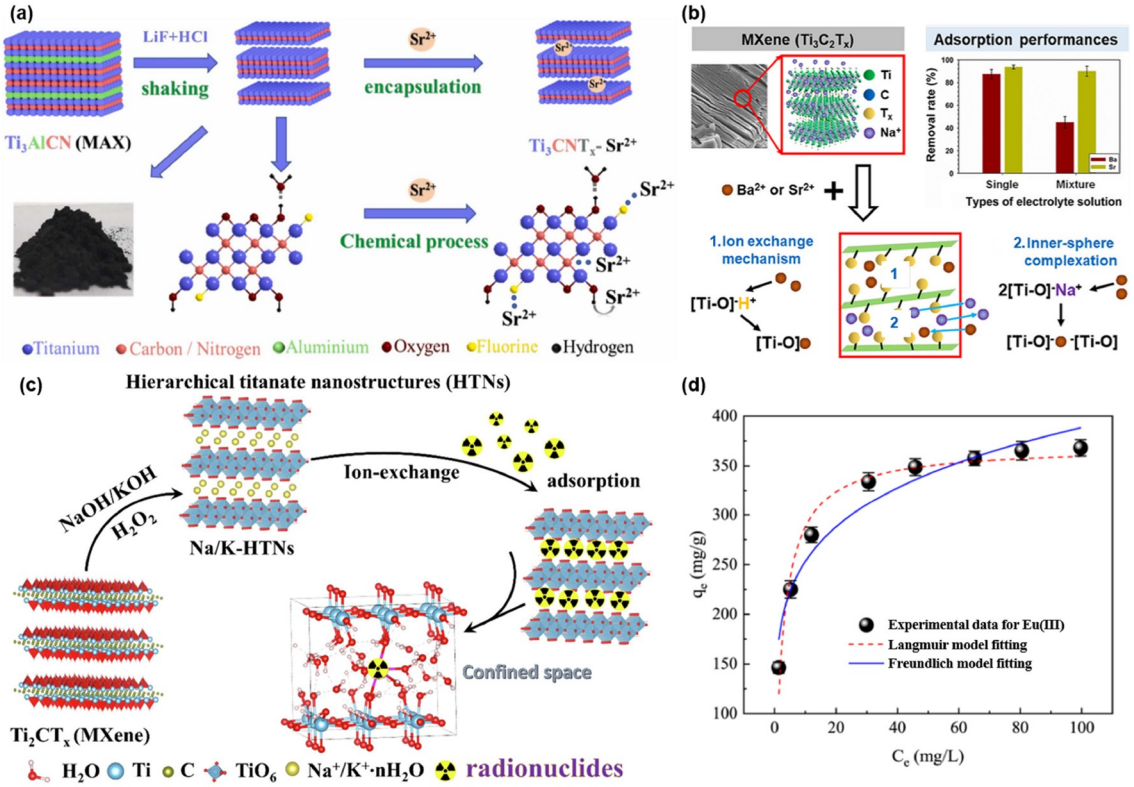

Figure 12 (a) Schematic diagram showing the adsorption mechanism of Sr^{2+} by Ti_3CNT_x [344]. (b) Mechanism diagram of Ba^{2+}/Sr^{2+} by $Ti_3C_2T_x$ [67]. (c) Synthesis schematic of hierarchical titanate nanostructures (HTNs) for adsorption radionuclides [345]. (d) Removal of Eu(III) by functionalized MXenes Nb_3C_4@UiO-66-NH_2-PA [346] (color online).

at trace levels. Nezami *et al*. [348] used phosphate-functionalized $Ti_3C_2T_x$ to efficiently remove Th(IV) from radioactive wastewater. The adsorption mechanism indicated that the adsorption process of Th(IV) was mainly based on electrostatic reaction and intra-sphere complexation. For the capture of $^{99}TcO_4^-$, the introduction of poly(diallyldimethylammonium chloride) adjusted the surface charge of Ti_2CT_x, improved the stability of Ti_2CT_x nanosheets, which were favorable for Ti_2CT_x nanosheets with high removal capacity and fast adsorption kinetics for $^{99}TcO_4^-$.

In summary, MXenes have been shown to be competitive inorganic adsorbents for environmental radionuclide capture and fixation. The removal mechanisms of radionuclides by MXene-based materials include electrostatic interaction, coordination, ion exchange and reduction immobilization. The adsorption characteristics are not only related to the water environment conditions but also have a close relationship with the layer structures, specific surface area, and surface chemical properties of MXenes materials. However, the powdered MXenes materials are not efficient in the separation of radionuclides. The separation process from the solution is cumbersome, difficult to recycle and has a low reuse rate. In addition, MXenes are often tightly reorganized by the hydrogen bond interaction between surface functional groups, which is not conducive to the mass transfer efficiency inside MXenes. The application of covalent grafting multifunctional MXene composites in the selective separation of radionuclides needs further study. Most of the current research focuses on the removal of radionuclides, and future research on other pollutants should be strengthened to expand the application range of MXene-based materials.

7 Porous carbon (PC) materials for radionuclides separation

7.1 Preparation and functionalization

As a member of the large family of porous materials, PC has broad prospects in the fields of water purification, gas separation, catalyst support, and electrochemical energy storage by virtue of their fascinating properties, like large specific surface area (SSA), controllable porous nanostructures, good mechanical, chemical and thermal stability [349]. According to the pore size, PC materials can be classified into four types: microporous < 2 nm, 2 nm ⩽ mesoporous ⩽ 50 nm, macroporous > 50 nm, and hierarchical-porous (micro-meso-macro pore). Based on various carbon precursors, PC materials can also be categorized into conventional fossil fuels-derived PC, biomass-derived PC, polymers-derived PC and MOF-derived PC [349,350].

To date, multifarious methods have been reported to prepare PC materials, mainly including the activation method [351,352], carbonization method [350,353] and template method [354–356]. The activation method, involving physical activation, chemical activation, or their combination, obtains PC through the reaction of carbon precursors with gaseous etchants (*e.g*., CO_2, NH_3, or H_2O) or chemical reagents (*e.g*., KOH, $ZnCl_2$, Na_2CO_3). The carbonization method gets PC by directly carbonizing precursors with inherent porous structures, such as ZIFs, MOFs, porous organic polymers, or biomass. The template method consists of hard templates (*e.g*., mesoporous silica, zeolite molecular sieves, aluminum oxide) and soft templates (*e.g*., organic molecules, supramolecular, amphiphilic polymers). PC can be acquired by removing various pre-existing sacrificial templates in precursors. Among these methods, the template method has aroused extensive attention since it can obtain a relatively uniform pore structure, which is highly demanded in separation and catalysis [356].

Functionalization of PC materials is essential for improving their application performance. Generally, two approaches can be used to functionalize PC materials: pre-designed functionalization and post-synthetic functionalization (Figure 13a) [357]. For the pre-designed functionalization, namely the bottom-up approach, functional species directly act as building blocks to assemble into porous materials. For instance, Liu *et al*. [351] adopted this approach to synthesize N, P and S co-doped carbon material. In the preparation process, the precursor polyphosphazene was first polymerized from the functional species, hexachlorocyclotriphosphazene, bis(4-hydroxyphenyl) sulfone and triethylamine, and then carbonized. For the post-synthetic functionalization, *i.e*., top-down approach, the porous structure is first synthesized, followed by a facile external modifications process to obtain the desired functionality. Li [358] and Chen *et al*. [359] used this approach to obtain phosphorylated hydrothermal carbon spheres and amidoxime-modified PC cloth electrodes, respectively.

In recent years, the unique properties of PC or functionalized PC materials have provided them with attractive opportunities to be utilized as adsorbents, electrocatalysts, photocatalysts, *etc*., to separate radionuclides from aqueous solutions [34]. Herein, based on different separation strategies, we systematically reviewed the recent works on radionuclide separation using PC-based materials since 2019.

7.2 PC for uranium separation

7.2.1 Adsorption

Adsorption is a well-established technology for separating U(VI) from water, with the advantages of low cost, easy operation, and strong practicality. The design of PC adsorbents with large SSA, suitable pore size distribution, and abundant active sites is the key to U(VI) extraction. Hence, most re-

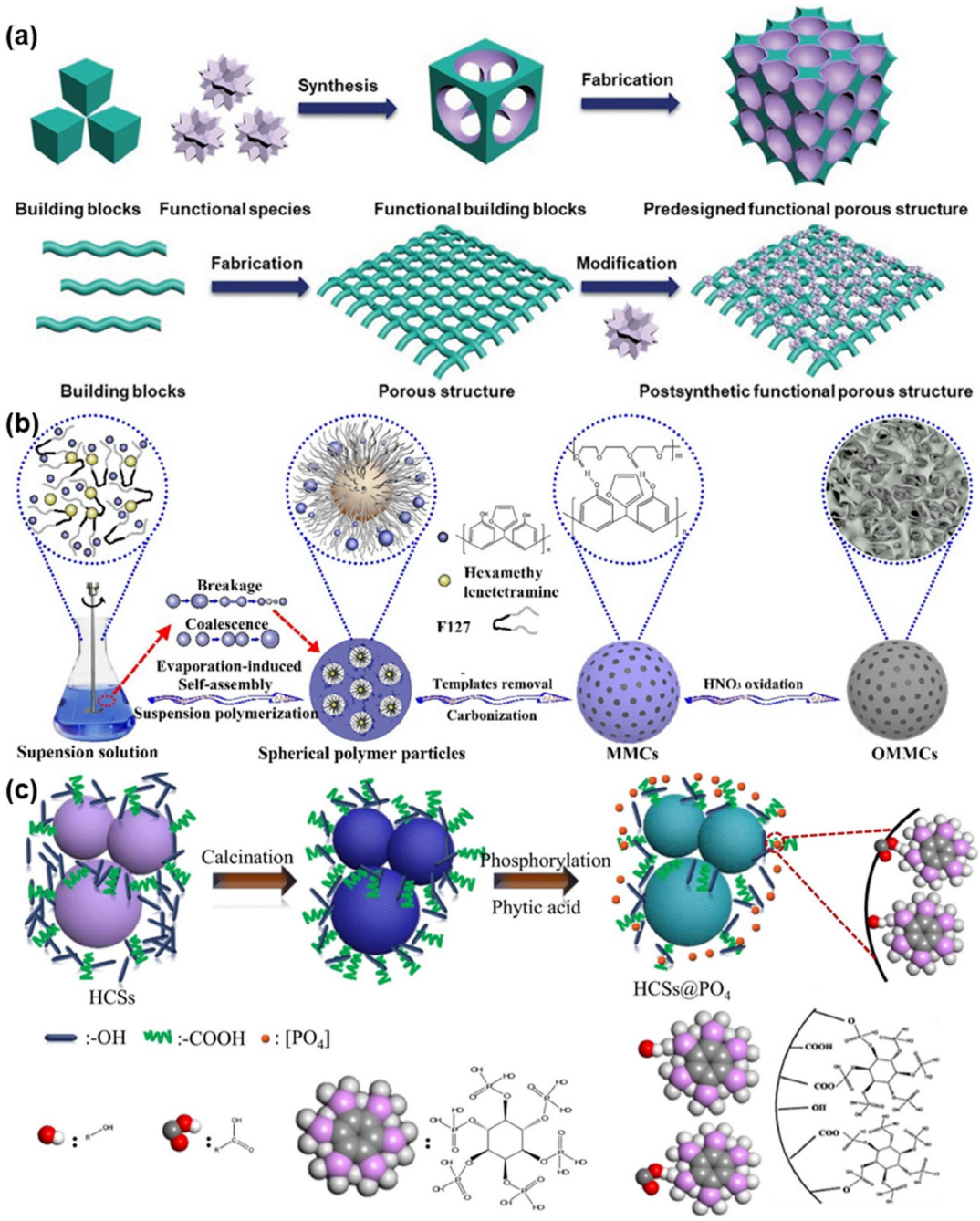

Figure 13 (a) Illustration of pre-designed functionalization and post-synthetic functionalization [357]. (b) Construction of oxidized millimeter-sized hierarchically porous carbon sphere [355]. (c) Schematic the preparation of phosphorylated hydrothermal carbon spheres [358] (color online).

search focuses on improving U(VI) adsorption performance by tailoring the pore structure, surface modification, and hybridizing or compounding with other functional components.

Among PC materials with different pore sizes, the hierarchical-pore PC is attractive since it balances both a high density and a low diffusional resistance toward active sites. The macropores act as transport highways, while the micro- and mesopores can offer large SSA loading active sites for U(VI) separation. Hence, PC adsorbents with a hierarchical pore size distribution are preferred and intensive research efforts are being directed toward this aspect [349,354,355]. For instance, Dong *et al*. [355] achieved U(VI) efficient removal by constructing functionalized millimeter-sized hierarchically porous carbon spheres (Figure 13b). In this work, spherical polymer particles were first fabricated through evaporation-induced self-assembly and suspension polymerization. The hierarchical pore structure was obtained by removing the template through carbonization. HNO_3 oxidation was followed to further increase the macro-porous vo-

lume and introduce oxygen groups on micropores. Finally, the as-produced hierarchically PC spheres exhibited a high BET SSA between 400–550 m^2/g and a large pore volume between 0.57–0.76, leading to a maximal U(VI) removal capacity of 232.45 at pH = 4.5 and 298 K.

Since some specific functional groups, such as phosphate [352,358], carboxyl [360], amidoxime [361], can form strong complexation with U(VI) ions, introducing functional groups on the surface of PC adsorbents is a common strategy to improve U(VI) adsorption performance. Li *et al*. [358] fabricated phosphorylated hydrothermal carbon spheres (HCSs@PO_4) by chemical grafting with phytic acid as a phosphorus source (Figure 13c). HCSs@PO_4 presented a strong inner-sphere surface complexation with U(VI), making its adsorption capacity up to 552.49 mg/g (pH = 5.0, T = 298 K), greatly outperforming that of HCSs (32.06 mg/g) and state-of-the-art materials. Similarly, Sun *et al*. [352] synthesized a phosphorylated honeycomb-like PC material (HLPC-PO_4) using activated orange peel as a precursor, which showed a maximum U(VI) uptake capacity of 552.6 mg/g, more than 3 times that of HLPC. Meanwhile, due to the strong bonding ability of –PO_4 to U(VI), the adsorption selectivity for U(VI) is also as high as 70.1%. In addition, Lai *et al*. [360] prepared solvothermal carbon-rich in carboxyl and phenol groups from crop straw, which also showed almost 100% U(VI) adsorption rate.

Hybridizing or compounding PC materials with other functional components as adsorbents can combine the merits of different materials and provide a good platform for U(VI) adsorption. Currently, many studies focus on loading metals and metal oxides, such as Fe, MgO, MnO_2, onto PC supports to enhance U(VI) adsorption [353,362–364]. For instance, Wang *et al*. [353] developed carbon-coating nano zero-valent iron using konjac glucomannan-derived carbon aerogel, which removed up to 90.1% U(VI) from 200 mg/L U(VI) wastewater in 60 min, with an enrichment capacity of 720.8 mg/g. During adsorption, the oxygen-containing groups of konjac glucomannan-derived carbon captured the UO_2^{2+} firstly, the electrons were transferred to carbon support, further reducing U(VI) to U(IV). Moreover, Lv *et al*. [362] reported that the evenly loaded MgO nano-particles onto N-doped carbon support can be quickly transformed to $Mg(OH)_2$, and an enhanced adsorption capacity (947.91 mg/g) can be obtained through the joint effect of complexation and ion exchange between Mg(II) and U(VI) ions.

7.2.2 Electrochemical method

Electrochemical method for U(VI) separation has its incomparable advantages, such as low energy consumption, fast kinetics, high adsorption capacity, no secondary pollution, and easy regeneration. Over the past five years, various PC-based electrode materials have been extensively used for U(VI) separation due to the high SSA and conductivity, mainly involving heteroatom-doped PC [34,361,365], conductive polymer-PC composites [359,366,367], transition metal oxide-PC composites [368,369].

Heteroatom doping can increase the number of binding sites for ions, improve the charge transfer ability and hydrophilicity of PC electrodes, thus beneficial for enhancing the catalytic activity of U(VI) and electrochemical extraction efficiency. Recently, Yang *et al*. [34] synthesized an Fe, N co-doped PC electrocatalyst (Fe-N_x-C-R), which consisted of N-doped carbon capsules supporting Fe-N_x sites and surface chelating amidoxime groups (Figure 14a). The surface of Fe-N_x-C-R electrode formed pale yellow flocs, a layer of dark yellow product covered the entire working electrode with the increase of extraction time and uranyl ions continued to be effectively converted into electrodeposited precipitates (Figure 14b). During extraction, the amidoxime groups offered surface-specific binding sites for UO_2^{2+} capture, while site-isolated Fe-N_x centers can effectively reduce adsorbed UO_2^{2+} into UO_2^{+}, and then re-oxidize UO_2^{+} to yellow $Na_2O(UO_3{\cdot}H_2O)_x$ deposits in the presence of Na^+ (Figure 14c). Similarly, Jin's group designed an *in-situ* Mn, N co-doped carbon nanospheres (Mn-NC) electrode through calcinating the Mn-polytriazine precursor. The resulting Mn-NC exhibited a U(VI) uptake capacity of ~194 mg/g at 1.8 V. The satisfactory adsorption performance originated from the fact that the N dopants within Mn-NC can coordinate with U(VI), while the Mn further enhances the polarity and charge transfer of the N-doped adsorption site, thus facilitating the removal process [365].

For electrochemical extraction of U(VI), PC materials may suffer from relatively low electrical double-layer (EDL) capacitance. Conducting polymers, like polyaniline, porous aromatic frameworks, polypyrrole, *etc*., which can store ions through pseudo-faradic reactions, frequently exhibit much higher pseudo-capacitance than EDL capacitance of carbon materials [359,366,367]. Hence, incorporating conductive polymer with PC is a useful strategy to enhance electrosorption performance. Through investigating the CV curves, Yu *et al*. [367] demonstrated cotton derived carbon/polyaniline electrode, which possessed higher specific capacitance (135.2 F/g) than carbon electrode (43.9 F/g), and can provide pseudocapacitance for U(VI) ion capture. A maximum U(VI) adsorption capacity of 282.2 mg/g at pH = 4.0 and 0.9 V was finally achieved. Chen *et al*. [359] constructed a self-standing PAF electrode (PAF-E) on carbon cloths, and the electroactive carbazoles in its structure could act as the redox sites to reduce UO_2^{2+} ions, thereby promoting U(VI) extraction. The PAF-E showed 3-fold faster kinetics than physicochemical adsorption, with an ultra-high removal capacity of 1413.9 mg/g from U-spiked seawater and an uptake capacity of 12.6 mg/g over 24 days in natural seawater.

Owing to the excellent electrochemical stability, high theoretical specific capacitance, multiple oxidation states,

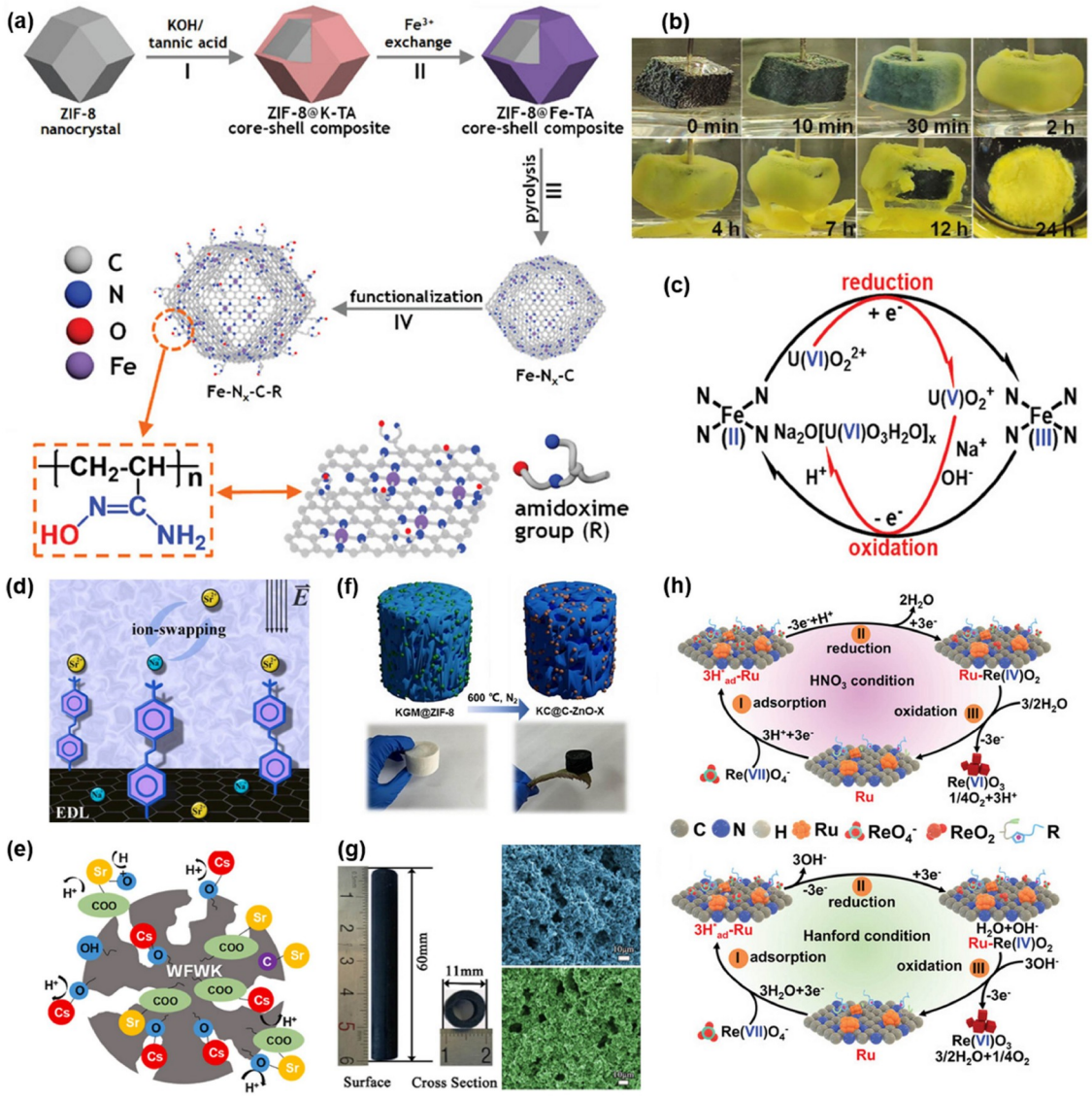

Figure 14 (a) Schematic synthesis of Fe-N_x-C-R. (b) Photographs of the Fe-N_x-C-R electrode in spiked seawater. (c) A plausible reversible electron transfer reaction mechanism [34]. (d) Electrostatic interaction between Sr^{2+} ions and anionic sulfonic group [380]. (e) Ion exchange between dissociated H^+ ions from -COOH and -OH and Cs^+ ions [374]. (f) U(VI) adsorption-photoreduction by ZIF-8-derived ZnO carbon aerogels [390]. (g) Photographs of CTCM tube and SEM images [382]. (h) Electrocatalytic extraction of ReO_4^- during the adsorption-electrocatalysis under various conditions [383] (color online).

various crystalline phases, environmental friendliness, *etc*., transition metal oxides are often combined with PC for U (VI) extraction. For example, Zhang *et al*. [368] synthesized a CC/γ-MnO_2-OVs electrode by growing MnO_2 on carbon cloth (CC), followed by the creation of oxygen vacancies (OVs) through the electrochemical method. Thanks to the interaction between Mn 3d orbital in CC/γ-MnO_2 and O 2p orbital in UO_2^{2+}, the OVs can increase the charge transfer and decrease binding energy between UO_2^{2+} and CC/γ-MnO_2, which made CC/γ-MnO_2-OVs display favorable selectivity, high adsorption capacity, and rapid kinetics towards U(VI). Zhou *et al*. [369] also developed a floriform WO_3/C composite for U(VI) removal. Based on the combination of WO_3 and carbon layer, the WO_3/C electrode exhibited a synergistic effect of EDL and pseudo-capacitance, producing a maximum U(VI) electrosorption capacity of 449.9 mg/g at 1.2 V.

7.2.3 *Photo-assisted methods*

In addition to adsorption and electrochemical methods, PC materials can also be used for photo-assisted U(VI) separation, mainly including photocatalytic reduction and photothermal methods. In these cases, PC materials are used as photocatalysts or photothermal conversion materials due to their large light-harvesting SSA, intrinsic broadband light absorption, good conductivity, excellent photocatalytic or photothermal conversion efficiency, and good photostability. Li *et al*. [370] fabricated C_3N_4/activated carbon composites

(CN/AC) for U(VI) reduction under visible light irradiation. Owing to the introduction of activated carbon, an exceptional boost in photocatalytic activity was observed for CN/AC composites, which was 70 times higher than the bulk g-C_3N_4. The enhanced photocatalytic activity enabled U(VI) to be efficiently reduced by photo-electrons and deposited at the edge of the CN/AC composite. Wan *et al*. [371] prepared a TiO_2/N-doped hollow carbon sphere (TiO_2/NHCS) for U(VI) removal. Benefitting from the cooperative effect of ideal energy level structure and Mott Schottky junction, TiO_2/NHCS exhibited above 90% removal efficiency, ~2.3 times the pristine TiO_2. For the photothermal method, Liu *et al*. [372] reported a monolithic MOF-bonded carbon sponge with photothermal enhanced U(VI) adsorption. By adopting a carbon sponge as an excellent photothermal conversion platform, the temperature of the adsorbent increased under light irradiation, thereby promoting the fast transport of U (VI) ions. After 4 weeks in natural seawater, U(VI) uptake increased by 32.37% compared to dark conditions.

7.3 PC for cesium and strontium separation

7.3.1 Adsorption

For Cs(I) and Sr(II) ions removal, the high porosity and diversified functional groups of PC adsorbents are conducive to obtaining high adsorption performance. Dong *et al*. [373] reported a millimeter-sized carbon-based supramolecular recognition material for selective adsorption of Cs(I). Attributing to the large SSA, reasonable macropore-mesoporous aperture distribution, and the host-guest molecular recognition between calix[4]biscrown-6 and Cs(I), this adsorbent showed Cs(I) adsorption capacity of 22.72 mg/g, outperforming most currently-reported adsorbents. Meanwhile, the adsorbent also displayed high selectivity to capture Cs(I) from coexisting ions. Since biochar is a promising and inexpensive adsorbent, intensive research has been devoted to enhancing the removal of Cs(I) and Sr(II) by endowing biochar with functionalities. Palansooriya *et al*. [374] demonstrated that the functional groups (–OH, $–NH_2$, and –COOH) in biochar facilitated the adsorption of Cs(I) and Sr (II). Hasan's team [375] achieved a high Cs(I) adsorption capacity of 133.54 mg/g by introducing diverse oxygen-containing –COOH, –C=O, and –OH groups on charcoal. In addition, Feng's group [376] and Hu's group [377] also observed enhanced adsorption of Cs(I) and Sr(II) through compositing biochar with Prussian blue or Mxene.

7.3.2 Electrochemical method

Since Prussian blue (PB) crystals have lattice spacing which is optimal for the hydration radius of Cs(I), PB (or analogues)-PC composites have recently emerged as one of the most promising candidates for Cs(I) selective removal. Park *et al*. [378] first demonstrated that core-shell structured PB-carbon nanofiber (PB-CNF) composites could effectively remove ^{137}Cs *via* the electrochemical method. Following that, they synthesized a series of CNF electrodes decorated with PB analogs (NiFe, CoFe, FeFe, and commercial PB). They found that NiFe PB-CNF exhibited higher electrochemical adsorption performance for Cs(I), and the adsorption process involved the reduction of Fe(III) in NiFe PB [379]. For the electrochemical removal of Sr(II), specific functional components have been reported to improve its selectivity. Xiang *et al*. [380] prepared an aryl diazonium salt of sodium 4-aminoazobenzene-4′-sulfonate (SPAC)-modified chestnut shell-derived PC material, the SPAC electrode showed superhigh Sr(II) selectivity of 70.65 against Na(I) in Na(I)-Sr(II) mixed solution with a molar ratio of Na(I):Sr(II) = 20:1. According to the analysis results, the high overlap of electron cloud between Sr^{2+} and $–SO_3^-$ endowed SPAC with the remarkable selectivity of Sr(II). Wang *et al*. [381] also reported a maximum Sr(II) removal efficiency of 99.5% and a maximum adsorption capacity of 668.9 mg/g by grafting specific crown ether molecules on carbon felt.

7.3.3 Membrane separation method

The PC-based electroactive membrane can also be adapted to selectively remove Cs(I) ions. From Rong's research [382], a nickel hexacyanoferrate (NiHCF) nanoparticle-loaded coal-based tubular carbon membrane (CTCM) exhibited an extremely high removal efficiency (over 99.99%), and extremely high Cs(I) selectivity even in the presence of high-concentration coexisting ion (*e.g*., Cs(I):Na(I) = 1:99, Cs(I):K(I) = 1:99). The rapid and selective Cs(I) uptake/release was ascribed to the good dispersion of NiHCF in the CTCM tube with high selectivity to adsorb Cs(I).

7.4 PC for other radionuclides separation

In addition to U(VI), Cs(I) and Sr(II), other types of radionuclides can also be efficiently eliminated by PC materials. Radioactive ^{99}Tc, present in the form of $^{99}TcO_4^-$, its selective removal from nuclear waste streams is technically challenging. Recently, Liu *et al*. [383] synthesized hollow N-doped carbon capsules loaded with ultrafine ruthenium clusters and then functionalized by a thin cationic polymeric network containing imidazolium-N^+ unit for efficient extraction of $^{99}TcO_4^-$. The imidazole cationic sites displayed a high binding affinity toward $^{99}TcO_4^-/ReO_4^-$, while the Ru clusters offered a reversible electron transfer platform to generate $^{99}TcO_3/ReO_3$ deposits. Eventually, the Ru@HNCC-R delivered a high extraction capacity, good $^{99}TcO_4^-/ReO_4^-$ selectivity, and long-term durability under extreme conditions. Guo *et al*. [384] also developed activated carbon-polypyrrole (AC-PPy) as an electrically switched ion exchange (ESIX) to remove ReO_4^- (as a surrogate of $^{99}TcO_4^-$). In this work, the ReO_4^- ions were adsorbed or released from the AC-PPy

composite by switching the potential to oxide and reducing PPy. Attractively, the ESIX treatment could be completed within 60 s, suggesting the rapid uptake and release of ReO_4^- ions.

Iodine species exist in solutions as the form of IO_3^- and I_3^- ions and in the dissolver off-gas stream as the form of highly volatile diatomic element I_2. Ma *et al*. [385] prepared lignin-based porous flower-like carbon nanosheets for the adsorption of iodine from iodine vapor and solution. The carbon nanosheets with micropores and mesopores showed high uptake capacity for I_2 vapor and aqueous solution. Through studying a series of N-doped PC (NBCs) for iodine adsorption, Wu *et al*. [386] found that the gaseous iodine adsorption was mainly determined by pore structure, especially micropores and narrow mesoporous and heteroatom-doping had limited influence on adsorption effect. In addition to pore-physisorption, it has been reported that bismuth-functionalized PC materials can also capture gaseous iodine by physisorption and chemisorption [387]. For the capture of iodine anions, silver-based PC [388] and heteroatom-doped PC [389] showed great potential.

7.5 Mechanism of PC for radionuclides separation

Studying the interaction and mechanism between PC-based materials and radionuclides is of great scientific significance for the rational design of carbon-based nanostructures for radionuclides separation. A considerable amount of spectral analyzes (such as EXAFS, TRLFS, XPS) and theoretical calculations have been utilized to investigate their interactions. So far, the most reported mechanisms include physical adsorption, surface complexation, electrostatic interaction, ion exchange, chemical reduction, and photo/electro-catalytic reduction/deposition.

Generally, physical adsorption shows relatively weak affinity to radionuclides and tends to occur around the pores mainly through Van der Waals forces and dipole moments. Relatively, surface complexation, mainly generated between radionuclides and surface functional groups of PC-based materials, shows a much stronger affinity to radionuclides. Based on this consideration, many studies have been devoted to increasing the density of surface functional groups (–COOH, –OH, $–PO(OH)_2$/$–PO(OR)_2$, $–C(NH_2)=N(OH)$, $–NH_2$), by activating PC materials or compounding with other functional components [352,374,391]. For some groups, such as –COOH and –OH, besides surface complexation, ion exchange can also take place between their dissociated H^+ ions and radionuclide ions (Figure 14e) [374]. For negatively charged $–SO_3^-$, $–COO^-$, $–PO_4^{3-}$ and other groups, electrostatic interaction can form between them and positively charged radionuclides (*e.g.*, UO_2^{2+}, Sr^{2+}, Cs^+) (Figure 14d) [380]. Moreover, by introducing multivalent metals or metal oxides on PC supports, the efficient separation of radionuclides, especially the enhanced selectivity, can be achieved through the chemical reduction (deposition) mechanism (Figure 14g) [353,364]. For the photocatalytic reduction, through tailoring the structure of photocatalyst, the generated photoelectrons can effectively reduce U(VI) ions into U(IV) deposits, such as UO_2 (Figure 14f) [370,371]. Usually, the photocatalytic reduction process can cooperate with the surface complexation mechanism for radionuclide separation.

Recently, with the electrochemical and photocatalytic reduction methods rapidly stand out, the photo/electro-catalytic reduction/deposition has also begun to be widely applied to separate radionuclides. Notably, Wang and his colleagues [34,361,383] conducted systematic study on the electrocatalytic reduction/deposition mechanism for radionuclides separation. In their work, a series of functionalized PC-based electrocatalysts were rationally designed to construct reversible electron transfer platforms, which can combine surface complexation with electrocatalytic reduction/deposition. During separation process, mobile radionuclides, *e.g.*, U or Re ions, were firstly to be selectively captured through binding groups, and then were rapidly electrocatalytic conversed to solid deposits *e.g.*, Na_2O-$(UO_3 \cdot H_2O)_x$ or $Re(VI)O_3$, on various catalytic sites through reversible redox pathways (Figure 14h).

7.6 Prospect of PC for radionuclides separation

Overall, PC materials have shown huge potential in the field of radionuclides separation due to their unique structural and performance characteristics. Through rationally tailoring the pore structure, surface functionalization or compositing with other functional components, the adsorption performance of PC materials, including adsorption capacity, kinetics, selectivity, stability and reusability can be further improved. Many technologies for efficiently capturing radionuclides using PC-based materials have been reported, mainly involving adsorption, electrochemical, and photo-assistant methods. Although great progresses of PC materials for radionuclide separation have been made, the following major challenges need to be addressed to further employ the full potential of PC-based materials in radionuclides separation.

First, from the perspective of material design, there exists a trade-off between specific surface area and chemical functionalization, which may lead to the impeded transportation of radionuclides. The hierarchical structure design with a uniform pore distribution and high concentration of active sites is highly needed. Second, from the angle of performance, the adsorption selectivity is still not high enough for the targeted radionuclides. Although the combination of surface modification of functional groups and photo/electro/chemical reduction could improve the selectivity, competition still exists in the selective adsorption process. The investigation of ultrahigh selectivity of viable PC-based materials is still in its infancy. Meanwhile, the stability and

reusability of PC-based material for extreme conditions, *e.g.*, strong acid medium, high ionic strength, and strong ionizing radiation, should be further considered. Third, from the viewpoint of mechanism, the relationship between the structure of PC-based materials and the capture mechanisms of radionuclide should be in-depth exploration at the molecular level. Advanced characterization techniques such as *in-situ* Raman, *in-situ* FTIR, and XANES/EXAFS are suggested to be fully exploited. Fourth, from the perspective of practical application, promising PC-based materials are still fabricated on a small scale or in laboratories, and convincing demonstrations of their utility for practical applications are lacking. Further study should be developed for large-scale synthesis of PC-based materials with high adsorption performance using low-cost, eco-friendly, and easy operation methods.

8 Graphene-based materials for radionuclides separation

8.1 Preparation of GO

Graphene-based materials have become one of the most potential materials for radionuclides separation owing to their high specific surface areas, tunable surface chemistry, and flexible morphology regulation. As an important graphene derivative, GO is easier to process and functionalize than initial graphene [392], so GO-based materials have attracted great attention in recent years. GO could be prepared through a series of graphite oxidative treatments, and the modified Hummer's method is one of the most commonly used methods for preparing GO [393]. Oxidative treatment equips GO with abundant oxygen-containing groups (such as hydroxyl, carboxyl, and epoxides), which provide coordination sites for radionuclides and increase the hydrophilicity [394]. As a result, GO could be directly utilized to separate radionuclides efficiently from aqueous solutions. Further, GO could be easily synthesized into different morphologies like microsphere, membrane, aerogel, and hydrogel. In this case, the specific surface area, porous structure, and mechanical property of GO could be regulated controllably so that GO could cope with different conditions of radionuclides separation. For example, introducing Eu^{3+} when preparing aerogel through reduction of GO could regulate the porous structure of aerogel, hierarchically porous structure caused by Eu^{3+} endowed rGO-Eu composite aerogel with great adsorption potential [395]. The porous membrane could also be used for separation. The membrane with different pore sizes prepared by the confined combustion method exhibited excellent separation performance of H_2O and D_2O [396].

8.1.1 Functionalization of GO

Although a part of radionuclides could be separated by pristine GO, disadvantages like poor coordination selectivity of oxygen-containing groups for radionuclides limit its practical application. The functionalization of GO through chemical reactions endows GO with particular function and utility, which increases the application prospect of GO efficiently. Covalent modification is the common strategy for introducing functional groups on GO. Abundant oxygen-containing groups serve as reactive sites during the modification [397]. Guo *et al*. [398] reported a flexible common method for covalent double functionalization of GO, which involved the ring opening of the epoxy ring and the subsequent reaction of the hydroxyl group with the benzoquinone, followed by the Michael addition of the amine derivative. Non-covalent modification is another simple but efficient method to functionalize GO. The high specific surface area of GO provided abundant modification sites for non-covalent. Among them, the sp^2 zone on GO was the ideal site for modification by π-π stacking; an aromatic compound like porphyrins could be easily modified on GO through π-π stacking [399].

8.1.2 Preparation of GO composite materials

Thanks to its high reactivity, GO is also used to prepare composite materials by combining with polymer, inorganic materials and MOFs, so that the separation ability for radionuclides of GO could be significantly improved [393,400]. The combination of GO and polymer is an efficient method to improve the specific surface area, porosity, mechanical strength, and conductivity so that the GO/polymer composite can be used for the electrosorption of radionuclides [401]. The introduction of inorganic materials like metal ions could equip GO with specific adsorption ability for certain radionuclide as well as regulate the morphology of GO. As a result, the self-assembly of GO-based aerogel induced by metal ions has been regarded as the common method for preparing GO composite aerogel [395]. Huo *et al*. [402] utilized metal ions (Mn^{2+}) and PVA to induce the self-assembly of GO to obtain GO-based composite aerogel. Mn^{2+} and PVA played a synergistic role in the gelation of composite aerogel. The introduction of Mn also enhanced the adsorption performance of Co^{2+} and Sr^{2+}. MOF is another commonly used material for preparing GO-based composite owing to its excellent adsorption property [403]. GO was easily combined with MOF through various flexible methods, such as the direct mixing method and *in-situ* synthesis method, owing to the high specific surface area and strong reactivity of GO [404]. Compositing with MOF-equipped GO with selective separation ability, reduced graphene oxide (rGO) hydrogel modified with ZIF-67 exhibited great adsorption selectivity and application potential for the removal of U(VI) [405].

8.2 Graphene-based materials for radionuclides separation

8.2.1 Separation of uranium

GO-based materials with high adsorption capacity and outstanding separation efficiency have been used to separate U (VI) from water with great success. Abundant O-containing groups (hydroxyl, carboxyl, and epoxides) endow GO with high adsorption ability for U(VI) [408]. Furthermore, the strong hydrophilicity of GO was also beneficial for the highly efficient separation of U(VI). Wang *et al*. [409] prepared GO nanoribbons (GONR) through oxidative unzipping. Unzipping introduced more O-containing groups on GO so that GONR possessed more adsorption sites for U (VI). The abundant adsorption sites of GONR caused the large adsorption ability of U(VI) at pH = 4.5 with the maximum adsorption amount (q_m) of 437.1 mg/g. Although pristine GO exhibited high adsorption amounts for U(VI), poor adsorption selectivity and excessive aggregation in aqueous significantly limits its further direct application [410].

Functionalization of GO and synthesizing GO into composite materials are efficient methods to overcome the abovementioned limitations. Modification of GO with functional groups that could combine U(VI) would specifically endow GO with selective adsorption ability for U(VI). Li *et al*. [406] prepared amidoxime-functionalized carboxymethyl β-cyclodextrin/graphene aerogel (GDC). The separation of U(VI) by GO-based materials could also be achieved by external stimuli such as light and electricity. The excellent electrical conductivity and unique 3D mesoporous channels of GO-based aerogels promote the electron and mass transfer in the catalytic process. GO-based aerogel performed well for photocatalytic separation of U(VI) with possessed q_m of 654.2 mg/g (Figure 15a). Wang *et al*. [411] prepared graphene aerogel (GA) with photocatalytic activity through the reduction of GO. GA could photocatalytic transform U(VI) into $(UO_2)O_2{\cdot}2H_2O$ under visible light irradiation and the removal capacity of U(VI) reached 1050 mg/g. Moreover, the outstanding reactivity allows GO to be prepared into composites other than aerogel, like membrane and sphere [412,413]. Li *et al*. [407] synthesized Anti-hydrogel, which showed an excellent adsorption capability of 9.2 mg/g in natural seawater after contact with natural seawater for 14 days (Figure 15b). EXAFS and DFT revealed the adsorption mechanism of phosphate-modified GO hydrogel to U(VI). EXAFS analysis suggested that one phosphate group was coordinated with one uranyl during the adsorption (Figure 15c). Further analysis of the DFT calculation confirmed the complexation configuration and mechanism (Figure 15d).

The preparation of rGO foam also shows excellent prospects for U(VI) extraction using the *in-situ* electrolytic deposition method. Wang *et al*. [58] prepared a functionalized rGO foam (3D-FrGOF) as the working electrode, and the functional groups on the graphene surface can form chelation binding with U(VI) ions (Figure 15e). In the photographs and SEM images of the 3D-FrGOF (Figure 15f), the surface of the foam is flat and the internal structural porosity increases the reaction surface area, which is conducive to fast U(VI) extraction. XRD pattern and DFT calculations show a quasi-2D $UO_2(OH)_2$ layer stacked pattern, and TEM images of the particles show the morphology of hexagonal-shaped thin disks (Figure 15g). The results show that the 3D-FrGOF electrode can be used for *in-situ* removal of U(VI).

8.2.2 Separation of thorium

Similar to the situation with U, Th could be adsorbed by O-containing groups on pristine GO [410]. In addition to O-containing groups, the defect of GO generated during the oxidation could also connect Th(IV) through the reaction of Th(IV) and electrons in the defect. GO nanoflakes (GONF) with abundant O-containing groups performed great adsorption ability for Th(IV) with the equilibrium adsorption of Th(IV) within 8 h, and GONF140 exhibited a high q_m for Th (IV) of 427.77 mg/g at pH = 3 [414]. In order to improve the separation selectivity for Th(IV), GO was functionalized with functional groups that could react specifically with Th (IV). Sreenivasan *et al*. [415] prepared a polymer-grafted nanocellulose/GO composite; the synthesized composite performed well for batch adsorption of Th(IV). The GO/polymer composite enhanced the adsorption ability of GO, providing the modification method for efficient separation of Th(IV).

GO-based aerogel and sphere were also utilized to separate Th(IV). Abundant porous structures of GO-based aerogel provided a mass transfer channel for Th(IV), causing the rapid adsorption kinetic, while high specific surface area and O-containing groups provided modification sites for functional groups. Chitosan is the common functional group for adsorption of Th(IV), GO/chitosan (GOCS) composite aerogel exhibited competitive adsorption kinetic with other inorganic materials and adsorption equilibrium was reached within 1 h at pH = 3 [416]. The GO-based sphere is the material that is efficient for the separation of Th(IV). The unique morphology of the sphere was beneficial for the continuous adsorption as a filler of the column. Shahr El-Din *et al*. [417] studied the separation performance of calcium/alginate-graphene oxide (Ca/Alg-GO) composite sphere for Th(IV). High specific surface area originating from porous structure and abundant O-containing groups caused the large adsorption amount for Th(IV), which was as high as 418 mg/g at pH = 2.

8.2.3 Separation of strontium and cesium

GO is usually functionalized to separate Sr(II) and Cs(I) because the adsorption performance of pristine GO is un-

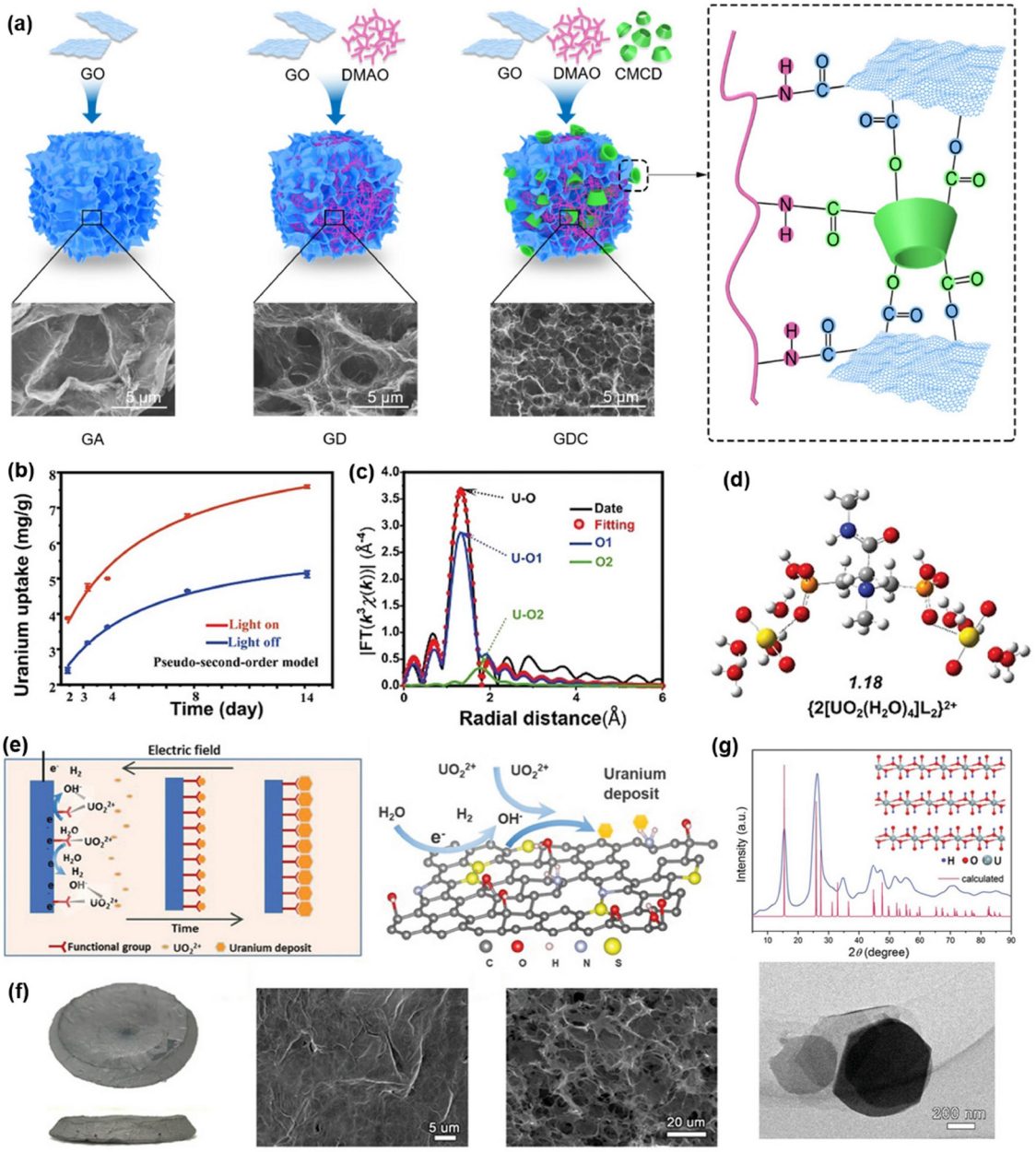

Figure 15 (a) Synthesis and SEM images of GA, GD and GDC [406]. (b) Adsorption performance of Anti-hydrogel in natural seawater, (c) EXAFS analysis of U(VI) binding with Anti-hydrogel and (d) optimized structure of one phosphate group coordinated with one UO_2^{2+} [407]. (e) Schematics of the electrolytic deposition process of uranium, (f) photographs and SEM images of 3D-FrGOF and (g) XRD and TEM of the 3D-FrGOF electrode after uranium extraction [58] (color online).

satisfactory. GO-based aerogel performed well as an adsorption tool for the efficient separation of Sr(II) and Cs(I) because it successfully circumvented the complicated separation issue of adsorption. Moreover, the 3D architecture of aerogel would boost the adsorption performance due to the enhanced accessibility of active sites resulting from macro- and mesopores of the 3D structure. Huo *et al*. [402] modified MnO_2 in PVA/GO aerogel. The introduction of MnO_2 increased adsorption sites for Sr(II) and q_m was enhanced to 26.85 mg/g with the adsorption equilibrium in 6 h.

PB is a important functional group owing to its satisfactory adsorption capacity and excellent adsorption selectivity for Cs(I) [378,379]. PB-functionalized GO aerogels were also useful separation materials for Cs(I), rGO/PVP/PB composite aerogel with porous structure performed well for adsorption of Cs(I) and exhibited high adsorption amount for Cs(I) with q_m of 143.88 mg/g [418]. PB-modified GO membranes were utilized for separation as well. Zhang *et al*. [419] modified porous GO/PVED membranes with PB by phase inversion. The modified membrane could selectively separate Cs(I) by membrane filtration in varieties of water systems like natural organic matter solution, surface water,

and tap water. The separation of Cs(I) with GO/PB composite provided practical application guides for the preparation of adsorption-filtration materials with great selective separation of Cs(I) and other radionuclides.

8.2.4 Separation of technetium and iodine

Separation of Tc is important for the treatment of radioactive water. Rhenium (Re), as a non-radioactive analogue with similar chemical properties to Tc, is often used to evaluate the separation performance of Tc [300]. In order to improve the practical application potential of GO-based materials, GO-based membranes and aerogel were prepared to separate Tc/Re. The intense hydrophily of GO limited its adsorption application because of the difficulty of separating it from the aqueous solution, so modification of GO through click reaction could inhibit this shortcoming efficiently. GO click membrane (GO-C) modified with Gemini ionic liquid performed outstanding adsorption ability for Re at the pH range of 3–10 with q_m of 238.67–269.17 mg/g [420]. Preparing GO into aerogel is another method to improve its adsorption performance and achieve favorable recycling. To evaluate the separation performance of GO-based aerogel for Tc/Re, Zhang *et al*. [421] prepared chitosan-modified GO aerogel (GO-CS) with high porosity. The abundant porous structure provided an abundant mass transfer channel of Re. Thus, GO-CS could adsorb more than 60% of Re within 20 min.

Pristine graphene and GO cannot adsorb iodine due to the lack of specific interaction sites, so functionalization is necessary for endowing graphene and GO with adsorption ability toward iodine. Modification of Ag is a feasible method owing to the excellent adsorption ability of iodine on Ag sites [422]. GO/Ag membrane was prepared by generating Ag nanoparticles on GO carboxylic acid sites *via* metal coordination. Composite GO membrane exhibited rapid adsorption kinetic for I^- and the adsorption equilibrium reached within 15 min with q_m of 150.2 mg/g [423]. Besides I^-, radioactive I_2 is also widely concerned because of its strong volatility [424]. Ag-modified graphene aerogel (GA/Ag) performed considerable adsorption capacities for both I_2 vapor and I_2 in solution [425]. Furthermore, modification of graphene by non-metallic elements is also a useful method for synthesizing iodine adsorbents. Liu *et al*. [426] reported that S, N co-doped graphene aerogel (SN-GA) could separate I_2 from water efficiently. Co-doping of S and N enhanced the interaction between I_2 and graphene structure, resulting in fast adsorption kinetic and high adsorption ability (q_m = 999 mg/g) of I_2 on synthesized aerogel.

8.2.5 Separation of other radionuclides

GO-based materials perform well when separating other radionuclides. Separation of actinides from acidic solution is important for the safe management of nuclear waste [428]. Functionalization of GO with the liquid complexing ligand is a useful method for equipping GO with selective adsorption performance for actinides. Modification of GO with liquid complexing ligands is helpful for the separation of actinides and rare earth elements. Modified GO not only performed high extraction degree for U(VI), Th(IV), and Pu(IV) in 3 mol/L HNO_3, but also could separate actinides selectively from the massive interfering ions [429]. In order to simplify the separation operation, it is necessary to prepare GO into membrane or aerogel owing to their unique morphology, which is beneficial for separation. Wang *et al*. [427] prepared a GO-based membrane with different interlayer spacing. The GO membrane exhibited excellent separation selectivity for actinides (U, Np, Pu, and Am) from lanthanides in HNO_3 solution through ion sieving effect (Figure 16a–c), which can block the larger and linear actinyl ions, but allows smaller and spherical lanthanide ions to penetrate and achieve the separation factor of lanthanide/actinide ions as high as 400.

Lithium (Li) and deuterium (D) are important materials in the nuclear industry, and the GO membrane could be used to selectively separate Li and D through the sieving effect of the GO-based membrane [430,431]. Liang *et al*. [396] prepared a GO-based membrane containing porous graphene. The GO-based membrane exhibited an excellent D_2O rejection rate of 97.02% (Figure 16d). The viscosity difference between D_2O and H_2O effectively slowed down the flow rate of D_2O between GO/PG-3/GO membranes with a three-layer sandwich structure (Figure 16e). Furthermore, the D and H on the hydroxyl group undergo isotope exchange. At the same time, the dense membrane structure of GO effectively prolongs the permeation rate of the solution and effectively adsorbs D_2O, thereby improving the selectivity. Further, introducing MOF with excellent adsorption performance is helpful for endowing GO with separation ability for Li. Liu *et al*. [432] modified the GO membrane with ZIF-8/zinc alginate and created a tunable interlayer channel with a ternary heterostructure. The membrane displayed remarkably excellent Li selective separation ability through ion-sieving. The selectivity values of Li/K and Li/Mg reached 20.9 and 9.5, respectively.

8.3 Mechanism of GO for radionuclides separation

Knowledge of the separation mechanism of radionuclides is imperative for the treatment of nuclear waste and the design of novel separation materials. Herein, separation mechanisms containing functional group complexation, photocatalytic oxidation/reduction, ion exchange, and size sieving are summarized.

8.3.1 Functional group complexation

Functional group complexation is the main mechanism for the separation of radionuclides by GO-based materials.

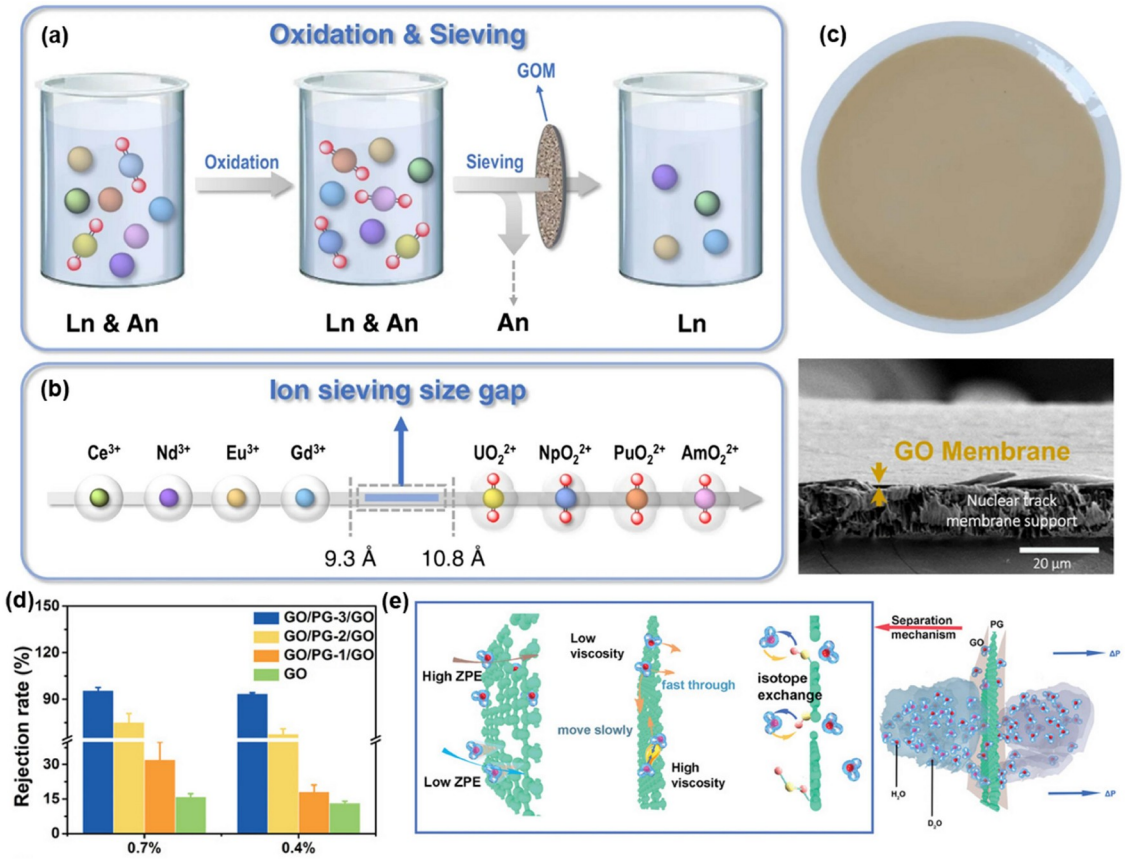

Figure 16 (a) Scheme of actinides/lanthanides group separation. (b) Representative lanthanide and actinide ions and (c) digital photo and cross-sectional SEM image of the GOM [427]. (d) Rejection rates with GO heterostructure membranes for the H_2O/D_2O. (e) Mechanism of GO/PG/GO separation to H_2O/D_2O [396] (color online).

Oxygen-containing groups on GO could react with various radionuclides through complexation. Investigating the complexation mechanism between O-containing groups and radionuclides is important for designing GO-based materials for the separation of radionuclides. Gao *et al*. [414] investigated the binding behavior of O-containing groups (–OH, –COOH, and –COC) on GO to Th(IV) through DFT calculation. DFT calculation showed that Th(IV) coordinated well with O-containing groups at the various positions on the surface of GO. Negative adsorption energies indicated the strong Th(IV) binding ability of O-containing groups. This provided a reference for the complexation between GO and radionuclide. The spectroscopic technique is another useful method for revealing the adsorption mechanism. The analysis of EXAFS spectra allows for a conclusion to be made on the local atomic environment of adsorbed radionuclides. When studying the complexation mechanism between defect-rich GO and U(VI) through EXAFS spectroscopy, complexation information provided by the spectrum showed that carboxylic on GO dominated the GO-UO_2^{2+} interaction [433].

8.3.2 *Photocatalytic oxidation/reduction*

Photocatalysis-assist separation is an efficient method for separating U(VI) with the help of external stimulus. Oxidative (H_2O_2) or reductive species (e_{aq}^-) could be generated with the assistance of GO-based catalysts. These reactive species would transfer U(VI) into insoluble products subsequently so that U(VI) was separated from the aqueous solution. Due to the conjugate π structure and conductivity, the GO-based photocatalysts have been widely designed for the efficient removal of U(VI). Wang *et al*. [411] explored the photocatalysis-assist precipitation of U(VI) by graphene aerogel. Characterization of photocatalytic products declared that U(VI) was transferred into insoluble $(UO_2)O_2{\cdot}2H_2O$ by graphene aerogel-induced photocatalytic precipitation. Further study of EPR spectra indicated the formation of active ·OH radicals. Subsequently ·OH was formed H_2O_2 and H_2O_2 transferred uranyl into $(UO_2)O_2{\cdot}2H_2O$. In addition to photocatalytic oxidation, photocatalytic reduction of the soluble U(VI) to the insoluble U(IV) is widely used to separate U (VI) as well. The introduction of photocatalysts on GO is the key point for separating U(VI) through photocatalytic reduction. g-C_3N_4 is the ideal candidate owing to its excellent photocatalytic performance [370]. Wu *et al*. [434] separated

U(VI) through photocatalytic reduction by C_3N_5/rGO aerogel, C_3N_5 generated photogenerated electrons and holes under visible light irradiation, then the injection of photogenerated electrons into the surface of rGO improved the separation and migration for photoexcited carriers. Subsequently, photogenerated electrons were captured by U(VI) and reduced U(VI) into insoluble U(IV). The photocatalytic method has been regarded as a promising strategy and has been extensively applied to the separation of U(VI) from the solution.

8.3.3 Other mechanism

Ion exchange reaction is the main mechanism for the adsorption of anionic radionuclides like $^{99}TcO_4^-$/ReO_4^-. The decoration of ion exchange units to GO-based materials could grant GO the prominent ability to anion separation. Wang *et al*. [420] studied the adsorption mechanism of ReO_4^- on GO click membrane modified with imidazolium ionic liquid by chemical characterization and DFT calculation. Change of XPS N 1s spectra for imidazolium after adsorption indicated that it was C–N^+=C instead of C–N=C interaction with ReO_4^-, while the decrease of chloride content after adsorption confirmed the ion exchange reaction between Cl^- and ReO_4^-. The adsorption energy of ReO_4^- was obtained as −255.96 kJ/mol by DFT calculation, turning out that the adsorption process was spontaneous and efficient.

Sieving based on size effect could separate certain radionuclides selectively. Thus the 2D layer structured GO is suitable to construct a membrane containing vertical heterojunction and nano-channel structure. When nano-channel or interlayer spacing of GO in the size gap between different radionuclides, certain radionuclide could be bolded back by GO while others penetrated GO. Thus, selective separation would be achieved. Wang *et al*. [427] prepared GO membrane (GOM) with a nano-channel size of 10.5 Å, which sits in the size gap between hydrated actinyl ions and lanthanides ions. GOM exhibited outstanding selective separation ability for actinides from lanthanides through the sieving effect. As a novel strategy for separating certain radionuclide selectively, sieving based on size effect exhibited great application potential for large-scale separation of radionuclides, and preparation of membrane with specific porosity for sieving is the point for separation of radionuclides.

The separation of iodine by graphene-based materials mainly depends on the generation of solid products by the interaction between iodine and functional units. Modification of Ag is the most common method for adsorption of iodine. Chen *et al*. [423] studied the adsorption mechanism of I^- ions on GO/Ag composite. The results showed that GO/Ag adsorbed I^- through the interaction of Ag with I^- to form the AgI solids. Functionalization of Bismuth (Bi) on GO-based material is a novel method for iodine adsorption. Chee *et al*. [435] researched the adsorption performance of I_2 vapor on Bi^0-rGO and investigated the adsorption mechanism. Bi^0 could react with I_2 vapor into BiI_3 solid that deposited on rGO. Thus Bi^0-rGO exhibited outstanding adsorption performance for I_2 vapor. To improve the adsorption ability of iodine by GO, synthesizing GO-based aerogel is also a useful method owing to the large specific surface area and high porosity.

8.4 Prospect of graphene-based materials for radionuclides separation

Graphene-based materials are ideal materials for the separation of radionuclides owing to their diverse structures, high reactivity, and great separation performance [436,437]. This section highlighted the synthesis of graphene-based materials such as graphene-based aerogel, membrane and sphere, and their separation performance and mechanism for U(VI), Th(IV), Sr(II), Cs(I) and other radionuclides were discussed. Obviously, the functionalization of graphene sufficiently enhanced its separation performance, and materials with different morphologies could meet different separation requirements. Although the milestones have been achieved in the path of separation of radionuclides by graphene-based materials, a lot of work is still to be done to improve the separation properties and promote practical application, including (i) in the process of separation of radionuclides by graphene-based materials, the effect of chemical groups on separation is mainly studied, while the synergetic effect of complexation and topological structure of GO-based materials is seldom studied. It would be necessary to explore the synergetic effect of porous structure and morphology regulation on improving separation properties; (ii) external stimulus such as light, electric field, and magnetic field could be utilized to assist the separation of radionuclides, endowing graphene-based materials with optical, electrical, and magnetic response ability will be helpful for improving their separation performance; (iii) radionuclides usually exist in harsh environments with strong acid, high temperature, and strong radioactivity, studying the stability and separation performance of graphene-based material in such harsh environments is important for evaluating the practical application property; and (iv) the separation performance of graphene-based materials for radionuclides in real radioactive wastewater is still need to be further investigated, the performance of graphene-based materials in industrial application for separating radionuclides also remains to be explored.

9 g-C_3N_4 for radionuclides separation

9.1 Basic introduction of g-C_3N_4

g-C_3N_4, as a non-metallic organic polymer semiconductor material, has attracted wide attention in the field of radionuclides separation due to its outstanding advantages such as a broader light absorption range, strong controllability of molecular structure, high physicochemical stability, appropriate band structure, and simple preparation methods [438]. The C and N atoms in the structure of g-C_3N_4 form a highly delocalized π-conjugated system through sp^2 hybridization, while the interlayer structure is formed in a π-π stacking manner. This π-conjugated structure is extremely advantageous for the transmission and migration of photoinduced carriers in the bulk phase, which is crucial for accelerating the rate of photoreactions. Thanks to the above advantages, g-C_3N_4 has become one of the popular catalysts in the field of radionuclides separation. As is well known, g-C_3N_4 is usually prepared by thermal polymerization of precursor materials. A variety of precursor materials for the synthesis of g-C_3N_4 have been reported, typically derived from widely available and inexpensive precursors such as melamine [439], cyanuric acid [64], urea [65], thiourea [440], and dicyandiamide [78,370]. The synthesis of g-C_3N_4 generally involves two steps. Firstly, the precursor undergoes polymerization to form melamine at 335 °C. And then, as the temperature rises to approximately 390 °C, melamine loses amino groups and rearranges to form heptazine rings, ultimately forming g-C_3N_4 polymer at 520–550 °C [441]. It is worth noting that g-C_3N_4 becomes unstable, and the heptazine ring framework gradually collapses above 600 °C. At temperatures above 700 °C, g-C_3N_4 completely decomposes into small molecules such as CO_2 and NH_3. Therefore, differences in preparation conditions such as precursor type, pyrolysis temperature, and heating rate can cause significant differences in particle size, pore volume, and specific surface area of the g-C_3N_4 product. Moreover, the distinct morphological structures significantly influence the physicochemical properties of g-C_3N_4, leading to differences in the separation performance of radionuclides. Therefore, this section systematically summarizes the modification strategies of g-C_3N_4-based materials and their research progress in the field of radionuclides separation.

9.2 g-C_3N_4 for uranium reduction

In recent years, g-C_3N_4-based photocatalysts have flourished in the research on the deep purification of U-containing wastewater and U(VI) extraction from seawater due to the unique advantages of non-metallic semiconductors [442]. However, traditional g-C_3N_4 has some shortcomings, such as a lack of active reaction sites, low efficiency of photogenerated charge separation, and narrow spectral utilization range, which severely limit its practical application in photocatalytic U(VI) extraction [443]. To develop and design g-C_3N_4-based photocatalysts with excellent U(VI) extraction performance, researchers have adopted various effective material modification strategies to address the challenges faced by traditional g-C_3N_4. So far, several modification strategies have been proposed, including element doping [444], structural regulation [78], functional group grafting [445], and heterojunction construction [446]. These strategies have been proven to optimize the band structure of g-C_3N_4, broaden the spectral absorption range, and improve the separation and migration of photogenerated charge carriers, thereby significantly enhancing the photocatalytic performance of g-C_3N_4 [447,448]. Developed g-C_3N_4-based photocatalysts have achieved impressive progress in the research field of efficient U(VI) separation and enrichment. Next, the main modification strategies and key parameters influencing the photocatalytic performance will be elaborated in detail, providing useful guidance for further development of g-C_3N_4 with excellent photocatalytic performance.

9.2.1 Element doping

Introducing metal or non-metal elements into the plane or interlayer of g-C_3N_4 through doping is an effective method to adjust its physicochemical properties. For example, element doping can improve physical and chemical properties such as charge transfer rate, material conductivity, light absorption, and molecular structure. These changes in properties play a crucial role in the photocatalytic performance of the catalyst during the extraction process of U(VI). Chen *et al*. [449] reported a novel O and K co-doped g-C_3N_4 (OKDCN) for efficient photo-assisted U(VI) removal under aerobic conditions without sacrificial hole scavengers. The co-doping of O and K effectively regulated the band gap of g-C_3N_4, enhancing the conduction band potential of g-C_3N_4. Furthermore, the co-doping of O and K caused the redistribution of electron clouds within the g-C_3N_4 molecule, forming new local charge centers, which improved the efficiency of electron-hole pair separation. Therefore, the synergistic effects of higher electron energy, narrower band gap, and higher charge separation efficiency enhanced the photoreduction performance of OKDCN, achieving higher efficiency in the removal of U(VI).

Nie *et al*. [450] reported Cu-doped g-C_3N_4 (Cu-CCN) with high surface area for photo-assisted U(VI) removal. Cu-doping caused the effective separation of charges and upward shift of valence and conduction band potentials, resulting in a narrow band gap and increasing the photocatalytic activity of Cu-CCN towards U(VI). The optimal Cu-CCN-50 exhibited a photocatalytic removal efficiency close to 100% within 10 min of irradiation time and demonstrated stable cycling performance. To further enhance the photocatalytic activity and adsorption capacity of C_3N_4 photocatalysts, Liu *et al*. [451] prepared a novel dual-functional C_3N_4 material (CN550) doped with Zn-Cl through a molten salt method, which possesses more abundant ad-

sorption sites and a higher specific surface area (75.6 m^2/g). Compared with pristine g-C_3N_4, CN550 exhibited significantly higher adsorption and photocatalytic activity. The U(VI) extraction capacity of CN550 is as high as 1,556 mg/g, and the removal rate in real seawater is up to 98.7%.

9.2.2 Functional group grafting

Introducing functional groups (such as –OH, –COOH, –CNOH, –CN) into g-C_3N_4 is the most practical method for directly enhancing the adsorption and photoreduction performance towards U(VI). For instance, the introduction of strong electron-donating groups, such as carboxyl, cyano, and amidoxime groups, not only serves as adsorption sites for uranyl ions but also as photoreduction sites, enhancing the charge separation efficiency of g-C_3N_4, thus significantly improving the adsorption and reduction performance of U(VI) [64,443,445,452]. Although g-C_3N_4-based materials have demonstrated effective photoreduction of U(VI), previous efforts have focused on enhancing the adsorption capacity or photoreduction performance toward U(VI) by promoting photon-generated carrier separation. Currently, little attention has been paid to the inconsistency between the adsorption and reduction sites of U(VI) on photocatalysts. This disparity significantly prolongs the distance required for photo-generated electrons from the accumulation area to the adsorption sites of U(VI), resulting in the loss of photoelectrons. Therefore, it is crucial to design an advanced photocatalytic material with adsorption and photoreduction co-locating sites to achieve efficient U(VI) extraction activity. Yu *et al*. [453] successfully designed amidoxime g-C_3N_4 (AO-g-C_3N_4), achieving efficient U(VI) adsorption and photoreduction extraction from seawater (Figure 17a). For AO-g-C_3N_4, amidoxime groups not only serve as coordination sites for U(VI), but also significantly enhance the visible light absorption capability and charge carrier separation efficiency of AO-C_3N_4 by introducing defect energy levels, rendering AO-C_3N_4 with excellent photocatalytic activity and antibacterial properties (Figure 17b, c). Building upon this foundation, Hu *et al*. [64] further developed a cyanogen-functionalized g-C_3N_4 (g-C_3N_4-CN) with an isosite structure of adsorption and photoreduction for U(VI), achieving efficient photo-assisted U(VI) extraction from seawater. As the key of the isosite structure, the cyano group not only significantly promotes the separation of photogenerated charges of g-C_3N_4-CN but also greatly improves the adsorption capacity and selectivity for U(VI). Consequently, g-C_3N_4-CN demonstrates efficient photo-assisted U(VI) reduction performance, with a saturated U(VI) extraction capacity of 2,644.3 mg/g, significantly higher than most reported g-C_3N_4-based photocatalysts. In conclusion, the introduction of active moieties on g-C_3N_4 plays a pivotal role in enhancing the adsorption and photoreduction performance of U(VI) (Figure 17d).

9.2.3 Heterojunction engineering

Due to its practicality and effectiveness in spatially separating electron-hole pairs, heterojunction engineering has been demonstrated as a promising approach to constructing photocatalysts for enhancing charge separation efficiency [454]. Constructing heterojunctions by combining g-C_3N_4 with other materials (such as WO_3 [439], GO [455], CdS [456,457], $ZnFe_2O_4$ [458]), the optical response range of the composite material can be expanded, thereby enhancing the light absorption efficiency of the photocatalyst. At the interface of the heterojunction, electrons and holes will be effectively separated in space due to band bending and modulation, thereby improving the charge separation efficiency. For instance, Chen *et al*. [459] synthesized g-C_3N_4/GO hybrid nanosheets (g-C_3N_4/GO) using ultrasound-assisted method for the purification of U(VI)-containing organic wastewater. Due to the staggered band structure, electrons generated on g-C_3N_4 are transferred to GO, thereby achieving synchronous heterotopic organic oxidation and U(VI) reduction. Li *et al*. [456] reported a CdS/g-C_3N_4 heterojunction with U(VI) removal efficiency up to 95% within 6 min under sacrificial free conditions, which is the fastest reduction in the report. Most importantly, the U(VI) extraction capacity of CdS/g-C_3N_4 reached 2,379 mg/g, and the recovered CdS/g-C_3N_4 nanocomposite material still maintained high stability and activity post-reaction. Furthermore, the main obstacles remain the use of protective gases and additional sacrificial agents in the photoreduction of U(VI). In response to the above issues, Wang's team [460] developed a bifunctional WO_x/g-C_3N_4 catalyst with oxygen vacancies for selective oxidation of benzyl alcohol and simultaneous reduction of U(VI) without the need for protective gas or sacrificial agents. The removal rate of U(VI) achieved 98.5%, the conversion rate of benzyl alcohol was close to 32%, and the selectivity was close to 100%. Compared to pristine g-C_3N_4 and defect-free WO_3, the photoreduction activity of WO_x/g-C_3N_4 was 10.4 times and 7 times higher, respectively. Furthermore, heterogeneous structure photocatalysts such as $LaFeO_3$/g-C_3N_4 [370], $ZnFe_2O_4$/g-C_3N_4 [458], MoS_2/g-C_3N_4 [461] have achieved efficient U(VI) removal performance.

9.2.4 Mechanism of uranium reduction and separation

The basic process of photocatalytic reactions is summarized in three main steps: photon absorption, charge carrier separation, and interfacial reactions. Firstly, the range of light absorption is determined by the band gap (E_g) of the photocatalyst itself. Only when the energy of the incident photons is greater than the E_g of the semiconductor ($h\nu > E_g$), the photocatalyst can be excited, causing electrons to transition from the valence band to the conduction band and leaving

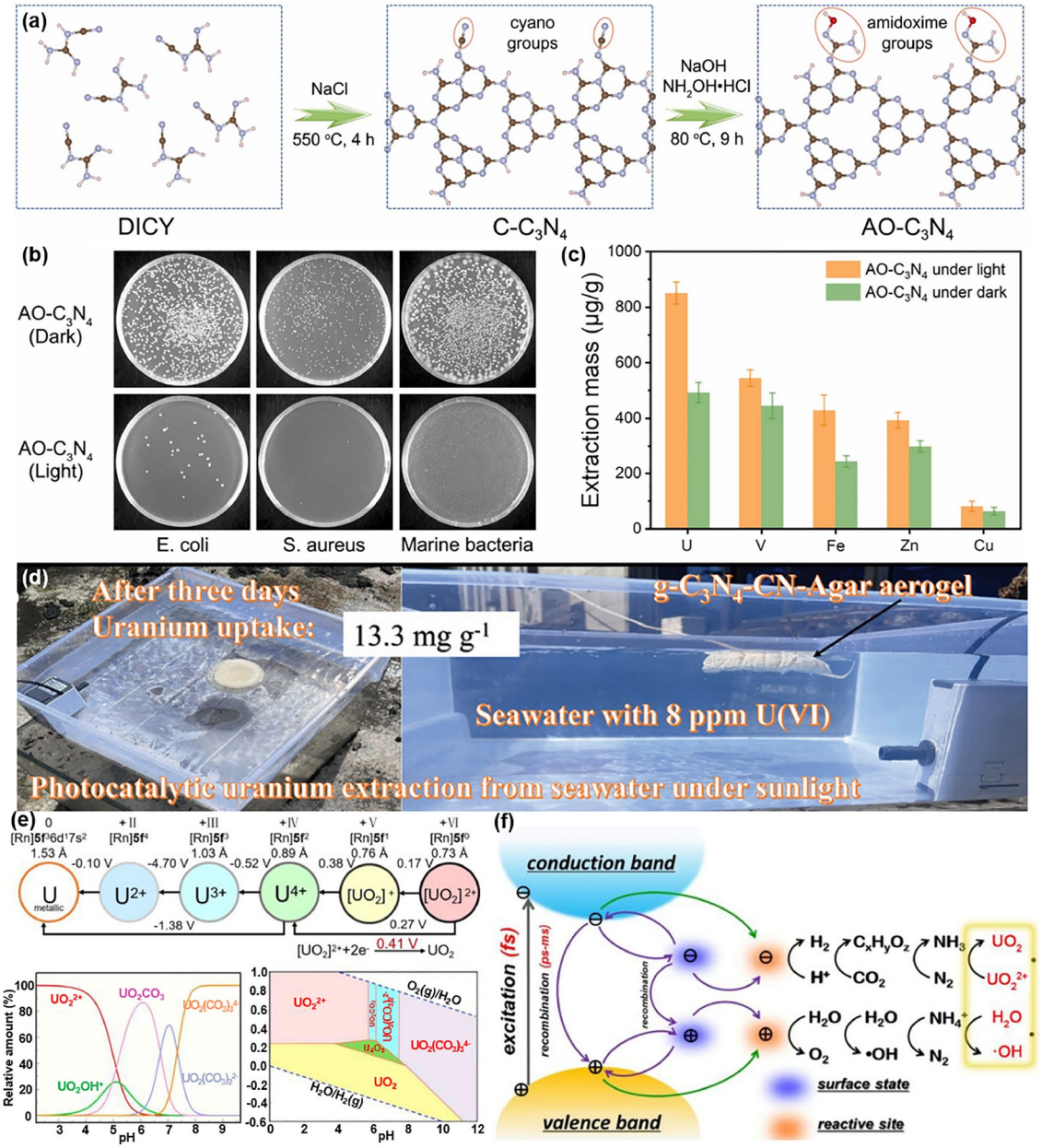

Figure 17 (a) The preparation diagram of AO-C_3N_4. (b) Photographs of anti-biofouling of AO-C_3N_4 and (c) the selectivity of AO-C_3N_4 from natural seawater under dark/light [453]. (d) The solar light-driven photocatalytic uranium extraction from seawater over g-C_3N_4-CN-Agar aerogel [64]. (e) The chemical valence of uranium and the complex forms of uranium under various pH. (f) The photoreduction uranium process [447] (color online).

holes in the valence band [462]. Secondly, the photo-generated electron-hole pairs separate and migrate to different reaction sites. During this process, some electron-hole pairs may be captured and recombined by defects or sites within the catalyst, thereby affecting the efficiency of the subsequent photocatalytic reactions. Finally, the electrons and holes that successfully migrate to the surface of the catalyst will participate in reduction and oxidation reactions, promoting the conversion of chemical substances. Throughout the entire reaction process, various types of reactive oxygen species (ROS) can be generated. Dissolved oxygen in water participates in competitive electron reactions to generate superoxide radicals ($\cdot O_2^-$), while water is oxidized by holes to hydroxyl radicals (·OH). Through a series of catalytic conversion reactions, the entire photocatalytic system mainly produces four stable reactive substances: superoxide radicals, singlet oxygen, hydroxyl radicals, and hydrogen peroxide [463]. These reactive species exhibit strong reactivity and play crucial roles in the corresponding photocatalytic U (VI) reduction reaction.

Uranium exists in four valence states: VI, V, IV and III. IV and VI states are the most important valence states (Figure

17e). Hexavalent uranium (U(VI)) in the form of uranyl ions (UO_2^{2+}), contained in wastewater or seawater, is easily to migrate in the aquatic environment. The U(VI) species are mainly in the form of UO_2^{2+}, UO_2CO_3, and $UO_2(CO_3)_3^{4-}$ at different pH conditions. The photoreduction of uranium aims to convert mobile U(VI) to U(IV) (Figure 17f).

Based on the photocatalytic reaction processes described above and related research on photocatalytic U(VI) reduction, three main mechanisms can be identified for the involvement of photo-generated electrons in U(VI) reduction reaction [447]:

(1) Single electron reduction: the U(VI) captured by functional groups is first photoelectron and reduced to U(V) (Eq. 1). And then, U(V) further obtains electrons and is further reduced to U(IV) (Eq. 2). Meanwhile, U(V) can also undergo disproportionation to generate U(VI) and U(IV) during the entire reaction (Eq. 3).

$$U(VI) + e^- \rightarrow U(V) \quad (1)$$

$$U(VI) + e^- \rightarrow U(IV) \quad (2)$$

$$U(V) \rightarrow U(VI) + U(IV) \quad (3)$$

(2) Double electron reduction: the captured U(VI) directly obtains two photoelectrons and is reduced to U(IV) in one step (Eq. 4).

$$U(VI) + 2e^- \rightarrow U(IV) \quad (4)$$

(3) Double electron reduction involving proton participation in an acidic solution: during the reduction process of U (VI), H^+ directly participates in the reduction of U(VI) due to the high concentration of H^+ in the solution (Eq. 5).

$$UO_2^{2+} + 4H^+ + 2e- \rightarrow U^{4+} + 2H_2O \quad (5)$$

9.3 Progress of g-C_3N_4 for thorium separation

The radioactive nuclide Th(IV) primarily originates from radioactive wastewater generated by nuclear power production and thorium mining, which presents significant challenges in treatment and disposal for the nuclear energy industry and radioactive waste management [464]. Effectively extracting Th(IV) from radioactive wastewater is beneficial for the efficient utilization of thorium resources and environmental conservation [92,465]. g-C_3N_4 is composed of repeating units of tri-s-triazine, containing a high proportion of pyridinic-N, with electronegativity between C and O. This characteristic provides it with abundant lone pair electrons, enabling coordination with metal ions and promoting solvent-interface interactions, thereby achieving efficient adsorption and separation of target radionuclides in complex solutions. Furthermore, the –NH–/–NH_2/=N– functional groups on the surface of g-C_3N_4 can also serve as active sites for metal adsorption, accelerating the adsorption kinetics of metal ions. However, the original g-C_3N_4 as an adsorbent presents some challenges in the field of Th(IV) adsorption. For example, the specific surface area and active sites of g-C_3N_4 are relatively limited, severely limiting the removal efficiency of Th(IV). To address these challenges and achieve efficient adsorption and separation of Th(IV), previous studies have focused on morphology control and functional group modification. These strategies have been proven to be one of the most direct and effective approaches to increasing the specific surface area and reactive sites of g-C_3N_4. Presently, various g-C_3N_4-based materials for efficient adsorption and separation of Th(IV) have been developed using these strategies, and significant research progress has been made.

9.3.1 *Morphology and pore structure regulation*

Regulating the morphology and structure of g-C_3N_4 is considered a promising strategy, which can endow g-C_3N_4 with a higher specific surface area and more active sites. Compared with bulk g-C_3N_4, the higher specific surface area brings more abundant active sites, which facilitates mass transfer and adsorption of reactants, significantly enhancing the adsorption performance for target metal ions. In recent years, relevant studies have reported the use of modified g-C_3N_4 as an adsorbent to separate Th(IV) from radioactive wastewater [466]. For instance, Liao *et al*. [467] prepared g-C_3N_4 nanosheets using the sonochemical thermal oxidation-etching method, which exhibited excellent adsorption capacity for actinide and lanthanide ions (Eu(III), La(III), Nd(III), Th (IV)) from aqueous solutions. The results indicate that the adsorption capacity of g-C_3N_4 nanosheets for Th(IV) was up to 185.6 mg/g at 333 K. Additionally, Huang *et al*. [468] used the sol-gel templating method to prepare mesoporous N-doped carbon (*mpg*-C_3N_4) for highly selective adsorption of Th(IV) (Figure 18a). The *mpg*-C_3N_4 exhibited the best selective extraction of Th(IV) in the presence of interfering cations with extraction capacities of 202.43 mg/g for mpg-$C_3N_{4/r}$ = 1.0 and 61.20 mg/g for g-C_3N_4 (Figure 18b). Th(IV) was almost completely adsorbed and reached to 93.53% (Figure 18c).

9.3.2 *Functional group modification*

The rich coordination sites and functional groups determine that g-C_3N_4-based materials possess high adsorption capacity by forming strong surface complexes [469]. As is well known, amidoxime group is considered a star group with strong chelating properties with metals. Meanwhile, the amidoxime group possesses good chemical stability and controllability, enabling it to maintain efficient removal efficiency in complex environments. For example, Yussuf *et al*. [470] prepared amidoxime-functionalized g-C_3N_4 (g-C_3N_4-AX) photocatalysts using urea as a precursor *via* a hydrothermal method for the removal of Th(IV) from aqueous solutions. Experimental results indicated that the out-

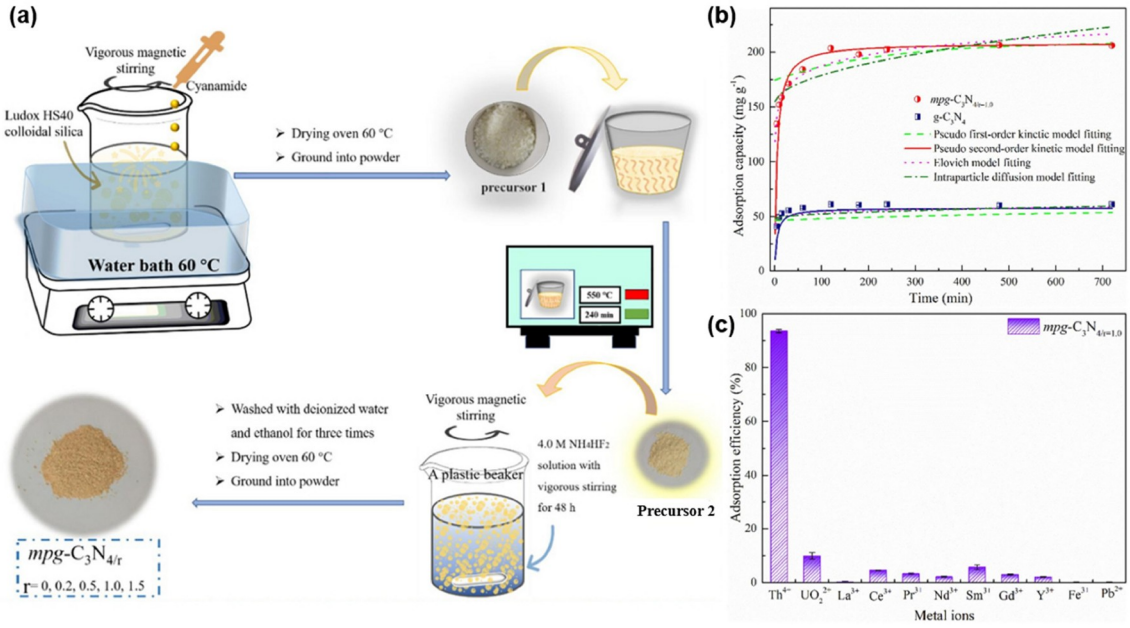

Figure 18 (a) Synthesis route of *mpg*-C_3N_4. (b) Adsorption kinetics for the adsorption of thorium and (c) selectivity of *mpg*-C_3N_4 in monazite leachate [468] (color online).

standing performance of g-C_3N_4-AX was mainly attributed to the introduction of the amidoxime group. The g-C_3N_4-AX exhibited the best selective extraction of Th(IV) in the presence of interfering cations with an extraction capacity reaching 71.09 mg/g. Meanwhile, the above team also successfully prepared a g-C_3N_4/AX electrode modified with amidoxime group for the efficient and selective electro-adsorptive separation of Th(IV). The results indicated that the g-C_3N_4/AX electrode achieved a removal efficiency of 84.46% for Th(IV) at −1.0 V and a high adsorption capacity of 275.74 mg/g. Mechanistic studies revealed that the abundant nitrogen sites and amidoxime groups on g-C_3N_4/AX electrode are highly active sites for efficient Th(IV) adsorption [471]. In addition, g-C_3N_4 had shown remarkable potential in the separation of other radionuclides (Eu(III), La (III), Nd(III)) [467]. It is worth noting that g-C_3N_4 can be further customized according to the characteristics of different radionuclides to achieve efficient and selective extraction of corresponding radionuclides.

9.3.3 Adsorption mechanism of thorium

Currently, g-C_3N_4-based materials are widely used in the research of adsorption and separation of Th(IV) from radioactive wastewater. The adsorption mechanism of Th (IV) by g-C_3N_4-based materials has always been the focus of researchers. The pyridine-like nitrogen in g-C_3N_4, such as –NH_2/–NH–/=N–, provides abundant lone pair electrons, which are considered the main active sites for capturing Th (IV). The pH value, ionic strength, and temperature of the solution can also affect the dissolution behavior and surface adsorption characteristics of Th(IV), thereby affecting adsorption efficiency. Therefore, when studying the adsorption mechanism of Th(IV), it is necessary to consider the impact of environmental factors on adsorption behavior comprehensively. Additionally, the surface properties and structural characteristics of g-C_3N_4 are crucial for the adsorption mechanism of Th(IV). For example, the content, distribution, and chemical properties of surface nitrogen functional groups directly influence the interaction between Th(IV) ions and the adsorbent. By controlling the synthesis methods and surface modifications, the adsorption performance of g-C_3N_4-based materials for Th(IV) can be effectively adjusted to enhance adsorption efficiency and selectivity. In conclusion, a comprehensive understanding of Th(IV) adsorption mechanism by g-C_3N_4 as an adsorbent involves various factors such as environmental conditions, surface properties, and structural characteristics.

9.4 Prospect of g-C_3N_4 for other radionuclide separation

Although g-C_3N_4 has made significant progress in the separation of radioactive U(VI) and Th(IV) as an excellent photocatalyst and adsorbent. However, there are still numerous unresolved challenges in the design of catalysts, understanding of mechanisms, and practical applications. The composition of real seawater and industrial radioactive wastewater is especially complex, containing a large number of high concentrations of competing ions and organic compounds that are far beyond the concentration range in laboratory studies. In this case, it is not accurate to evaluate the application prospects of g-C_3N_4-based materials based on the results obtained under relatively ideal laboratory conditions.

In terms of mechanism research, future research directions should focus on some *in-situ* characterization techniques, such as *in-situ* synchrotron radiation, *in-situ* infrared spectroscopy, and so on. In practical applications, various factors in complex environments such as strong acid, strong alkali, high salt, and strong radiation (mainly γ rays) should be systematically considered to comprehensively evaluate the feasibility of the practical application of g-C_3N_4-based materials.

10 Biomimetic materials for radionuclides separation

10.1 Biomimetic porous materials

Rather than solely relying on traditional chemical processes, bioinspired and biomimetic approaches, mimicking the structure and process of biomolecules and living organisms for enriching U(VI) and some other radionuclides, have emerged as new strategies for radionuclides separation [472]. Biomimetic materials exhibit several advantages for radionuclides separation owing to their distinct characteristics deriving from the natural biological systems. The construction of biomimetic materials is based on the desirable physiological structure and bioconcentration mechanism of biomolecules and living organisms, including high binding affinity, high selective recognization, and high binding site density, which enable biomimetic materials with excellent separation ability to radionuclides [68,145,473]. The ongoing progress in this area has mainly focused on U(VI) separation and can provide highly potential approaches for developing highly efficient materials to combat the challenges linked with radionuclide contamination.

The development of biomimetic materials entails creating nanoparticles or nanostructures with functionalized surface characteristics. Inspired by the mechanisms of biomolecules and living organisms in binding radionuclides, the surfaces can be modified with specific ligands or molecules that have a strong binding ability to target radionuclides to mimick the biological structures. By taking cues from proteins, enzymes, and other biological structures, researchers craft materials that possess improved selectivity and effectiveness in separating radionuclides [144,474–476]. Various techniques, such as protein engineering, self-assembly technique, and template method, are utilized to empower the materials with superior selectivity and efficiency for separating radionuclides [13,477,478]. This section focuses on four crucial classes of strategies for constructing highly efficient materials for radionuclides separation, mainly including the utilization of biomaterials, the construction of biomimetic chelating sites, the construction of biomimetic ion channels and the biomimetic photocatalysis.

10.2 Strategies for biomimetic separation of radionuclides

10.2.1 Biological materials

Super uranyl-binding protein (SUP), which attains femtomolar binding ability (K_d = 7.4 fM) and ultra-high selectivity (> 10,000-fold over other metal ions) to uranyl ion by forming uranium recognization biological structures, has been designed to enable efficient and selective separation of uranyl ions. However, the modest mechanical strength of SUP-based adsorbent limited its application in the practical environment [32]. Wang and his colleagues conducted extensive research on SUP and their derivatives for U(VI) separation. Considering the robust strength and extensibility of spider silk, they engineered protein hydrogel fibers from spidroin-based SUP (SSUP) using biomimetic spinning technology [476]. The fast saturation time of 30 min with an adsorption capacity of 15.91 mg/g was achieved in simulated seawater containing 16 mg/L U(VI). When tested in real seawater, the U(VI) adsorption capacity of SSUP fibers reached 12.33 mg/g over a span of 3.5 days, proving the function of SSUP in U(VI) separation. However, there was no significant synergistic effect on U(VI) adsorption by SSUP fusing with spidroin that lacks specific uranyl ion binding ability. Further investigation revealed that SUP showed high structural similarity with that of spidroin, which were all characterized by α-helices and random coils. Therefore, dual copies of SUP protein (DSUP) were linked and subsequently spun into a protein hydrogel fiber.

Given that DNAzyme can specifically recognize uranyl ions, a DNA-based adsorbent was initially explored for U(VI) separation. A single uranyl-binding DNA strand derived from DNAzyme was cyclized into circular DNA and further transformed into a DNA hydrogel DNA-UEH *via* rolling circle amplification. In test with 8 mg/L U(VI)-spiked simulated seawater at pH = 5.0, the U(VI) adsorption capacity achieved 13.71 mg/g within 24 min. Subsequent trials in actual seawater over 6 days demonstrated an adsorption capacity of 6.06 mg/g. Mechanistic analysis showed that a five-coordinated nanostructured pocket was formed by the coordination of five oxygen atoms from phosphate and carbonyl groups on DNA-UEH with uranyl ions, which empowered this DNA hydrogel with binding uranyl binding selectively and affinity (Figure 19a, b) [479].

Furthermore, an antimicrobial peptide omiganan, identified through a database screening of antimicrobial peptides, not only displayed broad-spectrum antimicrobial activity but also exhibited a strong binding affinity for uranyl ions [31]. Therefore, dual copies of SUP protein (DSUP) were linked and subsequently spun into a protein hydrogel fiber. This DSUP fiber, exhibiting a loofah-like structure due to the cross-linked thin nanofibers, demonstrated substantial mechanical strength. Benefit to the synergistic effect of dual

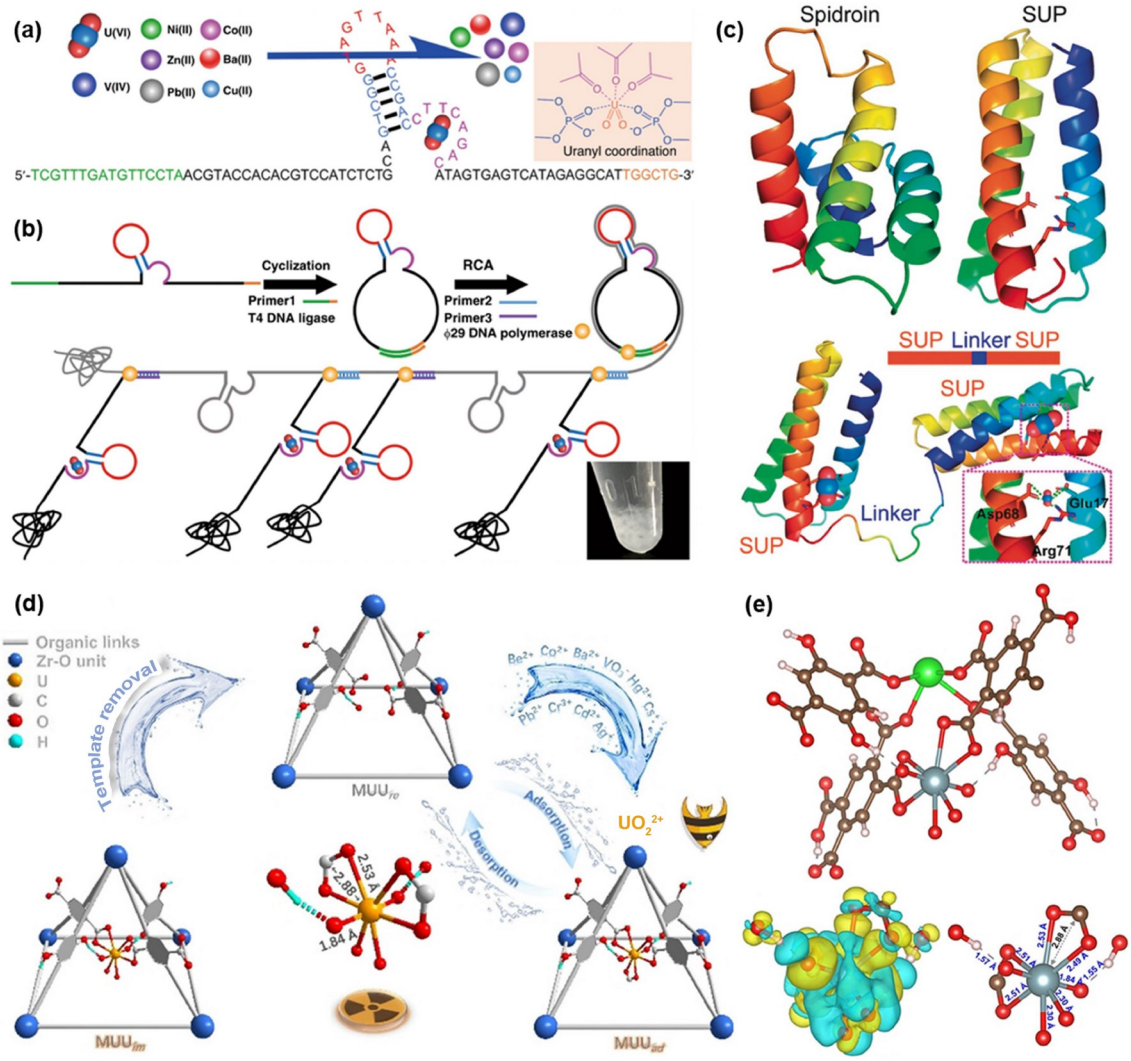

Figure 19 (a) Biological materials with nano coordination structures and materials with biomimetic nano coordination sites for separation of uranium. (b) Schematic illustration for the fabrication of DNA-hydrogel DNA-UEH and the nanopocket formed in DNA-UEH for separation of uranyl ion [479]. (c) 3D structure and uranyl adsorption mechanism of protein DSUP [474]. (d) *In situ* synthesis of uranyl-imprinted nanocage for uranium separation and (e) DFT calculation of coordination mechanism [145] (color online).

copies of SUPs, DSUP exhibited superior performance in U(VI) adsorption coupled with a saturation adsorption capacity of 17.45 mg/g within a 3-day period in real seawater (Figure 19c) [474]. The polymeric peptide hydrogel PPH-OP was fabricated using glutaraldehyde crosslinking to generate abundant nanoscale pores on the wall of dry hydrogel to improve U(VI) adsorption capacity. Adsorption experiments indicated that PPH-OP achieved excellent U(VI) adsorption, capturing 139.47 mg/g in 16 mg/L U(VI) simulated seawater within 70 min and 7.12 mg/g in real seawater over 3 weeks. Mechanistic studies further disclosed the formation of a nanostructure cage, wherein each U(VI) atom was coordinated by two oxygen atoms from the carbonyl groups of amino acid residues Arg11 and Lys12 with bond lengths of 2.45 Å and 2.27 Å, respectively, resulting in high U(VI) binding selectivity. The design and application of biological materials for U(VI) separation are all based on the assembly of uranyl-binding nanostructures by the biomolecules themselves, which endowed the biological materials with the ability to selectively and tightly bind to U(VI) ions.

10.2.2 Biomimetic nano-chelating sites

Since the identification of bio-chelation in uranyl-binding biomaterials, researchers have been inspired to create nanostructured chelating sites into porous materials. In 2018, Sun *et al*. [473] proposed the innovative use of a nano-trap strategy for U(VI) separation. To validate this hypothesis, the artificial chelating models were constructed by integrating amidoxime and amino groups into porous organic polymers (POPs). The designed POP-based materials all achieved 90% of their equilibrium capacity within 1 h. Notably, POP-*o*NH_2-AO exhibited high adsorption capacity of 530 mg/g

for U(VI) in 7.56 mg/L uranium solution and 4.36 mg/g in real seawater during 56 days of seawater immersion. Single crystal structure analysis and DFT calculation revealed that hydrogen bonding interaction worked as a sub-interaction aided by amino groups, significantly enhancing the coordination of POP-*o*NH_2-AO with uranyl ions. This phenomenon bore a resemblance to the chelation interaction observed in well-folded proteins, highlighting the importance of second-sphere interaction in such a coordination process. Except for amino groups that have been found to form mimic bionic chelation, carboxyl, phosphate and hydroxyl groups, which widely existed in biological systems, have also been found to play a significant role in the binding of U(VI) by biomolecules and living organisms. Motivated by the high specificity and affinity of SUP protein for uranyl ions, the construction of such highly binding affinity nanopockets for uranyl ions can also be realized by introducing uranyl ion template into MOFs and a higher uranyl binding affinity of 0.3 pM to uranyl ions was achieved (Figure 19d, e) [145]. Compared with natural biological materials containing nanostructures for separating radionuclides, biomimetic chemical chelators exhibit higher stability and lower fabrication costs, which can greatly improve their application potential in complicated natural environments.

10.2.3 Biomimetic nano-ionic channels

To realize efficient transportation of nutrients and metabolic waste, organisms have evolved numerous transportation channels within the body. The construction of biomimetic nano-ionic channels in membranes presents a highly potential strategy for efficient separation of radionuclides. The hierarchical networks in the blood vessels of organisms make it possible to transport mass efficiently while requiring minimal energy. This proof-of-concept prototype provided the synthetic inspiration of an artificial bionic membrane; a hierarchical self-supporting membrane AO-PIM-1 was fabricated *via* the traditional non-solvent-induced phase separation method [69]. The pore diameters of the major transport channel run through in AO-PIM-1 were around 20 μm, which was sufficient to allow the readily move of uranyl ions, while the smaller pores of 300–500 nm on the wall provided uranyl ions with more available binding sites. The adsorption capacity of AO-PIM-1 was 345.94 mg/g in 32 mg/L U-spiked water. Intriguingly, a plateau was observed during the adsorption processing where U(VI) began diffusing into the biomimetic branching nanochannels. After adsorption in seawater for 28 days, AO-PIM-1 exhibited an adsorption capacity of 9.03 mg/g for U(VI). Indisputably, the size of the crown ether significantly influences the coordination of nuclides within the ion channels in this strategy. To clarify this, Li *et al*. [480] embedded modular tunable crown ether units into Zr-based MOF and designated them ZJU-X100 and ZJU-X102. Both ZJU-X100 and ZJU-X102 exhibited rapid response in wastewater containing Sr(II) or Cs(I) ions, achieving adsorption equilibrium within 1 min (Figure 20a). However, the mechanistic analysis demonstrated that ZJU-X102 containing a larger pore of 24-crown-8-ether underwent conformational change while coordinated with Cs(I) ions, resulting in a high energy barrier which paradoxically decreased its selectivity towards the target ions (Figure 20b). Furthermore, mimicking the fast and selective ion transfer across biological transmembrane channels is also an effective approach. Yu *et al*. [481] engineered a nano-transport channel modified with 4-sulfocalix[4]arene on a GO-substrate membrane SCA-GO. This modification significantly improved the separation coefficients for K^+/Mn^{2+} on SCA-GO. For example, the separation ratio K^+/UO_2^{2+} for SCA-GO increased from 12.7 for pristine GO membrane to 263, which was attributed to the specific binding between functional molecule 4-sulfocalix[4]arene and radionuclides.

10.2.4 Biomimetic photocatalytic materials

Drawing inspiration from photosynthesis, Dong *et al*. [454] designed a novel hollow nanosphere (MTCA), which consisted of MnO_x, TiO_2, CdS, and Au materials, using a hard template and hydrothermal method (Figure 20c). The Z-scheme heterojunction of TiO_2@CdS coupled with spatially separated cocatalyst Au NPs and MnO_x effectively suppressed the charge recombination process and thereby structured a biomimetic photocatalytic system. Importantly, the removal rate of U(VI) by MTCA reached 91.83% in natural uranium mine wastewater without adding any sacrificial agent under natural sunlight irradiation at the solid-to-liquid ratio of 0.75 g/L. Moreover, the U(VI) removal rate of MTCA maintained 94.8% of its original performance after five reuse cycles, demonstrating the considerable application potential of MTCA. The electronic transfer paths formed through the electron donor (D) and acceptor (A) in photosystem II (PSII), which holds different electron affinities to minimize the electron-hole recombination and, therefore, promote the separation efficiency. Inspired by this, Yu *et al*. [482] chose plastoquinone (PQ) with both electron deficiency and redox activity to construct PSII-like charge transport chains for U(VI) separation. Utilizing conjugated microporous polymers (CMPs) as support, three metal-free biomimetic donor-acceptor photocatalysts were fabricated *via* Sonogashira-Hagihara coupling polymerization. The generated catalyst ECUT-TQ exhibited a narrow band gap of 1.7 eV and realized a high U(VI) removal rate of 97.4%. In addition to developing biomimetic photocatalytic systems, it has been demonstrated that the integration of bacteria with inorganic photocatalysts can also act as an effective system for boosting U(VI) removal ability. Wang *et al*. [68] developed a hybrid biotic-abiotic catalytic system (UUS-1/CdS) that could effectively facilitate both selective adsorption and

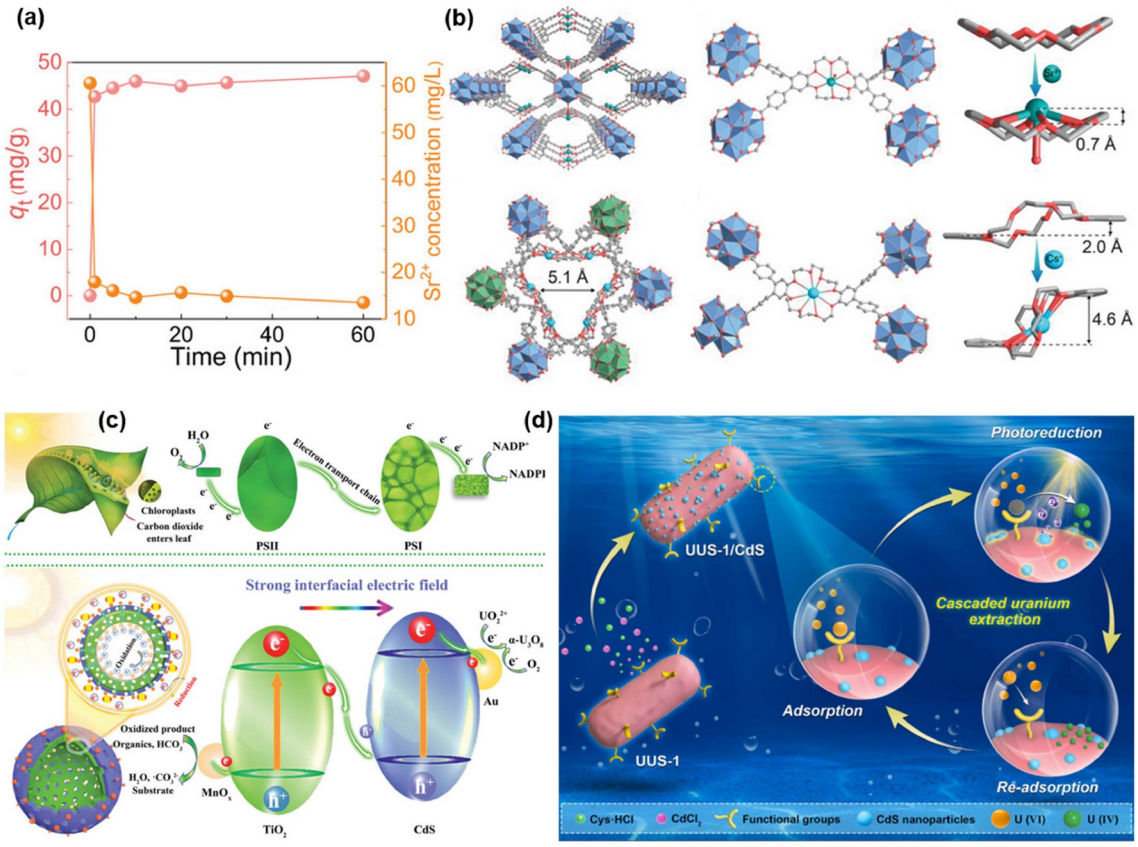

Figure 20 (a) Adsorption kinetics of ZJU-X100 toward Sr^{2+} and (b) extraction mechanisms of ZJU-X100 and ZJU-X102 [480]. (c) Photosynthesis inspired biomimetic photocatalysis system constructed by MnOx@TiO_2@CdS@Au (MTCA) for separation of U(VI) [454]. (d) Schematic illustration of photosensitized biohybrid system UUS-1/CdS for U(VI) extraction from seawater [68] (color online).

photoreduction of U(VI) (Figure 20d). This system enhanced U(VI) separation efficiency by 81.29% following the introduction of CdS nanoparticles. This study indicated that the collaborative application of biological adsorption and reduction enrichment would be a promising strategy for improving the separation selectivity and capacity of U(VI).

The biomolecules and living organisms realize efficient enrichment of radionuclides mainly by the specific nanostructures for binding radionuclides or the catalysis of radionuclides *via* efficiently providing electrons. Accordingly, the design of biomimetic materials for radionuclides separation incorporated four strategies derived from these two fundamental mechanisms. Firstly, the biological molecules that contain nanostructures with strong radionuclide-binding ability were directly employed in the fabrication of materials for separating radionuclides. Secondly, several previous studies tended to emphasize *in-situ* introduction and spatial regulation of functional groups derived from biomolecules on materials to construct biomimetic nanostructured binding sites. Thirdly, inspired by the nanochannels in organisms for transportation, biomimetic nano-ionic channels were built to enhance the speed and affinity of radionuclides separation. Finally, porous materials were designed by mimicking the photosynthesis process, thereby realizing enhanced radionuclides separation through photocatalysis. As a result, the biomimetic separation outperformed the traditional chemical separation approach in the categories of separation selectivity, separation capacity and separation speed, which empowered them with considerable application potential.

Despite the significant application potential of biomimetic porous materials in the separation of radionuclides, these materials still face several technical challenges. Firstly, based on the fundamental mechanisms between biomimetic materials and radionuclides, the highly selective separation of radionuclides by biomimetic materials greatly depends on the precisely pre-organized nanostructures for coordination of radionuclides, which is difficult to reproduce well in porous materials by using chemical synthesis methods. Thus, the method for easily constructing nanostructures to bind radionuclides and the approach for large-scale fabrication of biomimetic materials are still lacking. Secondly, the biomimetic materials have exhibited outstanding performance in the extraction of radionuclides, particularly U(VI), Sr(II), and Cs(I), but reports on some other radionuclides are still limited, which are primarily attributed to the poorly under-

stood of interactions between biomolecules and living organisms with radionuclides. The uncovering of more interactions between biomolecules and living organisms with other radionuclides can provide more theoretical instruction for designing biomimetic materials targeted at these radionuclides. Thirdly, several biomolecules and living organisms in nature exhibit enrichment ability to diverse radionuclides, while currently available studies only focused on the selective separation of individual radionuclides. In fact, multiple radionuclides always existed simultaneously. The fabrication of biomimetic materials from biomolecules or living organisms that target diverse radionuclides can meet the need to treat various radionuclide pollutions simultaneously.

In summary, attributing to the excellent ability of biomolecules and living organisms to enrich radionuclides, biomimetic materials have been synthesized for radionuclides separation and promising separation performances have been realized, proving the feasible of biomimetic strategies in treating radionuclides. However, despite these successful applications, the biomimetic strategies need to be further improved to fulfill the practical needs, including the large-scale and economical fabrication method as well as the design of biomimetic materials with broader adsorption ability. With the goal of "from nature, beyond nature", the utilization of biomimetic materials would be a highly potential approach for practically separating radionuclides.

11 Carbon dots and their composite materials for radionuclides separation

11.1 Brief introduction of CDs

Carbon dots (CDs) or carbon quantum dots (CQDs) are a new class of carbon materials and they were first found by Xu *et al*. [483] during the purification of carbon nanotubes. They have high photoluminescence, and excellent biocompatibility and most of them are water soluble with a diameter smaller than 10 nm. These appealing characters have gained great attention in various research areas, such as bioimaging, drug delivery, catalysis, sensors, environmental remediation and so on [484,485]. Commonly, CDs are composed of carbon with various functional groups such as carbonyl, hydroxyl, and amino groups, which depend on the raw materials and the further functionalization process [486]. They are synthesized *via* top-down and bottom-up methods with a wide array of raw materials, such as carbon precursor (graphene, active carbon, carbon nanotubes *etc*.), nitrogen precursor (urea, p-phenylenediamine, ethylenediamine *etc*.), sulfur precursor (polythiophene, thioacetamide *etc*.), phosphorus precursor (phosphoric acid, phosphoryl chloride), bio-molecules (proteins, amino acids, sugars), polymers and so on [484]. The fluorescent or other properties of CDs are tuned with the raw materials and the synthesis methods, and it is convenient to design diverse CDs for various application areas.

While CDs also have some drawbacks in specific fields, it is an effective approach to fabricate CD-based composite materials to overcome the limitations of CDs. Besides, by choosing proper substrate materials, the fabrication of composite materials can also enhance the fluorescent, biocompatible, or photocatalytic properties, strengthen the mechanical properties, expand the application areas and so on. Various substrates can be composed with CDs through different methods, such as polymers, SiO_2, MOFs, C_3N_4, TiO_2, and metal nanoparticles to achieve better application properties.

11.2 Detection of uranium with CDs

The innate fluorescent property of CDs makes them different from other carbon materials [487]. CDs also possess tunable optical properties, low toxicity and high chemical stability, which are superior to the conventional semiconductor quantum dots and have been widely used in the detection of metal ions. Wang *et al*. [488] prepared CDs with a novel and convenient microplasma method in minutes and first introduced CDs for the detection of U(VI). The combination of CDs and U(VI) could quench the fluorescence of CDs, thus realizing the low limitation detection of U(VI). The detection mechanism is aggregation-caused quenching (ACQ) with the formation of the non-fluorescent complex [489]. The researchers often functionalized groups on CDs to combine with uranyl ions. Zhang *et al*. [490] employed hydroxypyridinone (HOPO), which was a chelating ligand with a strong affinity for U(VI), to prepare HOPO-CQDs. The fluorescence signal of HOPO-CQDs was quenched by uranyl ions in 1 min with a detection limit of 6.53 μg/L. HOPO-CQDs particles aggregated together after being combined with uranyl ions because the size was increased from 2.3 nm to 68.1 nm. Shilpa *et al*. [491] functionalized pamoic acid (PA) onto N-doped graphene quantum dots (N-GQDs), which had a high binding affinity towards U(VI) in aqueous medium with a detection limit of 2.009 μM. Gong *et al*. [492] anchored a layer of Ag^+ on the surface of CDs/SiO_2 material and the photoinduced electron transfer (PET) between CDs and uranyl ions made them good fluorescent probes with excellent selectivity and detected limit of 37 nM (Figure 21a). Wang's group [493] synthesized rhodamine functionalized CDs (o-CDs-Rho) for the ratiometric detection of uranyl ion with a detection limit of 53 nM. The mechanism was proposed to be aggregation-enhanced fluorescence resonance energy transfer because the FRET efficiency increased from 16.2% to 77.2% after CDs were aggregated with uranyl ions (Figure 21b). In addition to detecting uranyl ions in solution, Wu's group [494] prepared a CD-based solid-state sensor by printing CDs on nanofiber films and

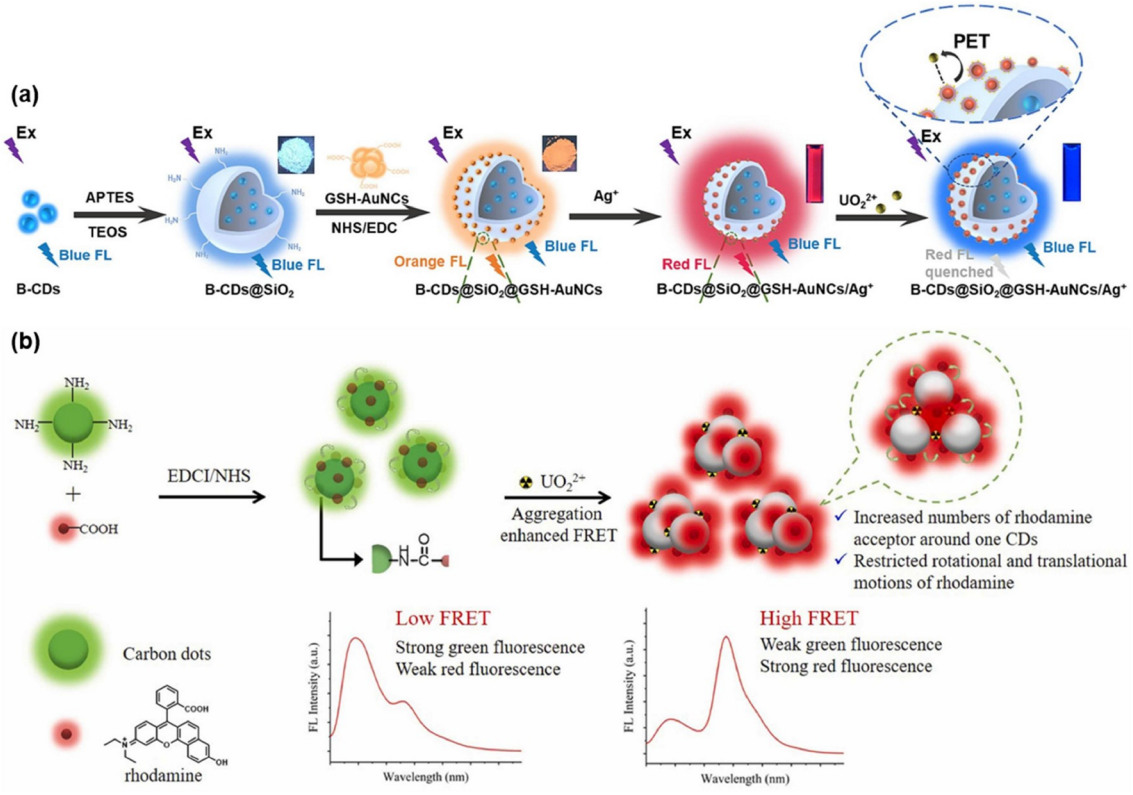

Figure 21 (a) The preparation process and photoinduced electron transfer (PET) between CDs and uranyl ions [492]. (b) The aggregation enhanced FRET for fluorescence detection of uranyl ions [493] (color online).

doping them into hydrogels. The two solid sensors could also detect uranyl ions with high selectivity, low cost, easy production and storage facilitation.

11.3 Adsorption of uranium with CDs

Most CDs are water soluble and small in size, which makes them hard to separate and recycle during the adsorption process. It is a good way to synthesize CD-based solid materials to cover the shortages. The small size of CDs endows the surface with abundant edge amine, carboxyl, and hydroxyl functional groups and so on. These groups can be designed and tailored easily by choosing proper raw materials during the synthetic process to accomplish different demands. They can be easily combined with other solid materials to prepare CDs composite materials.

Wang *et al*. [495] synthesized CD-based mesoporous silica (CDs/SBA) composite materials with the microplasma method and first applied CDs for the adsorption as well as detection of U(VI). They found that the introduction of CDs on silica not only enhanced the adsorption property of U(VI), but also possessed the fluorescent detection property of U (VI). They integrated the fluorescence and adsorption properties of CDs together and creatively applied the fluorescence signal change of CDs/SBA to determine the degree of adsorption saturation for U(VI). Interestingly, the selectivity of targeted metal ions on CD-based materials can be predicted by evaluating the fluorescence selectivity of the original CDs for metal ions.

Then, researchers employed the adsorption properties of CDs and decorated them onto magnetic materials [61,496,497], layered double hydroxides (LDHs) [498], MOFs [499,500], GO [501] and other substrates for the adsorption of U(VI). They found that the small size of CDs made them easy to load on the surface or between the layers of solid materials. The functional groups of CDs are convenient for grafting other targeted molecules, which could enhance the adsorption property for U(VI). Zhou *et al*. [501] composited CDs onto graphene aerogel with the one-step hydrothermal method and the experiments verified that the loading of CDs and graphene could bring target groups onto the surface of 3D graphene to enhance the adsorption property but also transform the zeta potential of rGO/ZIF-67 from positive to negative, which could improve the electrostatic interaction between adsorbents and radionuclides and was a benefit for the adsorption process.

11.4 Photocatalytic removal of uranium with CDs

Converting soluble U(VI) to insoluble U(IV) or producing other solid products with a photocatalytic method can realize the immobilization of U(VI). This promising strategy has

gradually gained widespread attention and researchers are devoted to finding new photocatalysts with high photocatalytic properties. CDs are a new kind of photocatalysts, and they have a small size effect and high quantum yield, which are beneficial in producing photogenerated electrons. Besides, the surface groups of CDs can be altered, morphed and controlled precisely to improve their photocatalytic activities, which also make them easy to compose with other semiconductor materials to obtain suitable band positions, thereby enhancing the photocatalytic efficiency. After being coupled with other materials, it can extend the adsorption spectrum range and form heterogeneous structures to promote the separation of electrons and holes, increasing the light energy utilization rate. Moreover, CDs possess high thermal and chemical stability, allowing them to be reused multiple times, and they have superior sustainability and good biocompatibility to endow CDs with an environmentally friendly character.

Various metal-free photocatalysts based on CDs have been designed for the photoreduction of U(VI). Dai *et al*. [502] fabricated CD-modified porous g-C_3N_4 (CNCD) for the photoreduction of U(VI). They found that the introduction of CDs could separate photoinduced electron-hole pairs effectively, enhance the visible light absorption capacity and narrow the band gap, reaching a U(VI) removal rate higher than 95%. The photoinduced e^- and $\cdot O_2^-$ could reduce U(VI) to U(IV) and finally convert to metastudtite ($(UO_2)O_2\cdot 2H_2O$) as products. Liu *et al*. [503] introduced CDs to g-C_3N_4 *via* thermal polymerization of melamine and CDs to prepare CDs-C_3N_4 with different loading amounts of CDs. They found that CDs showed obvious up-conversion photoluminescence behavior and made the utilization of light more effective. A weaker PL peak of CDs-C_3N_4 implied the less likely recombination of electrons and holes, and the photocatalytic activity was increased. The photocatalytic reduction of U(VI) by CDs-C_3N_4 was 2.67 times of the pure g-C_3N_4. Due to the high chemical stability of CDs as well as g-C_3N_4, the sample can be used 7 times with a slight decrease in removal rate. The mechanism study revealed that under the irradiation of visible light, the electrons on VB of g-C_3N_4 were excited to CB and transferred to CDs and then reduced the dissolved oxygen to generate $\cdot O_2^-$ and H_2O_2. These species reduced U(VI) to U(IV) and then formed UO_2 and 64% of uranyl ions were reduced and the possible mechanism was listed as Eqs. 6−11.

$$h\nu + \text{CD-}C_3N_4 \rightarrow \text{g-}C_3N_4(e^-) + \text{CDs}(h^+) \quad (6)$$
$$O_2 + e^- \rightarrow \cdot O_2^- \quad (7)$$
$$H_2O + h^+ \rightarrow \cdot OH + H^+ \quad (8)$$
$$O_2 + 2e^- + 2H^+ \rightarrow H_2O_2 \quad (9)$$
$$UO_2{+}\ 2 + 2e^-/2\cdot O_2^-/H_2O_2 \rightarrow UO_2(s) \quad (10)$$
$$CH_3OH + \cdot OH + h^+ \rightarrow CO_2 + H_2O \quad (11)$$

Different from the reduction process, Wang's group [411] designed a new strategy to solidify uranyl ions with a photocatalytic method under air atmosphere. They found that uranyl ions themselves could be photoinduced and reacted with organic materials to form H_2O_2 without any additional photocatalysts [62]. The photogenerated H_2O_2 under air then reacted with uranyl ions to form uranium peroxide solid products, thus realizing the removal of U(VI) efficiently. According to this reaction route (Figure 22), they modified different CDs onto g-C_3N_4 and discovered that the existing CDs were beneficial for increasing the photocurrent density and narrowing down the band gap [504]. The selected SerCDs/CN owned a much-improved removal performance and the removal capacity was as high as 1,690 mg/g. The products were characterized to be $(UO_2)O_2\cdot 2H_2O$, which was different from the photo-reduced process and the possible mechanism was listed as Eqs. 12−18. They also decorated CDs onto polyurethane (CDs/PU) and applied it for the photo-removal of U(VI) under air atmosphere [63]. The U (VI) removal rate of CDs/PU was higher than 97%. The sponge-like PU made the material easy to separate and the removal rate remained higher than 95% after 5 cycles, displaying good reusability. The U(VI) product was also assigned as metastudtite, which was formed by the reaction of uranyl ions and photogenerated H_2O_2 according to the mechanism study.

$$h\nu + \text{g-}C_3N_4 \rightarrow h^+ + e^- \quad (12)$$
$$O_2 + 2H^+ + 2e^- \rightarrow H_2O_2 \quad (13)$$
$$O_2 + e^- \rightarrow \cdot O_2^- \quad (14)$$
$$\cdot O_2^- + e^- + 2H^+ \rightarrow H_2O_2 \quad (15)$$
$$\cdot O_2^- + H_2O_2 \rightarrow \cdot OH + OH^- + O_2 \quad (16)$$
$$CH_3OH + \cdot OH/\cdot O_2^- \rightarrow CO_2 + H_2O \quad (17)$$
$$UO_2^{2+} + H_2O_2 + 2H_2O \rightarrow UO_2(O_2)\cdot 2H_2O + 2H^+ \quad (18)$$

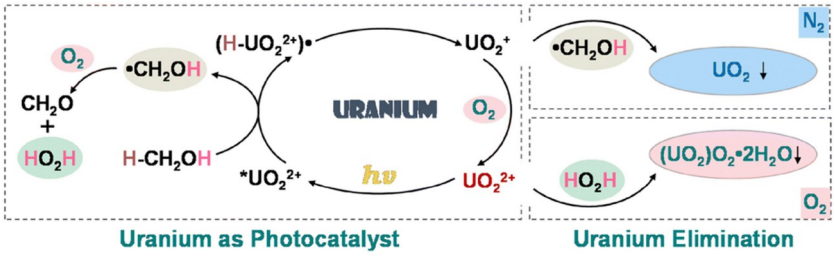

Figure 22 Illustration of the whole reaction mechanism with methanol as the sacrificial reagent under N_2 and air [62] (color online).

11.5 Other radionuclides

Various strategies and materials have been developed for the efficient capture of radioiodine from aqueous solutions. Most CDs are hydrophilic and are commonly used for iodine detection, which has high performance and low detection limits. Zheng *et al*. [505] constructed a hydrophobic surface by decorating hydrophobic CDs onto natural cotton fibers (n-CF) because a hydrophobic interface of adsorbent is required and plays a very important role in the physical adsorption of radioiodine from water. They found that the adsorption capacity of I_2 on n-CF@CDs was 6.8 times higher than that of n-CF. The adsorbed I_2 could be desorbed easily, indicating the good reusability of n-CF@CDs as well as the restoration of I_2.

$^{99}TcO_4^-$ is a radioactive anion formed by the radioactive nuclide ^{99}Tc. ^{99}Tc is a long-lived radionuclide that is water soluble and migrates in water rapidly, posing serious environmental hazards. It is necessary to develop a technique for the detection of $^{99}TcO_4^-$ that is discharged into water. Choi and Lee [506] functionalized quaternary ammonium functional groups onto dual-emission CDs to synthesize cationic CDs (C-CDs). C-CDs exhibited dual emission wavelength characteristics, with emission peaks at 450 and 540 nm. The electrostatic interaction between C-CDs and ReO_4^- could reduce the fluorescence signal and change the color of C-CDs from cyan to blue excited at 350 nm, which was attributed to the photoinduced electron transfer mechanism. The detection limits were calculated to be 87 and 208 μM at the excitation wavelengths of 254 and 350 nm, respectively. This work developed a kind of CD for the quantitative determination of $^{99}TcO_4^-$ while visually verifying the radioactive anion.

Since the first discovery in 2004, CDs have aroused sustained attention in various fields. The construction of CDs mainly involves non-metallic elements, which attach to good biocompatibility and environmentally friendly features. The surface is rich in various groups, which is conducive to further surface modification and functionalization. These characters endow CDs with excellent optical properties, such as tunable fluorescence emission characters, wide adsorption spectrum, and high efficiency to photo-generate electrons and holes. They are also easy to couple with other materials to overcome the shortages of CDs and create synergies to obtain a better performance. CDs have offered wide opportunities for efficient detection, adsorption and photo-elimination of radionuclides from water. Although the majority of these materials have made significant achievements, this attractive field is just in its early stage and many fundamental gaps and challenges still remain the scope of research. There are generally trace amounts of radionuclides in water. Enhancing the detection limit and selectivity with high sensitivity is of great significance for further application. For the adsorption and photocatalytic removal of U(VI), it is necessary to optimize the removal efficiency in complex environments at the commercial level. Therefore, there is still a

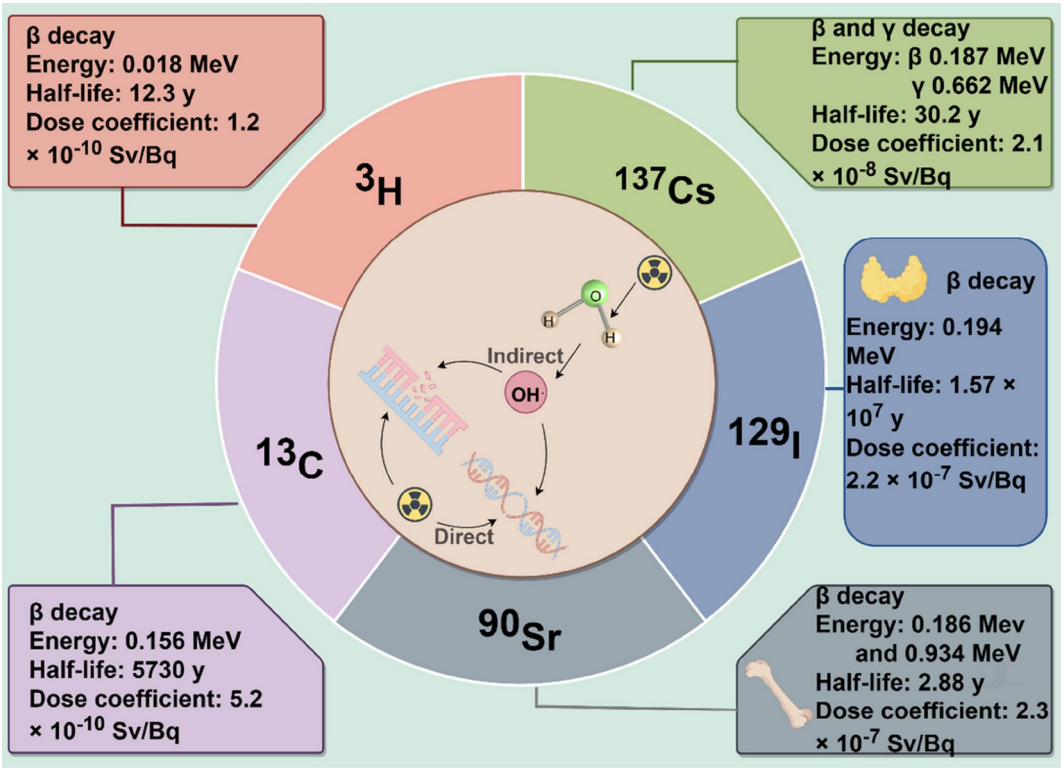

Figure 23 Radiological properties of five radionuclides and their mechanisms of cell damage (color online).

long way to go before developing the practical application of CDs for the treatment of radionuclides.

12 Toxicity of radionuclides

The radionuclides of particular concern in nuclear facility releases include ^{3}H (tritium), ^{14}C, ^{90}Sr, ^{129}I, and ^{137}Cs, with different half-lives, radiation types, and effective radiation doses (Figure 23). The toxicity of radionuclides consists of both chemical toxicity and radiation toxicity. The dose coefficient (DC) is utilized to convert the radiation dose from ingested radionuclides into an "effective dose", which is the primary quantity in the risk assessment system of the International Commission on Radiological Protection (ICRP) [507]. Radioactive isotopes generate α and/or β radiation through α and/or β decay processes. The resulting nuclei from decay are often in high-energy states and undergo transitions to lower energy levels, emitting γ photons as γ radiation or γ rays. Ionizing radiation impacts cells through diverse cellular and molecular mechanisms, exerting biological effects (Figure 24). Among these effects, DNA damage is a significant outcome that can arise from direct or indirect interactions between radiation and DNA molecules (Figure 23) [508,509]. The process of methionine (MET) conversion to S-adenosylmethionine (SAM) can be directly disrupted by radiation, leading to insufficient production of methyl groups (CH_3) required for DNA methylation replication [510]. Meanwhile, radiation can interact with other molecules (primarily water), generating hydroxyl radicals and inducing oxidative stress, indirectly contributing to DNA damage [511].

12.1 Tritium

Tritium (^{3}H), releasing weak β radiation, with a maximum energy of only 0.0186 MeV, and a half-life of 12.3 years, can mobilize quickly in the environment [512,513]. It is one of the most abundant radionuclides in the liquid radioactive effluents of nuclear power plants. The chemical form of compounds containing ^{3}H can result in different biological half-lives. The biological half-life of ^{3}H can be as long as 14 days. However, when ^{3}H is released from nuclear power plants, it is mostly in the form of water (HTO), and its biological half-life is approximately 10 days, which allows it to be rapidly eliminated from the organism [514]. This indicates that continuous ingestion and binding with biomolecules can still pose significant risks even when the radionuclide has low energy. Li *et al*. [515] reported that HTO can impact zebrafish physiology and behaviors by influencing physiological processes and intracellular signaling pathways. Arcanjo *et al*. [516] found that 1.22×10^{5} Bq/L

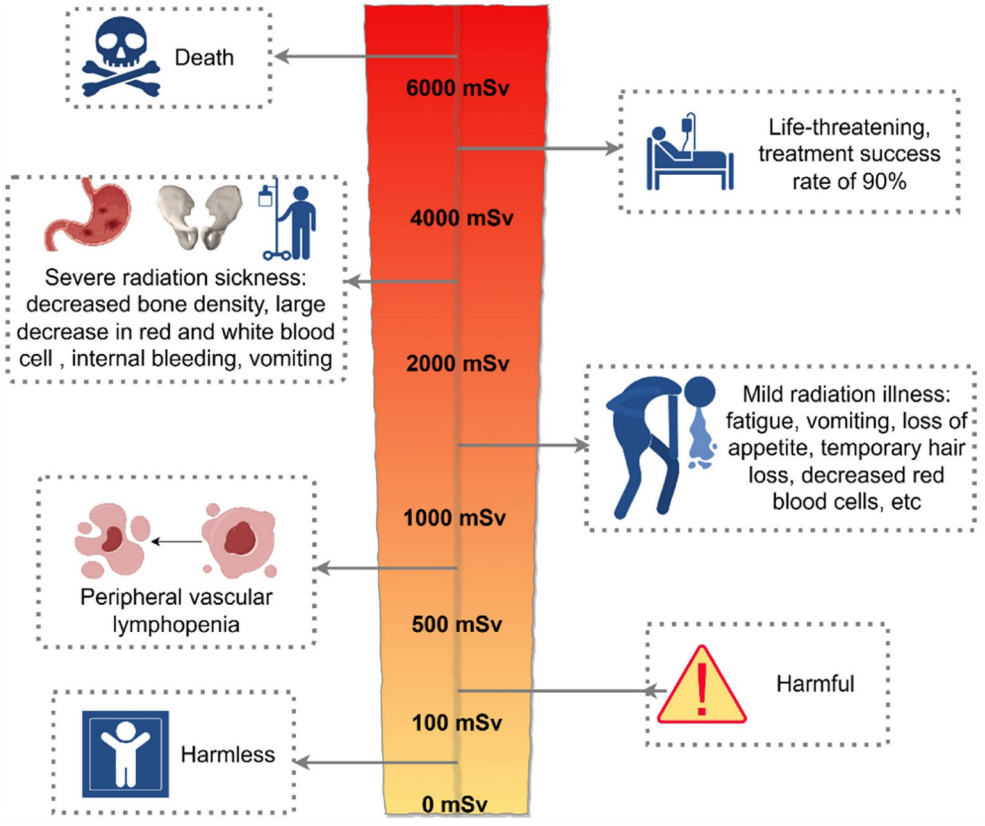

Figure 24 Toxicity to the human body from a single dose of different radiation doses (color online).

HTO can cause dysregulation of proteins involved in defense responses, muscular integrity and contraction, and possible vision alterations for zebrafish autonomous larvae aged 7 and 10 dpf. However, current health risk assessments primarily focused on the accumulation of ^{3}H in individual aquatic organisms, rather than the migration and risks of ^{3}H in the food chain, disregarding this well-known exposure pathway where tritium is internalized and sequestered in organic matter irreversibly, the risk of ^{3}H to humans was probably underestimated [517–522]. A certain proportion of ^{3}H absorbed by animal and plant tissues is incorporated into organic compounds such as lipids, proteins, nucleic acids, and collagen types (organically bound tritium, OBT), where it is chemically bound to carbon atoms, effectively fixed until the compounds begin to undergo metabolism, at which point it becomes exchangeable and decays, while ^{3}H atoms fixed to oxygen, sulfur, nitrogen, or phosphorus atoms can readily exchange with hydrogen in water [523]. OBT is produced through the photosynthesis of plants and the metabolic processes of animals and can be bioaccumulated in contrast to HTO [524]. OBT has a long lifetime (more than 40 days) in the human body. In mammalian organisms, OBT can be partially degraded into HTO and incorporated into the DNA of dividing cells, then subsequently irradiate the cell nucleus through local electron emissions, which is the most hazardous type of radiation, as the entire energy of the radiation is released within the genes; meanwhile, ^{3}H decaying to ^{3}He also disrupts the structure of DNA [525]. The form of ^{3}H affects not only its bioaccumulation but also its toxicity. It was reported that mice exposed to tritiated non-essential amino acids (TAA) ended up with a decrease in red blood cells (RBC) and iron deprivation, while those exposed to HTO did not occur [526].

12.2 Carbon-14

Carbon-14 (^{14}C) is one of the main radioactive effluents released into the environment by the nuclear fuel cycle, such as methane, ethane, and CO_2 [527]. Because of its relatively long half-life (5,730 years), its mobility in the environment and enrichment through the food chain, ^{14}C may pose a long-term potential exposure risk. Carbon is the most basic element of life. Therefore, ^{14}C is likely to participate in the entire process of biological life metabolism, resulting in a potential impact. It was reported that ^{14}C is mainly stored in plant cells as carbon-containing organic matter produced through photosynthesis [528]. ^{14}C in the environment can be used and stored by microorganisms and plants, leading to prolonged exposure to radiation and abnormal cellular metabolism [529]. For higher animals, dietary intake is the main route of ^{14}C exposure, and it is excreted from the body through metabolism. Shipley injected rats with ^{14}C-labeled sodium bicarbonate *via* intravenous injection and extracted different components from the rats after 6 h to measure ^{14}C content. The results showed that the remaining ^{14}C in the fed and fasted rats was 2.5% and 6.3%, respectively, indicating most of ^{14}C in the body can be metabolized and consumed and expelled from the body, and feeding can accelerate this process [530]. ^{14}C can emit low-energy β rays and then cause some effects on cell mortality, DNA base damage, and cancer incidence. Krisch [531] introduced ^{14}C labeled thymine with an activity of 55.4 mCi/mM into the DNA of *E. coli* and stored the bacteria at −196°C for 3 years, the results showed that ^{14}C decay may cause potential damage to microbial DNA. Purdom exposed *Drosophila melanogaster* with 0.1 mCi/g of ^{14}C labeled glucose and the results showed that it led to increased mortality rates [532]. Some studies considered that the transmutation of ^{14}C atoms in DNA molecules to nitrogen is the main factor causing cancer in the body, compared to β rays [533]. Molecular dynamics calculations were used to quantify the impact of ^{14}C-induced bond rupture in a variety of organic molecules, including DNA base pairs. It is found that double bonds and ring structures have radiation resistance, and this structure exists in DNA bases, enhancing their resistance to ^{14}C-induced bond-breaking. At the same time, the sugar groups in DNA and RNA backbones are susceptible to ^{14}C-induced single-strand breaks [534]. Although ^{14}C is the least toxic of all radionuclides, its potential risks should still be paid more attention. Its distribution and effects in tissues and organs of the body, as well as its effects on metabolism and enzyme reaction rate in the body, need to be well researched. Source control of nuclear power plants is also necessary.

12.3 Strontium-90

The decay of ^{90}Sr releases β-rays with an average energy of 0.186 MeV and has a half-life of 28.8 years [511]. The decay process of ^{90}Sr also produces an intermediate product (^{90}Y) that further undergoes rapid decay, releasing β-rays with an energy of 0.934 MeV. Sr and Ca are elements in the same group and share similar properties. When animals ingest ^{90}Sr, it can accumulate in their skeletal system. This accumulation occurs due to the similarity between Sr and Ca, as the body recognizes Sr as a calcium analog and incorporates it into the bone structure. The biological half-life of ^{90}Sr in the bones of dogs, primates, and humans is approximately 400–600 days, leading to long-term exposure of the skeleton to high doses of radiation [535]. ^{90}Sr entering the bone can irradiate the soft and hard tissues around the body, causing bone marrow hypoplasia or various forms of cancer (osteosarcoma leukemia) [536]. Adverse skeletal effects have been documented in both humans and animals following the ingestion of ^{90}Sr. In populations residing near the Techa River, where chronic exposure to radio and other radionuclides

through contaminated food and water occurred, dystrophic lesions of the skeleton primarily impacting articular and periarticular tissues were observed [537]. The occurrence of skeletal lesions was found to be significantly higher when the mean radiation doses to the surface of the bone exceeded 2 Sv.

12.4 Iodine-129 and iodine-131

^{129}I and ^{131}I are the main radioisotopes of iodine released from accidents and effluents of nuclear power plants produced by nuclear fission. Due to the strong solubility of iodine, ^{129}I and ^{131}I are easy to enter into the atmosphere in the form of gas and dissolve in water and soil. However, ^{131}I has a very short half-life of 8 days, while the half-life of ^{129}I is as long as 15.7 million years [511]. Although ^{131}I is more radioactive and toxic than ^{129}I, its long-term effects on the environment and organisms are more limited. In contrast, the long half-life of ^{129}I allows it to persist in the environment for extended periods, posing a potential long-term risk. The thyroid gland, concentrating over 80% of the body's iodine (including ^{129}I), serves as the primary target organ for this element [538]. While potential risks from internal exposure to ^{129}I arise from both inhalation and ingestion of contaminated food, the amount of iodine ingested significantly outweighs the amount inhaled [539]. Due to its indiscriminate uptake of both stable and radioactive iodine, the thyroid's exposure to the β radiation of ^{129}I is the main source of radiation toxicity, which has a risk of causing thyroid cancer [540]. The regulation radiation dose limit of ^{129}I to the thyroid is 0.04 mSv/y [540]. Given the low radiation energy and long half-life of ^{129}I, the molar concentration needed to deliver a radiologically significant dose is comparatively high. Therefore, the chemical toxicity of ^{129}I may be more harmful than its radioactive toxicity [541]. Although ^{129}I is less toxic at the present level, it was reported that ^{129}I stored in unprocessed spend fuel is 10 times more than released to the environment until 2005. Hence, more ^{129}I will be produced with the increase of nuclear power core, and the long-term toxic effects of ^{129}I exposure should still be considered [540].

12.5 Cesium-137

^{137}Cs undergo β decay, releasing β radiation with an energy of 0.187 MeV, an order of magnitude higher than ^{3}H. It has a half-life of 30.2 years and decays into ^{137}mBa, which has a half-life of 2.55 min and emits intense harmful γ radiation with a high energy of 0.662 MeV [511]. The high radiation energy of ^{137}Cs makes it a major concern in nuclear waste and many nuclear accidents [542,543]. γ ray is believed to induce DNA double-strand breaks in cells primarily. At the same time, the indirect effects it generates, such as the generation of reactive oxygen species (ROS), may be responsible for DNA single-strand breaks [544,545]. When only one strand of DNA is broken, it can be rapidly repaired, but more complex repair mechanisms exist to handle double-strand breaks [545]. Due to its longer half-life, ^{137}Cs have a more persistent impact on the environment and organisms. Research indicates that when *Daphnia Magna* accumulates approximately 11.2 Gy of ^{137}Cs dose within their bodies, leading to a significant decrease in egg production and reproductive inhibition; furthermore, under a concentration of 31 mGy/h exposure, the natural growth rate of *Daphnia magna* decreases by 21%, suggesting metabolic inhibition by the high energy γ ray released by ^{137}Cs [546]. Zebrafish larvae (5-6 days post-fertilization) exposed to a daily dose of 30 mGy for 24 hours showed a significant increase in DNA damage (40%–60% DNA in the tail); however, this effect was not observed in the group exposed to a daily dose of 10 mGy [547]. ^{137}Cs can be transferred and enriched along the food chain to higher trophic levels. Their concentration can be increased by 2 to 4 times [543,548]. It can be rapidly and completely absorbed by the body when ingested orally and is excreted mainly through the kidneys, with a biological half-life of about 50–60 days [549]. Cesium has no biological function. However, due to the similarity of its chemical composition, it can replace potassium in the body to some extent. Studies have found that ^{137}Cs, when ingested by dogs, distribute uniformly within their bodies, and their distribution and excretion patterns are similar to those of ^{40}K, which can be attributed to the similar chemical properties of ^{137}Cs and ^{40}K [550]. By collecting blood samples from a healthy population and isolating lymphocytes for exposure to γ-ray irradiation from ^{137}Cs source, the results have shown that γ-ray doses as low as 0.5 cGy can lead to overexpression of the Hsp70 protein, indicating the generation of cellular stress [551].

Overall, the dose coefficient of ^{3}H and ^{14}C is much lower than the other three radionuclides. Despite the low radiation energy of ^{3}H, biomagnification through the food chain and potential incorporation into organic molecules for BTO necessitate careful monitoring and risk assessment. ^{14}C can quickly enter the earth carbon cycle. It will inevitably be absorbed and used by various plants into the food chain, and then have an impact on animals and humans. The accumulation of ^{90}Sr in bones and long biological half-life pose a significant risk for bone marrow and surrounding tissues, potentially leading to various forms of cancer. The long half-life of ^{129}I presents a long-term environmental risk, its low radiation energy suggests that its chemical toxicity may be of great concern. The high-energy γ radiation decayed from ^{137}Cs poses a significant threat to both the environment and human health, with the potential for DNA damage and long-term effects on ecosystems. Further research is still needed to fully understand the complex interactions between these

radionuclides and biological systems. This includes investigating the long-term health effects of chronic low-level exposure, and the potential for synergistic effects between different radionuclides.

13 Summary and outlook

In this review, we systematically summarized the synthesis, structural regulation and functionalization of porous materials and their applications in radionuclides detection and separation, also discussed the chemical and radiotoxicity of different radionuclides. The structural diversity of porous materials endows them with radionuclides separation in different scenarios. The controllable pore size and fine-tuned sites of porous materials provide a broad platform for the detection and separation of radionuclides. Its structural designability, custom functionalization and abundant binding sites make it show great advantages in radionuclides separation. In addition, the combination diversity of structural units, functional sites, and excellent chemical and thermal stability endows porous materials with the ability to handle radionuclides in complex environments. The diverse choices of linker assembly and pore functionalization make porous materials become multifunctional adsorbents, which demonstrate the advantages that traditional adsorbents are difficult to achieve, such as controlling crystal morphology, finely adjusting pore size, increasing active site density, polarity, and ion properties suitable for target radionuclide. Porous materials are booming for the application in radionuclide separation, but several key challenges need to be overcome in practical applications: (i) structural stability: the chemical stability of porous materials is a common challenge under high acid/alkali and high radiation conditions; (ii) separation performance: the separation parameters of porous materials for nuclide separation should be investigated from the actual conditions, such as biofouling, high ionic strength, high acid/alkalinity, selectivity and long-term test under irradiation conditions; (iii) recycle: most of the porous materials in the form of powder, which is difficult to be processed and recycled, resulting in potential secondary troublesome, processing them into devices such as films, foams and gels; (iv) cost: how to simplify the synthesis process, finding inexpensive build block to reduce the synthesis cost, and developing low-energy, large-scale preparation methods in the practical application of radionuclides separation. Porous materials have been proven to be feasible for radionuclides separation, but their application in radionuclides separation is still in the laboratory or small-scale stage, and need further development of their separation performance in amplification experiments. Based on the abovementioned advances, the development of porous materials will play an important role in radionuclides separation, practical devices will be constructed and applied in the near future.

Acknowledgements This work was supported by the National Natural Science Foundation of China (22341602, U2067215, 22006036, U2167218, U2341289, 22327807, 22176077), the Beijing Outstanding Young Scientist Program, and the Fundamental Research Funds for the Central Universities (lzujbky-2023-stlt01).

Conflict of interest The authors declare no conflict of interest.

1 Chu S, Majumdar A. *Nature*, 2012, 488: 294–303
2 Baker RJ. *Coord Chem Rev*, 2014, 266-267: 123–136
3 Zhang H, Li A, Li K, Wang Z, Xu X, Wang Y, Sheridan MV, Hu HS, Xu C, Alekseev EV, Zhang Z, Yan P, Cao K, Chai Z, Albrecht-Schönzart TE, Wang S. *Nature*, 2023, 616: 482–487
4 Wiechert AI, Yiacoumi S, Tsouris C. *Nat Sustain*, 2022, 5: 13–14
5 Hao M, Liu Y, Wu W, Wang S, Yang X, Chen Z, Tang Z, Huang Q, Wang S, Yang H, Wang X. *EnergyChem*, 2023, 5: 100101
6 Wu Y, Pang H, Liu Y, Wang X, Yu S, Fu D, Chen J, Wang X. *Environ Pollut*, 2019, 246: 608–620
7 Sholl DS, Lively RP. *Nature*, 2016, 532: 435–437
8 Wu Y, Xie Y, Liu X, Li Y, Wang J, Chen Z, Yang H, Hu B, Shen C, Tang Z, Huang Q, Wang X. *Coord Chem Rev*, 2023, 483: 215097
9 Yang H, Liu Y, Chen Z, Waterhouse GIN, Ma S, Wang X. *Sci China Chem*, 2022, 65: 2335–2337
10 Mollick S, Saurabh S, More YD, Fajal S, Shirolkar MM, Mandal W, Ghosh SK. *Energy Environ Sci*, 2022, 15: 3462–3469
11 Zhang S, Chen L, Qu Z, Zhai F, Yin X, Zhang D, Shen Y, Li H, Liu W, Mei S, Ji G, Zhang C, Dai X, Chai Z, Wang S. *Chem*, 2023, 9: 3172–3184
12 Zhang H, Fan Y, Krishna R, Feng X, Wang L, Luo F. *Sci Bull*, 2021, 66: 1073–1079
13 Xie Y, Liu Z, Geng Y, Li H, Wang N, Song Y, Wang X, Chen J, Wang J, Ma S, Ye G. *Chem Soc Rev*, 2023, 52: 97–162
14 Gao N, Huang Z, Liu H, Hou J, Liu X. *Chemosphere*, 2019, 237: 124548
15 Li J, Wang X, Zhao G, Chen C, Chai Z, Alsaedi A, Hayat T, Wang X. *Chem Soc Rev*, 2018, 47: 2322–2356
16 Feng L, Wang H, Liu T, Feng T, Cao M, Zhang J, Liu T, Guo Z, Galiotis C, Yuan Y, Wang N. *Nat Sustain*, 2023, 6: 789–796
17 Liu W, Dai X, Bai Z, Wang Y, Yang Z, Zhang L, Xu L, Chen L, Li Y, Gui D, Diwu J, Wang J, Zhou R, Chai Z, Wang S. *Environ Sci Technol*, 2017, 51: 3911–3921
18 Datta SJ, Oleynikov P, Moon WK, Ma Y, Mayoral A, Kim H, Dejoie C, Song MK, Terasaki O, Yoon KB. *Energy Environ Sci*, 2019, 12: 1857–1865
19 Ye T, Qin Y, Liu W, Xia L, Liao J, Yang J, Lan T, Yang Y, Liu N, Li F. *Sep Purif Tech*, 2024, 330: 125284
20 Liu C, Jin Y, Yu Z, Gong L, Wang H, Yu B, Zhang W, Jiang J. *J Am Chem Soc*, 2022, 144: 12390–12399
21 Wang S, Wei G, Xie Y, Shang H, Chen Z, Wang H, Yang H, Waterhouse GIN, Wang X. *Sep Purif Tech*, 2022, 303: 122256
22 Meng C, Du M, Zhang Z, Liu Q, Yan C, Li Z, Dong Z, Luo J, Ma J, Liu Y, Wang X. *Environ Sci Technol*, 2024, 58: 9456–9465
23 Alam MF, Begum ZA, Furusho Y, Hasegawa H, Rahman IMM. *Microchem J*, 2022, 181: 107637
24 Tang JH, Jin JC, Li WA, Zeng X, Ma W, Li JL, Lv TT, Peng YC, Feng ML, Huang XY. *Nat Commun*, 2022, 13: 658
25 Li J, Jin J, Zhang T, Ma W, Zeng X, Sun H, Cheng M, Feng M, Huang X. *ACS EST Water*, 2021, 1: 2440–2449
26 Ma W, Lv TT, Tang JH, Feng ML, Huang XY. *JACS Au*, 2022, 2: 492–501
27 Liu C, Hsu PC, Xie J, Zhao J, Wu T, Wang H, Liu W, Zhang J, Chu S, Cui Y. *Nat Energy*, 2017, 2: 17007
28 Wang Y, Wang Y, Song M, Chen S, Wei J, You J, Zhou B, Wang S.

Angew Chem Int Ed, 2023, 62: e202217601
29 Ye Y, Jin J, Han W, Miao S, Feng Y, Qin Z, Tang X, Li C, Chen Y, Chen F, Wang Y. *Nat Water*, 2023, 1: 887–898
30 Yu F, Li C, Li W, Yu Z, Xu Z, Liu Y, Wang B, Na B, Qiu J. *Adv Funct Mater*, 2023, 34: 2307230
31 Yuan Y, Yu Q, Cao M, Feng L, Feng S, Liu T, Feng T, Yan B, Guo Z, Wang N. *Nat Sustain*, 2021, 4: 708–714
32 Zhou L, Bosscher M, Zhang C, Özçubukçu S, Zhang L, Zhang W, Li CJ, Liu J, Jensen MP, Lai L, He C. *Nat Chem*, 2014, 6: 236–241
33 Wang Z, Ma R, Meng Q, Yang Y, Ma X, Ruan X, Yuan Y, Zhu G. *J Am Chem Soc*, 2021, 143: 14523–14529
34 Yang H, Liu X, Hao M, Xie Y, Wang X, Tian H, Waterhouse GIN, Kruger PE, Telfer SG, Ma S. *Adv Mater*, 2021, 33: 2106621
35 Hao M, Chen Z, Liu X, Liu X, Zhang J, Yang H, Waterhouse GIN, Wang X, Ma S. *CCS Chem*, 2022, 4: 2294–2307
36 Zhang CR, Cui WR, Xu RH, Chen XR, Jiang W, Wu YD, Yan RH, Liang RP, Qiu JD. *CCS Chem*, 2021, 3: 168–179
37 Xie Y, Chen C, Ren X, Wang X, Wang H, Wang X. *Prog Mater Sci*, 2019, 103: 180–234
38 Wang X, Chen L, Wang L, Fan Q, Pan D, Li J, Chi F, Xie Y, Yu S, Xiao C, Luo F, Wang J, Wang X, Chen C, Wu W, Shi W, Wang S, Wang X. *Sci China Chem*, 2019, 62: 933–967
39 Xie Y, Pan T, Lei Q, Chen C, Dong X, Yuan Y, Maksoud WA, Zhao L, Cavallo L, Pinnau I, Han Y. *Nat Commun*, 2022, 13: 2878
40 Xie Y, Pan T, Lei Q, Chen C, Dong X, Yuan Y, Shen J, Cai Y, Zhou C, Pinnau I, Han Y. *Angew Chem Int Ed*, 2021, 60: 22432–22440
41 Banerjee D, Simon CM, Plonka AM, Motkuri RK, Liu J, Chen X, Smit B, Parise JB, Haranczyk M, Thallapally PK. *Nat Commun*, 2016, 7: 11831
42 Carboni M, Abney CW, Liu S, Lin W. *Chem Sci*, 2013, 4: 2396–2402
43 Zhu L, Sheng D, Xu C, Dai X, Silver MA, Li J, Li P, Wang Y, Wang Y, Chen L, Xiao C, Chen J, Zhou R, Zhang C, Farha OK, Chai Z, Albrecht-Schmitt TE, Wang S. *J Am Chem Soc*, 2017, 139: 14873–14876
44 Kang K, Liu S, Zhang M, Li L, Liu C, Lei L, Dai X, Xu C, Xiao C. *Adv Funct Mater*, 2022, 32: 2208148
45 Cui WR, Li FF, Xu RH, Zhang CR, Chen XR, Yan RH, Liang RP, Qiu JD. *Angew Chem Int Ed*, 2020, 132: 17837–17843
46 Li Y, Guo X, Li X, Zhang M, Jia Z, Deng Y, Tian Y, Li S, Ma L. *Angew Chem Int Ed*, 2020, 59: 4168–4175
47 Niu CP, Zhang CR, Liu X, Liang RP, Qiu JD. *Nat Commun*, 2023, 14: 4420
48 Sun Q, Aguila B, Earl LD, Abney CW, Wojtas L, Thallapally PK, Ma S. *Adv Mater*, 2018, 30: 1705479
49 Xiong XH, Yu ZW, Gong LL, Tao Y, Gao Z, Wang L, Yin WH, Yang LX, Luo F. *Adv Sci*, 2019, 6: 1900547
50 Zhang CR, Cui WR, Yi SM, Niu CP, Liang RP, Qi JX, Chen XJ, Jiang W, Liu X, Luo QX, Qiu JD. *Nat Commun*, 2022, 13: 7621
51 Guo X, Li Y, Zhang M, Cao K, Tian Y, Qi Y, Li S, Li K, Yu X, Ma L. *Angew Chem Int Ed*, 2020, 59: 22697–22705
52 He L, Chen L, Dong X, Zhang S, Zhang M, Dai X, Liu X, Lin P, Li K, Chen C, Pan T, Ma F, Chen J, Yuan M, Zhang Y, Chen L, Zhou R, Han Y, Chai Z, Wang S. *Chem*, 2021, 7: 699–714
53 Zhang Z, Dong X, Yin J, Li ZG, Li X, Zhang D, Pan T, Lei Q, Liu X, Xie Y, Shui F, Li J, Yi M, Yuan J, You Z, Zhang L, Chang J, Zhang H, Li W, Fang Q, Li B, Bu XH, Han Y. *J Am Chem Soc*, 2022, 144: 6821–6829
54 Li J, Li B, Shen N, Chen L, Guo Q, Chen L, He L, Dai X, Chai Z, Wang S. *ACS Cent Sci*, 2021, 7: 1441–1450
55 Li X, Li Y, Wang H, Niu Z, He Y, Jin L, Wu M, Wang H, Chai L, Al-Enizi AM, Nafady A, Shaikh SF, Ma S. *Small*, 2021, 17: 2007994
56 Wang B, Li J, Huang H, Liang B, Zhang Y, Chen L, Tan K, Chai Z, Wang S, Wright JT, Meulenberg RW, Ma S. *ACS Cent Sci*, 2024, 10: 426–438
57 Yang X, Wu W, Xie Y, Hao M, Liu X, Chen Z, Yang H, Waterhouse GIN, Ma S, Wang X. *Environ Sci Technol*, 2023, 57: 10870–10881
58 Wang C, Helal AS, Wang Z, Zhou J, Yao X, Shi Z, Ren Y, Lee J, Chang JK, Fugetsu B, Li J. *Adv Mater*, 2021, 33: 2102633
59 Chen Z, Chen W, Jia D, Liu Y, Zhang A, Wen T, Liu J, Ai Y, Song W, Wang X. *Adv Sci*, 2018, 5: 1800235
60 Zhang C, Li X, Chen Z, Wen T, Huang S, Hayat T, Alsaedi A, Wang X. *Sci China Chem*, 2018, 61: 281–293
61 Huang S, Jiang S, Pang H, Wen T, Asiri AM, Alamry KA, Alsaedi A, Wang X, Wang S. *Chem Eng J*, 2019, 368: 941–950
62 Wang Z, Li B, Shang H, Dong X, Huang L, Qing Q, Xu C, Chen J, Liu H, Wang X, Xiong XG, Lu Y. *Green Chem*, 2022, 24: 7092–7099
63 Wang Z, Zhang L, Lei Z, Zheng L, Huang L, Liu S, Lu Y. *Chin Chem Lett*, 2023, 34: 108146
64 Hu E, Chen Q, Gao Q, Fan X, Luo X, Wei Y, Wu G, Deng H, Xu S, Wang P, Liu L, He R, Chen X, Zhu W, Zhu Y. *Adv Funct Mater*, 2024, 34: 2312215
65 Wang H, Guo H, Zhang N, Chen Z, Hu B, Wang X. *Environ Sci Technol*, 2019, 53: 6454–6461
66 Hassan M, Lee S, Mehran MT, Shahzad F, Husnain SM, Ryu HJ. *J Nucl Mater*, 2021, 543: 152566
67 Jun BM, Park CM, Heo J, Yoon Y. *J Environ Manage*, 2020, 256: 109940
68 Wang M, Feng L, Luo G, Feng T, Zhao S, Wang H, Shi S, Liu T, Fu Q, Li J, Wang N, Yuan Y. *J Hazard Mater*, 2023, 445: 130620
69 Yang L, Xiao H, Qian Y, Zhao X, Kong XY, Liu P, Xin W, Fu L, Jiang L, Wen L. *Nat Sustain*, 2022, 5: 71–80
70 Jin K, Lee B, Park J. *Coord Chem Rev*, 2021, 427: 213473
71 Liu X, Pang H, Liu X, Li Q, Zhang N, Mao L, Qiu M, Hu B, Yang H, Wang X. *Innovation*, 2021, 2: 100076
72 Mei D, Liu L, Yan B. *Coord Chem Rev*, 2023, 475: 214917
73 Tang N, Liang J, Niu C, Wang H, Luo Y, Xing W, Ye S, Liang C, Guo H, Guo J, Zhang Y, Zeng G. *J Mater Chem A*, 2020, 8: 7588–7625
74 Li Y, Wang S, Wang X. *EcoEnergy*, 2024, 2: 205–219
75 Qu Z, Leng R, Wang S, Ji Z, Wang X. *Rev EnvContamination (formerly-Residue Rev)*, 2024, 262: 12
76 Li S, Wang L, Peng J, Zhai M, Shi W. *Chem Eng J*, 2019, 366: 192–199
77 Wang Z, Zhang L, Zhang K, Lu Y, Chen J, Wang S, Hu B, Wang X. *Chemosphere*, 2022, 287: 132313
78 Wang J, Wang Y, Wang W, Ding Z, Geng R, Li P, Pan D, Liang J, Qin H, Fan Q. *Chem Eng J*, 2020, 383: 123193
79 Ju Y, Li ZJ, Qiu J, Li X, Yang J, Zhang ZH, He MY, Wang JQ, Lin J. *Inorg Chem*, 2023, 62: 8158–8165
80 Liu W, Dai X, Wang Y, Song L, Zhang L, Zhang D, Xie J, Chen L, Diwu J, Wang J, Chai Z, Wang S. *Environ Sci Technol*, 2019, 53: 332–341
81 Díaz U, Corma A. *Coord Chem Rev*, 2016, 311: 85–124
82 Gou X, Zhang Q, Wu Y, Zhao Y, Shi X, Fan X, Huang L, Lu G. *RSC Adv*, 2016, 6: 39198–39203
83 Jiang D. *Bull Chem Soc Jpn*, 2021, 94: 1215–1231
84 Song T, Liu Z, Yun Q, Zhang X, Yuan K, Hu W. *TrAC Trends Anal Chem*, 2024, 171: 117500
85 Rasheed T, Khan S, Ahmad T, Ullah N. *Chem Record*, 2022, 22: e202200062
86 Zhang Y, Wang Q, Li Y, Hu R. *Microporous Mesoporous Mater*, 2022, 346: 112289
87 Hu K, Wang Y, Wang G, Wu Y, He Q. *Food Chem*, 2023, 429: 136801
88 Cui J, Zhang Y, Lun K, Wu B, He L, Wang M, Fang S, Zhang Z, Zhou L. *Microchim Acta*, 2023, 190: 421
89 Niu CP, Zhang CR, Cui WR, Yi SM, Liang RP, Qiu JD. *J Hazard Mater*, 2022, 425: 127951
90 Cui WR, Chen YR, Xu W, Liu K, Qiu WB, Li Y, Qiu JD. *Sep Purif Tech*, 2023, 306: 122726
91 Roozbahani GM, Chen X, Zhang Y, Juarez O, Li D, Guan X. *Anal Chem*, 2018, 90: 5938–5944

92 Gomaa H, Emran MY, Elsenety MM, Abdel-Rahim RD, Deng Q, Gadallah MI, Saad M, ALMohiy H, Ezzeldien M, Seaf El-Nasr TA, El-Gaby MSA, Aboraia AM. *ACS Sustain Chem Eng*, 2023, 11: 2127–2138
93 Moghaddam ZS, Kaykhaii M, Khajeh M, Oveisi AR. *Spectrochim Acta Part A-Mol Biomol Spectr*, 2018, 194: 76–82
94 Cui WR, Zhang CR, Jiang W, Li FF, Liang RP, Liu J, Qiu JD. *Nat Commun*, 2020, 11: 436
95 Song J, Zhao L, Wang Y, Xue Y, Deng Y, Zhao X, Li Q. *Nanomaterials*, 2018, 8: 1043
96 Xiao SJ, Qiu AT, Li HH, Wang MP, Zhang L, Guo KX, Guo J, Qiu JD. *Spectrochim Acta Part A-Mol Biomol Spectr*, 2023, 289: 122182
97 Mei D, Yan B. *ACS Appl Mater Interfaces*, 2023, 15: 16882–16894
98 Naguib M, Barsoum MW, Gogotsi Y. *Adv Mater*, 2021, 33: 2103393
99 Abney CW, Mayes RT, Saito T, Dai S. *Chem Rev*, 2017, 117: 13935–14013
100 Guo H, Mei P, Xiao J, Huang X, Ishag A, Sun Y. *Chemosphere*, 2021, 278: 130411
101 Lin X, Xuan D, Liang H, Xiao F, Li F, Liu C, Fan P, Hu C, Yang S, Liu Y. *J Environ Radioact*, 2020, 220-221: 106299
102 Li Y, Wang Z, Liu C, Zhang D, Liao L, Xiao X. *Z anorg allge Chem*, 2021, 647: 1914–1920
103 Dewangan PK, Khan F, Shrivas K, Sahu V. *J Radioanal Nucl Chem*, 2019, 320: 757–763
104 Peng J, Chen X, Ong WJ, Zhao X, Li N. *Chem*, 2019, 5: 18–50
105 Ran J, Gao G, Li FT, Ma TY, Du A, Qiao SZ. *Nat Commun*, 2017, 8: 13907
106 Jun BM, Kim S, Heo J, Park CM, Her N, Jang M, Huang Y, Han J, Yoon Y. *Nano Res*, 2019, 12: 471–487
107 Khan AR, Husnain SM, Shahzad F, Mujtaba-ul-Hassan S, Mehmood M, Ahmad J, Mehran MT, Rahman S. *Dalton Trans*, 2019, 48: 11803–11812
108 Depauw A, Jonusauskaite L, Ghasemi R, Lefevre JP, Mongin C, Génot V, Delaire J, Leray I. *Sensors*, 2023, 23: 7826
109 Zhang J, Chen L, Dai X, Zhu L, Xiao C, Xu L, Zhang Z, Alekseev EV, Wang Y, Zhang C, Zhang H, Wang Y, Diwu J, Chai Z, Wang S. *Chem*, 2019, 5: 977–994
110 Qin X, Yang W, Yang Y, Gu D, Guo D, Pan Q. *Inorg Chem*, 2020, 59: 9857–9865
111 Wang Y, Liu Z, Li Y, Bai Z, Liu W, Wang Y, Xu X, Xiao C, Sheng D, Diwu J, Su J, Chai Z, Albrecht-Schmitt TE, Wang S. *J Am Chem Soc*, 2015, 137: 6144–6147
112 Orfano M, Perego J, Cova F, Bezuidenhout CX, Piva S, Dujardin C, Sabot B, Pierre S, Mai P, Daniel C, Bracco S, Vedda A, Comotti A, Monguzzi A. *Nat Photon*, 2023, 17: 672–678
113 He W, Hua D. *Talanta*, 2019, 201: 317–329
114 Bai Y, Xu L, Chai H, Zhou L, Jiang G, Zhang G. *Front Chem*, 2022, 10: 882250
115 Wang N, Du J, Li X, Ji X, Wu Y, Sun Z. *Anal Chem*, 2023, 95: 12956–12963
116 Wen J, Huang Z, Hu S, Li S, Li W, Wang X. *J Hazard Mater*, 2016, 318: 363–370
117 Meir R, Zverzhinetsky M, Harpak N, Borberg E, Burstein L, Zeiri O, Krivitsky V, Patolsky F. *Anal Chem*, 2020, 92: 12528–12537
118 Roozbahani GM, Chen X, Zhang Y, Xie R, Ma R, Li D, Li H, Guan X. *ACS Sens*, 2017, 2: 703–709
119 Cotruvo JA. *J AWWA*, 2017, 109: 44–51
120 Li L, Shen S, Su J, Ai W, Bai Y, Liu H. *Anal Bioanal Chem*, 2019, 411: 4213–4220
121 Chen WM, Meng XL, Zhuang GL, Wang Z, Kurmoo M, Zhao QQ, Wang XP, Shan B, Tung CH, Sun D. *J Mater Chem A*, 2017, 5: 13079–13085
122 Hou JX, Gao JP, Liu J, Jing X, Li LJ, Du JL. *Dyes Pigments*, 2019, 160: 159–164
123 Zhang J, Ren Y, Xia T, Du Y, Shao L, Tang H, Yang S. *Z anorg allge Chem*, 2022, 648: e202100337
124 Riley BJ, Vienna JD, Strachan DM, McCloy JS, Jerden Jr. JL. *J Nucl Mater*, 2016, 470: 307–326
125 Santschi PH, Xu C, Zhang S, Schwehr KA, Grandbois R, Kaplan DI, Yeager CM. *Appl GeoChem*, 2017, 85: 121–127
126 Nandanwar SU, Coldsnow K, Utgikar V, Sabharwall P, Eric Aston D. *Chem Eng J*, 2016, 306: 369–381
127 Zhang L, Zhou Y, Han S. *Angew Chem Int Ed*, 2021, 60: 15192–15212
128 Achmann S, Hagen G, Kita J, Malkowsky IM, Kiener C, Moos R. *Sensors*, 2009, 9: 1574–1589
129 Small LJ, Hill RC, Krumhansl JL, Schindelholz ME, Chen Z, Chapman KW, Zhang X, Yang S, Schröder M, Nenoff TM. *ACS Appl Mater Interfaces*, 2019, 11: 27982–27988
130 Small LJ, Nenoff TM. *ACS Appl Mater Interfaces*, 2017, 9: 44649–44655
131 Kobayashi Y, Jacobs B, Allendorf MD, Long JR. *Chem Mater*, 2010, 22: 4120–4122
132 Yousefi SR, Ahmadi SJ, Shemirani F, Jamali MR, Salavati-Niasari M. *Talanta*, 2009, 80: 212–217
133 Falaise C, Volkringer C, Giovine R, Prelot B, Huve M, Loiseau T. *Dalton Trans*, 2017, 46: 12010–12014
134 Al-Kady AS. *Sens Actuat B-Chem*, 2012, 166-167: 485–491
135 Kumar A, Ali M, Ningthoujam RS, Gaikwad P, Kumar M, Nath BB, Pandey BN. *J Hazard Mater*, 2016, 307: 281–293
136 Stradling GN, Moody JC, Gray SA, Ellender M, Hodgson A. *Hum Exp Toxicol*, 1991, 10: 15–20
137 Kumar A, Mishra P, Ghosh S, Sharma P, Ali M, Pandey BN, Mishra KP. *Int J Radiat Biol*, 2008, 84: 337–349
138 Song L, Liu W, Wang Y, Chen L, Wang XF, Wang S. *CrystEngComm*, 2019, 21: 3471–3477
139 Fang Y, Li C, Wu L, Bai B, Li X, Jia Y, Feng W, Yuan L. *Dalton Trans*, 2015, 44: 14584–14588
140 Liu H, Yonezawa A, Kumagai K, Sano M, Miyake T. *J Mater Chem A*, 2015, 3: 1562–1568
141 Namiki Y, Namiki T, Ishii Y, Koido S, Nagase Y, Tsubota A, Tada N, Kitamoto Y. *Pharm Res*, 2012, 29: 1404–1418
142 Gao YJ, Feng ML, Zhang B, Wu ZF, Song Y, Huang XY. *J Mater Chem A*, 2018, 6: 3967–3976
143 Mauree S, Villemot V, Hamel M, Sabot B, Pierre S, Dujardin C, Belloni F, Comotti A, Bracco S, Perego J, Bertrand GHV. *Adv Funct Mater*, 2023, 33: 2302877
144 Yuan Y, Feng S, Feng L, Yu Q, Liu T, Wang N. *Angew Chem Int Ed*, 2020, 59: 4262–4268
145 Feng L, Wang H, Feng T, Yan B, Yu Q, Zhang J, Guo Z, Yuan Y, Ma C, Liu T, Wang N. . *Angew Chem Int Ed*, 2022, 61: e202101015
146 Chen M, Liu T, Zhang X, Zhang R, Tang S, Yuan Y, Xie Z, Liu Y, Wang H, Fedorovich KV, Wang N. *Adv Funct Mater*, 2021, 31: 2100106
147 Zhang H, Liu W, Li A, Zhang D, Li X, Zhai F, Chen L, Chen L, Wang Y, Wang S. *Angew Chem Int Ed*, 2019, 58: 16110–16114
148 Zhang QY, Zhang LJ, Zhu JQ, Gong LL, Huang ZC, Gao F, Wang JQ, Xie XQ, Luo F. *Nat Commun*, 2024, 15: 453
149 Wang X, Chen L, Bai Z, Zhang D, Guan J, Zhang Y, Shi C, Diwu J. *Angew Chem Int Ed*, 2021, 60: 1646–1650
150 Guo XG, Su J, Xie WQ, Ni SN, Gao Y, Su X, Sun XQ. *Dalton Trans*, 2020, 49: 4060–4066
151 Song A, Yang M-, Wu Z, Yang Q, Lin B, Liang R, Qiu J. *Adv Funct Mater*, 2024, 34: 2406932
152 Mu W, Du S, Li X, Yu Q, Hu R, Wei H, Yang Y, Peng S. *Dalton Trans*, 2019, 48: 3284–3290
153 Feng L, Chen X, Cao M, Zhao S, Wang H, Chen D, Ma Y, Liu T, Wang N, Yuan Y. *Angew Chem Int Ed*, 2023, 62: e202312894
154 Zhang J, Chen L, Dai X, Chen L, Zhai F, Yu W, Guo S, Yang L, Chen L, Zhang Y, He L, Chen C, Chai Z, Wang S. *Chem Commun*, 2021, 57: 8452–8455
155 Zhao X, Zhao J, Sun Y, Ouyang H, Chen N, Ren J, Li Y, Chen S, Yang D, Xing B. *J Hazard Mater*, 2022, 424: 127715
156 Li L, Guo L, Zhang Z, Yang Q, Yang Y, Bao Z, Ren Q, Li J. *J Am*

Chem Soc, 2019, 141: 9358–9364
157 Le QTN, Cho K. *J Colloid Interface Sci*, 2021, 581: 741–750
158 Asgari P, Mousavi SH, Aghayan H, Ghasemi H, Yousefi T. *Micro-Chem J*, 2019, 150: 104188
159 Lin S, Zhao Y, Bediako JK, Cho CW, Sarkar AK, Lim CR, Yun YS. *Chem Eng J*, 2019, 362: 280–286
160 Tang J, Zhao J, Wang S, Zhang L, Zhao M, Huang Z, Hu Y. *Chem Eng J*, 2021, 407: 127223
161 Hu QH, Song AM, Gao X, Shi YZ, Jiang W, Liang RP, Qiu JD. *Nat Commun*, 2024, 15: 1558
162 Sheng D, Zhu L, Dai X, Xu C, Li P, Pearce CI, Xiao C, Chen J, Zhou R, Duan T, Farha OK, Chai Z, Wang S. *Angew Chem Int Ed*, 2019, 58: 4968–4972
163 Li CP, Ai JY, Zhou H, Chen Q, Yang Y, He H, Du M. *Chem Commun*, 2019, 55: 1841–1844
164 Xu H, Cao C-, Hu H-, Wang S-, Liu J-, Cheng P, Kaltsoyannis N, Li J, Zhao B. *Angew Chem Int Ed*, 2019, 58: 6022–6027
165 Huang M, Lou Z, Zhao W, Lu A, Hao X, Wang Y, Feng X, Shan W, Xiong Y. *J Hazard Mater*, 2022, 422: 126871
166 Shen N, Yang Z, Liu S, Dai X, Xiao C, Taylor-Pashow K, Li D, Yang C, Li J, Zhang Y, Zhang M, Zhou R, Chai Z, Wang S. *Nat Commun*, 2020, 11: 5571
167 Kang K, Dai X, Shen N, Xie R, Zhang X, Lei L, Wang S, Xiao C. *Chem Eur J*, 2021, 27: 5632–5637
168 Sharma S, Desai AV, Joarder B, Ghosh SK. *Angew Chem Int Ed*, 2020, 59: 7788–7792
169 Sharma S, Let S, Desai AV, Dutta S, Karuppasamy G, Shirolkar MM, Babarao R, Ghosh SK. *J Mater Chem A*, 2021, 9: 6499–6507
170 Andrade PHM, Henry N, Volkringer C, Loiseau T, Vezin H, Hureau M, Moissette A. *ACS Appl Mater Interfaces*, 2022, 14: 29916–29933
171 Chen P, He X, Pang M, Dong X, Zhao S, Zhang W. *ACS Appl Mater Interfaces*, 2020, 12: 20429–20439
172 Zhao Q, Zhu L, Lin G, Chen G, Liu B, Zhang L, Duan T, Lei J. *ACS Appl Mater Interfaces*, 2019, 11: 42635–42645
173 Yu Y, Ren L, Liu M, Huang S, Xiao X, Liu R, Wang L, Xu W. *ACS Appl Mater Interfaces*, 2019, 11: 31291–31301
174 Liu Y, Wu H, Guo L, Zhou W, Zhang Z, Yang Q, Yang Y, Ren Q, Bao Z. *Angew Chem Int Ed*, 2022, 61: e202117609
175 Wang H, Shi Z, Yang J, Sun T, Rungtaweevoranit B, Lyu H, Zhang Y-, Yaghi OM. *Angew Chem Int Ed*, 2021, 60: 3417–3421
176 Wang Q, Ke T, Yang L, Zhang Z, Cui X, Bao Z, Ren Q, Yang Q, Xing H. *Angew Chem Int Ed*, 2020, 59: 3423–3428
177 Xie Y, Ding X, Wang J, Ye G. *Angew Chem Int Ed*, 2023, 62: e202313951
178 Zeng J, Fu Y, Wu Y, Wang S, Zhang W, Ma H. *Angew Chem Int Ed*, 2023, 62: e202310235
179 Zheng F, Guo L, Chen R, Chen L, Zhang Z, Yang Q, Yang Y, Su B, Ren Q, Bao Z. *Angew Chem Int Ed*, 2022, 61: e202116686
180 Gong W, Xie Y, Wang X, Kirlikovali KO, Idrees KB, Sha F, Xie H, Liu Y, Chen B, Cui Y, Farha OK. *J Am Chem Soc*, 2023, 145: 2679–2689
181 Pei J, Gu XW, Liang CC, Chen B, Li B, Qian G. *J Am Chem Soc*, 2022, 144: 3200–3209
182 Wang H, Warren M, Jagiello J, Jensen S, Ghose SK, Tan K, Yu L, Emge TJ, Thonhauser T, Li J. *J Am Chem Soc*, 2020, 142: 20088–20097
183 Zhou J, Ke T, Steinke F, Stock N, Zhang Z, Bao Z, He X, Ren Q, Yang Q. *J Am Chem Soc*, 2022, 144: 14322–14329
184 Zhou Y, Wang J, Zhao Y, Gu H, Chen Z, Yang H, Wang X. *Front Chem Sci Eng*, 2023, 17: 1895–1912
185 Wang X, Ma F, Liu S, Chen L, Xiong S, Dai X, Tai B, He L, Yuan M, Mi P, Gong S, Li G, Tao Y, Wan J, Chen L, Sun X, Tang Q, He L, Yang Z, Chai Z, Wang S. *J Am Chem Soc*, 2022, 144: 13634–13642
186 Cote AP, Benin AI, Ockwig NW, O'Keeffe M, Matzger AJ, Yaghi OM. *Science*, 2005, 310: 1166–1170
187 Yuan S, Li X, Zhu J, Zhang G, Van Puyvelde P, Van der Bruggen B. *Chem Soc Rev*, 2019, 48: 2665–2681
188 Feng X, Ding X, Jiang D. *Chem Soc Rev*, 2012, 41: 6010–6022
189 Xue R, Liu YS, Yang W, Yang GY. *Coord Chem Rev*, 2024, 501: 215577
190 Wang H, Yang Y, Yuan X, Liang Teo W, Wu Y, Tang L, Zhao Y. *Mater Today*, 2022, 53: 106–133
191 Guan Q, Zhou LL, Dong YB. *Chem Soc Rev*, 2022, 51: 6307–6416
192 Fischbach DM, Rhoades G, Espy C, Goldberg F, Smith BJ. *Chem Commun*, 2019, 55: 3594–3597
193 Dey K, Pal M, Rout KC, Kunjattu H S, Das A, Mukherjee R, Kharul UK, Banerjee R. *J Am Chem Soc*, 2017, 139: 13083–13091
194 Ritchie LK, Trewin A, Reguera-Galan A, Hasell T, Cooper AI. *Microporous Mesoporous Mater*, 2010, 132: 132–136
195 Zhang M, Chen J, Zhang S, Zhou X, He L, Sheridan MV, Yuan M, Zhang M, Chen L, Dai X, Ma F, Wang J, Hu J, Wu G, Kong X, Zhou R, Albrecht-Schmitt TE, Chai Z, Wang S. *J Am Chem Soc*, 2020, 142: 9169–9174
196 Lv H, Zhao X, Niu H, He S, Tang Z, Wu F, Giesy JP. *J Hazard Mater*, 2019, 369: 494–502
197 Yang ST, Kim J, Cho HY, Kim S, Ahn WS. *RSC Adv*, 2012, 2: 10179–10181
198 Kuhn P, Antonietti M, Thomas A. *Angew Chem Int Ed*, 2008, 47: 3450–3453
199 Bojdys MJ, Jeromenok J, Thomas A, Antonietti M. *Adv Mater*, 2010, 22: 2202–2205
200 Vardhan H, Rummer G, Deng A, Ma S. *Membranes*, 2023, 13: 696
201 Bunck DN, Dichtel WR. *Angew Chem Int Ed*, 2012, 51: 1885–1889
202 Lanni LM, Tilford RW, Bharathy M, Lavigne JJ. *J Am Chem Soc*, 2011, 133: 13975–13983
203 Keller N, Bessinger D, Reuter S, Calik M, Ascherl L, Hanusch FC, Auras F, Bein T. *J Am Chem Soc*, 2017, 139: 8194–8199
204 Chen L, He L, Ma F, Liu W, Wang Y, Silver MA, Chen L, Zhu L, Gui D, Diwu J, Chai Z, Wang S. *ACS Appl Mater Interfaces*, 2018, 10: 15364–15368
205 Diercks CS, Lin S, Kornienko N, Kapustin EA, Nichols EM, Zhu C, Zhao Y, Chang CJ, Yaghi OM. *J Am Chem Soc*, 2018, 140: 1116–1122
206 He S, Yin B, Niu H, Cai Y. *Appl Catal B-Environ*, 2018, 239: 147–153
207 Zhang L, Wang SL, Zhang GH, Shen N, Chen H, Tao G, Tao GH, Yong F, Fu J, Zhu QH, He L. *Cell Rep Phys Sci*, 2022, 3: 101114
208 Yu J, Lan J, Wang S, Zhang P, Liu K, Yuan L, Chai Z, Shi W. *Dalton Trans*, 2021, 50: 3792–3796
209 Chen X, Addicoat M, Irle S, Nagai A, Jiang D. *J Am Chem Soc*, 2013, 135: 546–549
210 Nagai A, Guo Z, Feng X, Jin S, Chen X, Ding X, Jiang D. *Nat Commun*, 2011, 2: 536
211 Huang N, Krishna R, Jiang D. *J Am Chem Soc*, 2015, 137: 7079–7082
212 Waller PJ, Lyle SJ, Osborn Popp TM, Diercks CS, Reimer JA, Yaghi OM. *J Am Chem Soc*, 2016, 138: 15519–15522
213 Yang S, Sa R, Zhong H, Lv H, Yuan D, Wang R. *Adv Funct Mater*, 2022, 32: 2110694
214 Qian C, Zhou W, Qiao J, Wang D, Li X, Teo WL, Shi X, Wu H, Di J, Wang H, Liu G, Gu L, Liu J, Feng L, Liu Y, Quek SY, Loh KP, Zhao Y. *J Am Chem Soc*, 2020, 142: 18138–18149
215 Waller PJ, AlFaraj YS, Diercks CS, Jarenwattananon NN, Yaghi OM. *J Am Chem Soc*, 2018, 140: 9099–9103
216 Yang S, Yang C, Dun C, Mao H, Khoo RSH, Klivansky LM, Reimer JA, Urban JJ, Zhang J, Liu Y. *J Am Chem Soc*, 2022, 144: 9827–9835
217 Zhou ZB, Tian PJ, Yao J, Lu Y, Qi QY, Zhao X. *Nat Commun*, 2022, 13: 2180
218 Wei PF, Qi MZ, Wang ZP, Ding SY, Yu W, Liu Q, Wang LK, Wang HZ, An WK, Wang W. *J Am Chem Soc*, 2018, 140: 4623–4631
219 Li X, Zhang C, Cai S, Lei X, Altoe V, Hong F, Urban JJ, Ciston J, Chan EM, Liu Y. *Nat Commun*, 2018, 9: 2998
220 Liu L, Zhao B, Wu D, Wang X, Yao W, Ma Z, Hou H, Yu S.

Chemosphere, 2023, 341: 140086
221 Endrizzi F, Rao L. *Chem Eur J*, 2014, 20: 14499–14506
222 Wu YD, Cui WR, Zhang CR, Liang RP, Qiu JD. *Environ Chem Lett*, 2021, 19: 1847–1856
223 Xie Y, Wu Y, Liu X, Hao M, Chen Z, Waterhouse GIN, Wang X, Yang H, Ma S. *Cell Rep Phys Sci*, 2023, 4: 101220
224 Chen Z, Wang J, Hao M, Xie Y, Liu X, Yang H, Waterhouse GIN, Wang X, Ma S. *Nat Commun*, 2023, 14: 1106
225 Yang H, Hao M, Xie Y, Liu X, Liu Y, Chen Z, Wang X, Waterhouse GIN, Ma S. *Angew Chem Int Ed*, 2023, 62: e202303129
226 Zhang M, Li Y, Yuan W, Guo X, Bai C, Zou Y, Long H, Qi Y, Li S, Tao G, Xia C, Ma L. *Angew Chem Int Ed*, 2021, 60: 12396–12405
227 Hao M, Xie Y, Lei M, Liu X, Chen Z, Yang H, Waterhouse GIN, Ma S, Wang X. *J Am Chem Soc*, 2023, 146: 1904–1913
228 Xie Y, Rong Q, Mao F, Wang S, Wu Y, Liu X, Hao M, Chen Z, Yang H, Waterhouse GIN, Ma S, Wang X. *Nat Commun*, 2024, 15: 2671
229 Zhang P, Wang Z, Wang S, Wang J, Liu J, Wang T, Chen Y, Cheng P, Zhang Z. *Angew Chem Int Ed*, 2022, 61: e202213247
230 Liu X, Gao F, Jin T, Ma K, Shi H, Wang M, Gao Y, Xue W, Zhao J, Xiao S, Ouyang Y, Ye G. *Nat Commun*, 2023, 14: 5097
231 Qi S, Guo R, Bi Z, Zhang Z, Li C, Pan W. *Small*, 2023, 19: 2303632
232 Medina DD, Sick T, Bein T. *Adv Energy Mater*, 2017, 7: 1700387
233 Guo K, Zhu X, Peng L, Fu Y, Ma R, Lu X, Zhang F, Zhu W, Fan M. *Chem Eng J*, 2021, 405: 127011
234 Babu HV, Bai MGM, Rajeswara Rao M. *ACS Appl Mater Interfaces*, 2019, 11: 11029–11060
235 Li X, Jia Z, Zhang J, Zou Y, Zhang Y, Shu K, Liu W, Liu N, Li Y, Ma L. *Small*, 2023, 19: 2303775
236 Zhang CR, Qi JX, Cui WR, Chen XJ, Liu X, Yi SM, Niu CP, Liang RP, Qiu JD. *Sci China Chem*, 2023, 66: 562–569
237 Madhura L, Kanchi S, Sabela MI, Singh S, Bisetty K, Inamuddin K. *Environ Chem Lett*, 2018, 16: 343–365
238 Elmerhi N, Kumar S, Abi Jaoude M, Shetty D. *Chem - An Asian J*, 2024, 19: e202300944
239 Wang Z, Zhang S, Chen Y, Zhang Z, Ma S. *Chem Soc Rev*, 2020, 49: 708–735
240 Xiong XH, Tao Y, Yu ZW, Yang LX, Sun LJ, Fan YL, Luo F. *Chem Eng J*, 2020, 384: 123240
241 Liu X, Peng ZH, Lei L, Bi RX, Zhang CR, Luo QX, Liang RP, Qiu JD. *Appl Catal B-Environ*, 2024, 342: 123460
242 Bi RX, Liu X, Lei L, Peng ZH, Wang XX, Zhang L, Liang RP, Qiu JD. *Chem Eng J*, 2024, 485: 150026
243 Yin ZJ, Xu SQ, Zhan TG, Qi QY, Wu ZQ, Zhao X. *Chem Commun*, 2017, 53: 7266–7269
244 Zhang SY, Tang XH, Yan YL, Li SQ, Zheng S, Fan J, Li X, Zhang WG, Cai S. *ACS Macro Lett*, 2021, 10: 1590–1596
245 Zhou B, Chen Z, Feng S, Wang D, Liu H. *Macromolecules*, 2021, 54: 7642–7652
246 Yan Z, Yuan Y, Tian Y, Zhang D, Zhu G. *Angew Chem Int Ed*, 2015, 54: 12733–12737
247 Shreeraj G, Sah A, Sarkar S, Giri A, Sahoo A, Patra A. *Langmuir*, 2023, 39: 16069–16078
248 Luo D, He Y, Tian J, Sessler JL, Chi X. *J Am Chem Soc*, 2022, 144: 113–117
249 Wang Z, Huang Y, Yang J, Li Y, Zhuang Q, Gu J. *Dalton Trans*, 2017, 46: 7412–7420
250 Zhai L, Sun S, Chen P, Zhang Y, Sun Q, Xu Q, Wu Y, Nie R, Li Z, Mi L. *Mater Chem Front*, 2021, 5: 5463–5470
251 Wang H, Zeng C, Wang C, Fu J, Li Y, Yang Y, Du Z, Tao G, Sun Q, Zhai T, Li H. *Nat Mater*, 2024, 23: 596–603
252 Li X, Jia Z, Zhang J, Zou Y, Jiang B, Zhang Y, Shu K, Liu N, Li Y, Ma L. *Chem Mater*, 2022, 34: 11062–11071
253 Chakraborty S, Vimalnath KV, Lohar SP, Shetty P, Dash A. *J Radioanal Nucl Chem*, 2014, 302: 233–243
254 Peng H, Li F, Qin Y, Shi S, Ma G, Fan X, Li Y, Ma L, Liu N. *ACS Appl Mater Interfaces*, 2024, 16: 9343–9354
255 Yang S, Yin J, Li Q, Wang C, Hua D, Wu N. *J Hazard Mater*, 2022, 429: 128315
256 Hao M, Chen Z, Yang H, Waterhouse GIN, Ma S, Wang X. *Sci Bull*, 2022, 67: 924–932
257 Zu J, Diao J, Han G, Xue W, Pan X, Jin M, Tang Q. *Sep Purif Tech*, 2024, 338: 126455
258 Xie Y, Rong Q, Wen C, Liu X, Hao M, Chen Z, Yang H, Waterhouse GIN, Ma S, Wang X. *CCS Chem*, 2024, 6: 1908–1919
259 Jia Z, Yan Z, Zhang J, Zou Y, Qi Y, Li X, Li Y, Guo X, Yang C, Ma L. *ACS Appl Mater Interfaces*, 2021, 13: 1127–1134
260 Yu J, Yuan L, Wang S, Lan J, Zheng L, Xu C, Chen J, Wang L, Huang Z, Tao W, Liu Z, Chai Z, Gibson JK, Shi W. *CCS Chem*, 2019, 1: 286–295
261 Li L, Ma W, Shen S, Huang H, Bai Y, Liu H. *ACS Appl Mater Interfaces*, 2016, 8: 31032–31041
262 You Z, Zhang N, Guan Q, Xing Y, Bai F, Sun L. *J Inorg Organomet Polym*, 2020, 30: 1966–1979
263 Cheng G, Zhang A, Zhao Z, Chai Z, Hu B, Han B, Ai Y, Wang X. *Sci Bull*, 2021, 66: 1994–2001
264 Yang T, Tian C, Yan X, Xiao R, Lin Z. *Environ Sci-Nano*, 2021, 8: 1469–1480
265 Song S, Shi Y, Liu N, Liu F. *ACS Appl Mater Interfaces*, 2021, 13: 10513–10523
266 Yang Y, Xiong X, Fan Y, Lai Z, Xu Z, Luo F. *J Solid State Chem*, 2019, 279: 120979
267 Sun Y, Kang Y, Zhong W, Liu Y, Dai Y. *J Solid State Chem*, 2020, 292: 121731
268 Deng S, Yu C, Niu J, Liao J, Liu X. *Chem Eng J*, 2020, 392: 123815
269 Majdoubi H, Şimşek S, El Kaim Billah R, Koçak N, Kaya S, Tamraoui Y, Katin KP, Hannache H, Marzouki R. *J Mol Liq*, 2024, 395: 123951
270 Zhang X, Luo C, Li H, Liu R, Wang H, Liu L, Yue C. *Reactive Funct Polyms*, 2023, 190: 105648
271 Cao M, Luo G, Peng Q, Wang L, Wang Y, Zhao S, Wang H, Zhang J, Yuan Y, Wang N. *Chem Eng J*, 2024, 481: 148536
272 Yang J, Li Y, Tian T, Shi H, Ahmad Z, Geng N, Jin J, Huang Y, Zhang H, Fan H, Chen J. *Chem Eng J*, 2023, 465: 142952
273 Wang Y, Lin Z, Yu J, Zhu J, Liu J, Liu Q, Chen R, Liu P, Wang J. *J Environ Chem Eng*, 2023, 11: 109277
274 Tian Y, Liu L, Wang Y, Ma F, Zhang C, Dong H. *Environ Res*, 2023, 231: 116160
275 Tian Y, Liu L, Ma F, Zhu X, Dong H, Zhang C, Zhao F. *J Hazard Mater*, 2021, 419: 126538
276 Li Y, Wang ZY, Ren Q, Zhang F, Li XX, Wu Q, Hua R, Yan ZY, Wang Y. *Chemosphere*, 2023, 337: 139321
277 Zhang X, Yang X, Rong Q, Liu X, Zhou Y, Yang H, Wang G, Chen Z, Wang X. *ACS EST Eng*, 2024, 4: 250–268
278 Li H, Li L, Wen J, Ye G, Chen J, Wang X. *Chem Eng J*, 2023, 456: 140935
279 Yue C, Liu R, YinghaoYu R, Wan Q, Wang H, Liu L, Zhang X. *J Water Process Eng*, 2023, 53: 103582
280 Ahmad M, Chen J, Yang K, Shah T, Naik M, Zhang Q, Zhang B. *Chem Eng J*, 2021, 418: 129370
281 Tian Y, Wang Y, Liu L, Dong H, Zhu X, Ma F, Zhang C. *J Mol Liq*, 2023, 372: 121171
282 Zhang Q, Zeng K, Wang C, Wei P, Zhao X, Wu F, Liu Z. *New J Chem*, 2022, 46: 9238–9249
283 Xu Z, Yu S, Wang J, Yu F, Xu M, Xiong J, Xiao S, Liu Y, He Y, Xu J, Zhang Z, Qiu J. *Sep Purif Tech*, 2023, 309: 122953
284 Li Y, Li XX, Wang ZY, Zhang F, Wu Q, Sha LT, Wang Y, Yan ZY. *Sep Purif Tech*, 2022, 302: 122115
285 Leng R, Sun Y, Wang C, Qu Z, Feng R, Zhao G, Han B, Wang J, Ji Z, Wang X. *Environ Sci Technol*, 2023, 57: 9615–9626
286 Zhong X, Ling Q, Ren Z, Hu B. *Appl Catal B-Environ*, 2023, 326: 122398
287 Chen B, Zhang G, Chen L, Kang J, Wang Y, Chen S, Jin Y, Yan H, Xia C. *J Hazard Mater*, 2022, 426: 127851
288 Liang R, Luo J, Lin S, Li Z, Dong Z, Wu Y, Wang Y, Cao X, Meng

C, Yu F, Liu Y, Zhang Z. *Sep Purif Tech*, 2023, 312: 123291
289 Yu F, Zhu Z, Wang S, Peng Y, Xu Z, Tao Y, Xiong J, Fan Q, Luo F. *Chem Eng J*, 2021, 412: 127558
290 Yu F, Zhu Z, Wang S, Wang J, Xu Z, Song F, Dong Z, Zhang Z. *Appl Catal B-Environ*, 2022, 301: 120819
291 Wang X, Xu W, Cui WR. *J Hazard Mater*, 2024, 463: 132846
292 Huang M, Kan L, Zhao W, Wang Y, Xiong Y, Shan W, Lou Z. *Chem Eng J*, 2021, 421: 127763
293 Pearce CI, Moore RC, Morad JW, Asmussen RM, Chatterjee S, Lawter AR, Levitskaia TG, Neeway JJ, Qafoku NP, Rigali MJ, Saslow SA, Szecsody JE, Thallapally PK, Wang G, Freedman VL. *Sci Total Environ*, 2020, 716: 132849
294 Li J, Dai X, Zhu L, Xu C, Zhang D, Silver MA, Li P, Chen L, Li Y, Zuo D, Zhang H, Xiao C, Chen J, Diwu J, Farha OK, Albrecht-Schmitt TE, Chai Z, Wang S. *Nat Commun*, 2018, 9: 3007
295 Lee MS, Um W, Wang G, Kruger AA, Lukens WW, Rousseau R, Glezakou VA. *Nat Commun*, 2016, 7: 12067
296 Wu W, Liu X, Yang X, Xiao Q, Liu Y, Wang S, Wang XF. *Sep Purif Tech*, 2023, 318: 123951
297 Custelcean R. *Chem Commun*, 2013, 49: 2173–2182
298 Gu B, Brown GM, Bonnesen PV, Liang L, Moyer BA, Ober R, Alexandratos SD. *Environ Sci Technol*, 2000, 34: 1075–1080
299 Katayev EA, Kolesnikov GV, Sessler JL. *Chem Soc Rev*, 2009, 38: 1572–1586
300 Banerjee D, Kim D, Schweiger MJ, Kruger AA, Thallapally PK. *Chem Soc Rev*, 2016, 45: 2724–2739
301 Zhou S, Zhou X, Zhao P, Huang Y, Xu Y, Wu X, Chen S, Huang C, Jin Y, Zhang Y, Xia C. *Colloids Surfs A-Physicochem Eng Aspects*, 2024, 685: 133277
302 Sun Q, Zhu L, Aguila B, Thallapally PK, Xu C, Chen J, Wang S, Rogers D, Ma S. *Nat Commun*, 2019, 10: 1646
303 Yi SM, Zhang CR, Liu X, Jiang W, Liang RP, Qiu JD. *Mater Chem Phys*, 2023, 306: 128032
304 Zhou W, Li A, Zhou M, Xu Y, Zhang Y, He Q. *Nat Commun*, 2023, 14: 5388
305 Fajal S, Mandal W, Torris A, Majumder D, Let S, Sen A, Kanheerampockil F, Shirolkar MM, Ghosh SK. *Nat Commun*, 2024, 15: 1278
306 Da HJ, Yang CX, Yan XP. *Environ Sci Technol*, 2019, 53: 5212–5220
307 Zhao P, Zhou X, Huang Y, Xu Y, Chen S, Zheng C, Jin Y, Xia C. *Surfs Interfaces*, 2022, 29: 101788
308 Ding M, Chen L, Xu Y, Chen B, Ding J, Wu R, Huang C, He Y, Jin Y, Xia C. *Chem Eng J*, 2020, 380: 122581
309 Huang Y, Ding M, Ding J, Kang J, Yan Z, Zhao P, Zhou X, Jin Y, Chen S, Xia C. *Chem Eng J*, 2022, 435: 134785
310 Yuan L, Xu R, Yu H, Ji C, Lv L, Zhang W. *Chem Eng J*, 2023, 475: 146085
311 Qi JX, Zhang CR, Chen XJ, Yi SM, Niu CP, Liu JL, Zhang L, Liang RP, Qiu JD. *Anal Chem*, 2022, 94: 10850–10856
312 Roja A, Srividhya S, Arunachalam M. *Polymer*, 2024, 294: 126688
313 Xiong S, Tao J, Wang Y, Tang J, Liu C, Liu Q, Wang Y, Yu G, Pan C. *Chem Commun*, 2018, 54: 8450–8453
314 Li B, Wang B, Huang X, Dai L, Cui L, Li J, Jia X, Li C. *Angew Chem Int Ed*, 2019, 58: 3885–3889
315 Chen D, Ma T, Zhao X, Jing X, Zhao R, Zhu G. *ACS Appl Mater Interfaces*, 2022, 14: 47126–47135
316 Pearce EN, Caldwell KL. *Am J Clin Nutr*, 2016, 104: 898S–901S
317 Shen W, Fan W. *J Mater Chem A*, 2013, 1: 999–1013
318 Zhou H, Zhao B, Fu C, Wu Z, Wang C, Ding Y, Han BH, Hu A. *Macromolecules*, 2019, 52: 3935–3941
319 Liu M, Yao C, Liu C, Xu Y. *Sci Rep*, 2018, 8: 14071
320 Pourebrahimi S, Pirooz M, De Visscher A, Peslherbe GH. *J Environ Chem Eng*, 2022, 10: 107805
321 Wang J, Wu T, Wang X, Chen J, Fan M, Shi Z, Liu J, Xu L, Zang Y. *iScience*, 2024, 27: 108993
322 Wang J, Wang X, Deng Y, Wu T, Chen J, Liu J, Xu L, Zang Y. *Polymer*, 2023, 267: 125665
323 Zhang J, Shi W, Yang M, Huang K, Zhu Y, Xie Z. *Eur Polym J*, 2024, 205: 112724
324 Liu B, Mao C, Zhou Z, Wang Q, Zhou X, Liao Z, Deng R, Liu D, Beiyuan J, Lv D, Li J, Huang L, Chen X, Yuan W. *Int J Mol Sci*, 2023, 24: 370
325 Li X, Peng Y, Jia Q. *Sep Purif Tech*, 2020, 236: 116260
326 Zhao Y, Lu W, Zhang Y, Liu X, Sun B. *Microporous Mesoporous Mater*, 2024, 366: 112954
327 Xie L, Zheng Z, Lin Q, Zhou H, Ji X, Sessler JL, Wang H. *Angew Chem Int Ed*, 2022, 61: e202113724
328 Wang H, Qiu N, Kong X, Hu Z, Zhong F, Li Y, Tan H. . *ACS Appl Mater Interfaces*, 2023, 15: 14846–14853
329 Huan W, Huiping H, Qifan P. *Colloids Surfs A-Physicochem Eng Aspects*, 2021, 627: 127185
330 Niu TH, Feng CC, Yao C, Yang WY, Xu YH. *ACS Appl Polym Mater*, 2021, 3: 354–361
331 Naguib M, Mochalin VN, Barsoum MW, Gogotsi Y. *Adv Mater*, 2014, 26: 992–1005
332 Naguib M, Kurtoglu M, Presser V, Lu J, Niu J, Heon M, Hultman L, Gogotsi Y, Barsoum MW. *Adv Mater*, 2011, 23: 4248–4253
333 Ghidiu M, Lukatskaya MR, Zhao MQ, Gogotsi Y, Barsoum MW. *Nature*, 2014, 516: 78–81
334 Halim J, Lukatskaya MR, Cook KM, Lu J, Smith CR, Näslund LÅ, May SJ, Hultman L, Gogotsi Y, Eklund P, Barsoum MW. *Chem Mater*, 2014, 26: 2374–2381
335 Alhabeb M, Maleski K, Anasori B, Lelyukh P, Clark L, Sin S, Gogotsi Y. *Chem Mater*, 2017, 29: 7633–7644
336 Liew J, Liu L, Loh KH, Bashir S, Ramesh K, Ramesh S. *J Energy Storage*, 2024, 84: 110868
337 Liu F, Wang S, Hu B. *Chem Eng J*, 2023, 456: 141100
338 Liu F, Lou Y, Xia F, Hu B. *Chem Eng J*, 2023, 454: 140318
339 Peng C, Wei P, Chen X, Zhang Y, Zhu F, Cao Y, Wang H, Yu H, Peng F. *Ceramics Int*, 2018, 44: 18886–18893
340 Feng Y, Wang H, Xu J, Du X, Cheng X, Du Z, Wang H. *J Hazard Mater*, 2021, 416: 125777
341 He Z, Huang D, Yue G, Zhu J, Zhao P. *Appl Surf Sci*, 2021, 570: 150804
342 Liu F, Hu ZF, Xiang M, Hu B. *Appl Surf Sci*, 2022, 601: 154227
343 Shahzad A, Oh JM, Rasool K, Jang J, Kim B, Lee DS. *J Nucl Mater*, 2021, 549: 152916
344 Zhang P, Cao J, Yang Z, Wu Z, Wu L. *J Environ Chem Eng*, 2022, 10: 109019
345 Zhang P, Wang L, Yuan LY, Lan JH, Chai ZF, Shi WQ. *Chem Eng J*, 2019, 370: 1200–1209
346 Liu F, Luo Y, Hu B. *Sep Purif Tech*, 2023, 327: 124912
347 Shahzad A, Moztahida M, Tahir K, Kim B, Jeon H, Ghani AA, Maile N, Jang J, Lee DS. *J Nucl Mater*, 2020, 539: 152277
348 Nezami S, Ghaemi A, Yousefi T. *J Environ Chem Eng*, 2024, 12: 112491
349 Wang H, Shao Y, Mei S, Lu Y, Zhang M, Sun J, Matyjaszewski K, Antonietti M, Yuan J. *Chem Rev*, 2020, 120: 9363–9419
350 Singh G, Lakhi KS, Sil S, Bhosale SV, Kim IY, Albahily K, Vinu A. *Carbon*, 2019, 148: 164–186
351 Liu Y, Ouyang Y, Huang D, Jiang C, Liu X, Wang Y, Dai Y, Yuan D, Chew JW. *Sci Total Environ*, 2020, 706: 136019
352 Sun Y, Zhang H, Yuan N, Ge Y, Dai Y, Yang Z, Lu L. *J Hazard Mater*, 2021, 413: 125282
353 Wang R, Li M, Liu T, Li X, Zhou L, Tang L, Gong C, Gong X, Yu K, Li N, Zhu W, Chen T. *J Cleaner Production*, 2022, 364: 132654
354 Liu Q, Wang N, Xie B, Xiao D. *Sep Purif Tech*, 2023, 308: 122866
355 Dong Z, Zhang Z, Zhou R, Dong Y, Dai Y, Cao X, Wang Y, Liu Y. *Chem Eng J*, 2020, 386: 123944
356 Pavlenko V, Khosravi H S, Żółtowska S, Haruna AB, Zahid M, Mansurov Z, Supiyeva Z, Galal A, Ozoemena KI, Abbas Q, Jesionowski T. *Mater Sci Eng-R-Rep*, 2022, 149: 100682
357 Zheng B, Lin X, Zhang X, Wu D, Matyjaszewski K. *Adv Funct Mater*, 2020, 30: 1907006

358 Li L, Ma R, Wen T, Gu P, Zhang S, Zheng M, Wu X, Zhang X, Hayat T, Wang X. *Sci Total Environ*, 2019, 694: 133697
359 Chen D, Li Y, Zhao X, Shi M, Shi X, Zhao R, Zhu G. *ACS Cent Sci*, 2023, 9: 2326–2332
360 Lai P, Zhou H, Niu Z, Li L, Zhu W, Dai L. *Chem Eng J*, 2023, 457: 141255
361 Liu X, Xie Y, Hao M, Chen Z, Yang H, Waterhouse GIN, Ma S, Wang X. *Adv Sci*, 2022, 9: 2201735
362 Lv Z, Zhang J, Zhang Y, Li K, Ye X, Fang M, Tan X, Kong M, Wang X. *Sep Purif Tech*, 2022, 285: 120366
363 Yu Z, Li Q, Liao J, Zhang Y, Zhang L, Zhu W. *J Alloys Compd*, 2021, 868: 159069
364 Li M, Liu H, Chen T, Chen D, Wang C, Wei L, Wang L. *Sci Total Environ*, 2020, 703: 135604
365 Jin M, Huang X, Wang Z, Chan V, Hu J, Wu A, Hu G. *Chemosphere*, 2023, 342: 140190
366 Huang J, Liu Z, Huang D, Jin T, Qian Y. *J Hazard Mater*, 2022, 433: 128775
367 Yu H, Zhou L, Liu Y, Ao X, Ouyang J, Liu Z, Adesina AA. *Desalination*, 2023, 564: 116773
368 Zhang S, Yang F, Cao X, Tang Y, Yin T, Bo T, Liu Y, Lisak G, Kano N, Na B, Chang M, Liu Y. *J Hazard Mater*, 2023, 459: 132112
369 Zhou J, Zhou H, Zhang Y, Wu J, Zhang H, Wang G, Li J. *Chem Eng J*, 2020, 398: 125460
370 Li S, Yang X, Cui Z, Xu Y, Niu Z, Li P, Pan D, Wu W. *Appl Catal B-Environ*, 2021, 298: 120625
371 Wan H, Li Y, Wang M, Zhao Q, Fu Y, Chen Y, He P, Wu L, Meng Q, Ma T, Yang J, Duan T. *Chem Eng J*, 2022, 430: 133139
372 Liu T, Zhang X, Wang H, Chen M, Yuan Y, Zhang R, Xie Z, Liu Y, Zhang H, Wang N. *Chem Eng J*, 2021, 412: 128700
373 Dong Z, Li Z, Zeng D, Cheng Z, Wang Y, Dai Y, Cao X, Wang Y, Zhang Z, Liu Y. *Sep Purif Tech*, 2023, 304: 122255
374 Palansooriya KN, Yoon IH, Kim SM, Wang CH, Kwon H, Lee SH, Igalavithana AD, Mukhopadhyay R, Sarkar B, Ok YS. *Environ Res*, 2022, 214: 114072
375 Hasan MN, Shenashen MA, Hasan MM, Znad H, Awual MR. *Chemosphere*, 2021, 270: 128668
376 Feng S, Cao X, Zheng W, Yue X, Li X, Li S, Wang X, Feng S. *J Environ Chem Eng*, 2022, 10: 107972
377 Liu F, Wang S, Zhao C, Hu B. *Biochar*, 2023, 5: 31
378 Park JH, Kim H, Kim M, Lim JM, Ryu J, Kim S. *Chem Eng J*, 2020, 399: 125817
379 Kim M, Eun S, Ryu J, Kim S. *J Hazard Mater*, 2023, 443: 130215
380 Xiang S, Mao H, Geng W, Xu Y, Zhou H. *J Hazard Mater*, 2022, 431: 128591
381 Wang W, Liu S, Zhou Y, Luo J, Shi J, Zhou Z, Ma J. *Sep Purif Tech*, 2021, 276: 119235
382 Rong Y, Li S, Niu J, Wang Z, Hao X, Song C, Wang T, Guan G. *Sep Purif Tech*, 2021, 274: 119056
383 Liu X, Xie Y, Li Y, Hao M, Chen Z, Yang H, Waterhouse GIN, Ma S, Wang X. *Adv Sci*, 2023, 10: 2303536
384 Guo Z, Shams M, Zhu C, Shi Q, Tian Y, Engelhard MH, Du D, Chowdhury I, Lin Y. *Environ Sci Technol*, 2019, 53: 2612–2617
385 Ma Z, Han Y, Qi J, Qu Z, Wang X. *Industrial Crops Products*, 2021, 169: 113649
386 Wu Y, Guo Y, Su R, Ma X, Wu Q, Zeng Z, Li L, Yao X, Wang S. *Sep Purif Tech*, 2022, 303: 122237
387 Baskaran K, Ali M, Riley BJ, Zharov I, Carlson K. *ACS Mater Lett*, 2022, 4: 1780–1786
388 Chen X, Wang L, Ding C, Xie H, Zou H, Deng J, Liu Z, Shi J, Ding Y. *Appl Surf Sci*, 2024, 643: 158644
389 Bhakare MA, Lokhande KD, Dhumal PS, Bondarde MP, Some S. *Sep Purif Tech*, 2021, 278: 119490
390 Wang R, Dong H, Li X, Zhou L, Zhu W, Chen T. *Chem Eng J*, 2023, 478: 147331
391 Shin J, Kwak J, Lee YG, Kim S, Son C, Cho KH, Lee SH, Park Y, Ren X, Chon K. *Environ Res*, 2021, 199: 111346
392 Tarcan R, Todor-Boer O, Petrovai I, Leordean C, Astilean S, Botiz I. *J Mater Chem C*, 2020, 8: 1198–1224
393 Gupta NK, Choudhary BC, Gupta A, Achary SN, Sengupta A. *J Mol Liq*, 2019, 289: 111121
394 Agarwal V, Zetterlund PB. *Chem Eng J*, 2021, 405: 127018
395 Zhang P, Chen Y, Weng H, Muroya Y, Yamashita S, Zhao Y, Lin M. *J Mater Chem A*, 2023, 11: 2804–2813
396 Liang J, Zhang X, Liu T, Gao X, Liang W, Qi W, Qian L, Li Z, Chen X. *Adv Mater*, 2022, 34: 2206524
397 Guo S, Garaj S, Bianco A, Ménard-Moyon C. *Nat Rev Phys*, 2022, 4: 247–262
398 Guo S, Nishina Y, Bianco A, Ménard-Moyon C. *Angew Chem Int Ed*, 2020, 59: 1542–1547
399 Siklitskaya A, Gacka E, Larowska D, Mazurkiewicz-Pawlicka M, Malolepszy A, Stobiński L, Marciniak B, Lewandowska-Andrałojć A, Kubas A. *Sci Rep*, 2021, 11: 7977
400 Hong J, Park SJ, Kim S. *Electrochim Acta*, 2019, 311: 62–71
401 Tang X, Zhou L, Yu H, Dai Y, Ouyang J, Liu Z, Wang Y, Le Z, Adesina AA. *Sep Purif Tech*, 2021, 278: 119604
402 Huo J, Yu G, Wang J. *J Hazard Mater*, 2021, 411: 125117
403 Sun Y, Chen M, Liu H, Zhu Y, Wang D, Yan M. *Appl Surf Sci*, 2020, 525: 146614
404 Inonu Z, Keskin S, Erkey C. *ACS Appl Nano Mater*, 2018, 1: 5959–5980
405 Zhao M, Tesfay Reda A, Zhang D. *ACS Omega*, 2020, 5: 8012–8022
406 Li N, Yang L, Wang D, Tang C, Deng W, Wang Z. *Environ Sci Technol*, 2021, 55: 9181–9188
407 Li T, Lin X, Zhang Z, Yang L, Qian Y, Fu L, Zhou S, Chen W, Wang Q, Li X, Kong X-, Xiao H, Jiang L, Wen L. *Adv Funct Mater*, 2023, 33: 2212819
408 Liu X, Sun J, Xu X, Alsaedi A, Hayat T, Li J. *Chem Eng J*, 2019, 360: 941–950
409 Wang Y, Liu Y, Hu X, Li Y, Tu H, Wang C, Liu Y, Yuan D. *J Mol Liq*, 2021, 323: 114639
410 Gao Y, Chen K, Ren X, Alsaedi A, Hayat T, Chen C. *Environ Sci Technol*, 2018, 52: 12208–12215
411 Wang Z, Liu H, Lei Z, Huang L, Wu T, Liu S, Ye G, Lu Y, Wang X. *Chem Eng J*, 2020, 402: 126256
412 Joshi RK, Alwarappan S, Yoshimura M, Sahajwalla V, Nishina Y. *Appl Mater Today*, 2015, 1: 1–12
413 Lei Z, Christov N, Zhao XS. *Energy Environ Sci*, 2011, 4: 1866–1873
414 Gao Y, Qin Y, Zhang M, Xu L, Yang Z, Xu Z, Wang Y, Men M. *J Hazard Mater*, 2022, 436: 129148
415 Sreenivasan R, Suma Mahesh S, Sumi VS. *Sep Purif Tech*, 2019, 54: 1453–1468
416 Huang ZW, Li ZJ, Zheng LR, Wu WS, Chai ZF, Shi WQ. *Environ Pollut*, 2019, 248: 82–89
417 Shahr El-Din AM, Monir T, Borai EH. *J Polym Environ*, 2021, 29: 3721–3731
418 Lee I, Kang SM, Jang SC, Lee GW, Shim HE, Rethinasabapathy M, Roh C, Huh YS. *J Mater Chem A*, 2019, 7: 1737–1748
419 Zhang Y, Wang H, Gao K, Huang D, Hou L', Yang Y. *Sci Total Environ*, 2022, 838: 156530
420 Wang K, Yan Z, Fu L, Li D, Gong L, Wang Y, Xiong Y. *Sep Purif Tech*, 2022, 302: 122073
421 Zhang H, Yang F, Lu C, Du C, Bai R, Zeng X, Zhao Z, Cai C, Li J. *Environ Chem Lett*, 2020, 18: 1379–1388
422 Muhire C, Tesfay Reda A, Zhang D, Xu X, Cui C. *Chem Eng J*, 2022, 431: 133816
423 Chen L, Cui R, Dai J, Wang Y, Pan J. *Sep Purif Tech*, 2024, 333: 125955
424 Lei Y, Zhang G, Zhang Q, Yu L, Li H, Yu H, He Y. *Nat Commun*, 2021, 12: 4483
425 Fan K, Li LF, Li JJ. *High Energy Chem*, 2021, 55: 140–144
426 Liu B, Ren X, Chen L, Ma X, Chen Q, Sun Q, Zhang L, Si P, Ci L. *J Hazard Mater*, 2019, 373: 705–715

427 Wang Z, Huang L, Dong X, Wu T, Qing Q, Chen J, Lu Y, Xu C. *Nat Commun*, 2023, 14: 261
428 Veliscek-Carolan J. *J Hazard Mater*, 2016, 318: 266–281
429 Ali I, Zakharchenko EA, Myasoedova GV, Molochnikova NP, Rodionova AA, Baulin VE, Burakov AE, Burakova IV, Babkin AV, Neskoromnaya EA, Melezhik AV, Tkachev AG, Habila MA, El-Marghany A, Sheikh M, Ghfar A. *J Mol Liq*, 2021, 335: 116260
430 Pei H, Yan F, Liu H, He B, Li J. *Sep Purif Tech*, 2024, 341: 126857
431 Kim JY, Oh H, Moon HR. *Adv Mater*, 2019, 31: 1805293
432 Liu H, Zhang X, Lv Z, Wei F, Liang Q, Qian L, Li Z, Chen X, Wu W. *JACS Au*, 2023, 3: 3089–3100
433 Boulanger N, Kuzenkova AS, Iakunkov A, Romanchuk AY, Trigub AL, Egorov AV, Bauters S, Amidani L, Retegan M, Kvashnina KO, Kalmykov SN, Talyzin AV. *ACS Appl Mater Interfaces*, 2020, 12: 45122–45135
434 Wu L, Yang X, Chen T, Li Y, Meng Q, Zhu L, Zhu W, He R, Duan T. *Chem Eng J*, 2022, 427: 131773
435 Chee TS, Lee S, Ng WJ, Akmal M, Ryu HJ. *ACS Appl Mater Interfaces*, 2023, 15: 40438–40450
436 Wang X, Yu S, Jin J, Wang H, Alharbi NS, Alsaedi A, Hayat T, Wang X. *Sci Bull*, 2016, 61: 1583–1593
437 Xu L, Wang J. *Crit Rev Environ Sci Tech*, 2017, 47: 1042–1105
438 Yang L, Peng Y, Luo X, Dan Y, Ye J, Zhou Y, Zou Z. *Chem Soc Rev*, 2021, 50: 2147–2172
439 Zhang XY, Wang JJ, Li P, Tan ZY, Zeng JH, He YR, Habibul N. *Chem Eng J*, 2022, 428: 131209
440 Lu C, Zhang P, Jiang S, Wu X, Song S, Zhu M, Lou Z, Li Z, Liu F, Liu Y, Wang Y, Le Z. *Appl Catal B-Environ*, 2017, 200: 378–385
441 Ong WJ, Tan LL, Ng YH, Yong ST, Chai SP. *Chem Rev*, 2016, 116: 7159–7329
442 Yu J, Zhang H, Liu Q, Yu J, Zhu J, Li R, Liu P, Li Y, Wang J. *Chem Eng J*, 2023, 471: 144705
443 Gao H, Xu J, Zhou J, Zhang S, Zhou R. *J Colloid Interface Sci*, 2020, 570: 125–134
444 Li Y, Shi L, Mao Y, Zhang Y, Wang H. *Chem Eng J*, 2022, 446: 136872
445 Li P, Wang Y, Wang J, Dong L, Zhang W, Lu Z, Liang J, Pan D, Fan Q. *Chem Eng J*, 2021, 414: 128810
446 Jiang XH, Xing QJ, Luo XB, Li F, Zou JP, Liu SS, Li X, Wang XK. *Appl Catal B-Environ*, 2018, 228: 29–38
447 Chen T, Yu K, Dong C, Yuan X, Gong X, Lian J, Cao X, Li M, Zhou L, Hu B, He R, Zhu W, Wang X. *Coord Chem Rev*, 2022, 467: 214615
448 Chen T, Liu T, Pang B, Ding T, Zhang W, Shen X, Wu D, Wang L, Liu X, Luo Q, Zhu W, Yao T. *Sci Bull*, 2022, 67: 2001–2012
449 Chen L, Gao Y, Lian J, Li L, Ding D, Dai Z. *Sep Purif Tech*, 2023, 307: 122873
450 Nie Y, Zhu Y, Lu X, Qiu J, Wang B, Xie Z, Le Z. *Chem Eng J*, 2023, 477: 146908
451 Liu S, Wang Z, Lu Y, Li H, Chen X, Wei G, Wu T, Maguire DJ, Ye G, Chen J. *Appl Catal B-Environ*, 2021, 282: 119523
452 Wang J, Li P, Wang Y, Liu Z, Wang D, Liang J, Fan Q. *Adv Sci*, 2023, 10: 2205542
453 Yu K, Li Y, Cao X, Wang R, Zhou L, Wu L, He N, Lei J, Fu D, Chen T, He R, Zhu W. *J Hazard Mater*, 2023, 460: 132356
454 Dong Z, Hu S, Li Z, Xu J, Gao D, Yu F, Li X, Cao X, Wang Y, Zhang Z, Liu Y, Wang X. *Small*, 2023, 19: 2300003
455 Meng Q, Yang X, Wu L, Chen T, Li Y, He R, Zhu W, Zhu L, Duan T. *J Hazard Mater*, 2022, 422: 126912
456 Li P, Wang J, Wang Y, Dong L, Wang W, Geng R, Ding Z, Luo D, Pan D, Liang J, Fan Q. *Chem Eng J*, 2021, 425: 131552
457 Zhang Y, Sun H, Gao F, Zhang S, Han Q, Li J, Fang M, Cai Y, Hu B, Tan X, Wang X. *Research*, 2022, 2022: 9790320
458 Dai Z, Zhen Y, Sun Y, Li L, Ding D. *Chem Eng J*, 2021, 415: 129002
459 Chen T, Zhang J, Ge H, Li M, Li Y, liu B, Duan T, He R, Zhu W. *J Hazard Mater*, 2020, 384: 121383
460 He F, Xiao Q, Chen Y, Wang H, Wang X. *Appl Catal B-Environ*, 2024, 343: 123525
461 Huang X, Xiao J, Mei P, Wang H, Ishag A, Sun Y. *Catal Lett*, 2022, 152: 1981–1989
462 Guo Q, Zhou C, Ma Z, Ren Z, Fan H, Yang X. *Annu Rev Phys Chem*, 2018, 69: 451–472
463 Nosaka Y, Nosaka AY. *Chem Rev*, 2017, 117: 11302–11336
464 Hamza MF, Guibal E, Wei Y, Ning S. *Chem Eng J*, 2023, 464: 142638
465 Gomaa H, Emran MY, Elsenety MM, Abdel-Rahim RD, Deng Q, Gadallah MI, Saad M, ALMohiy H, Ali HRH, Faraghally FA, Seaf El-Nasr TA, El-Gaby MSA, Aboraia AM. *J Water Process Eng*, 2023, 51: 103436
466 Wei X, Pan Y, Li M, Linghu W, Guo X. *Res Chem Intermed*, 2023, 49: 2691–2704
467 Liao Q, Zou D, Pan W, Linghu W, Shen R, Li X, Asiri AM, Alamry KA, Sheng G, Zhan L, Wu X. *J Mol Liq*, 2018, 252: 351–361
468 Huang Y, Zheng H, Li H, Zhang Z, zhao C, Gou Q, Liu Y. *Chem Eng J*, 2021, 410: 128321
469 Chen Z, Zhang S, Liu Y, Alharbi NS, Rabah SO, Wang S, Wang X. *Sci Total Environ*, 2020, 731: 139054
470 Yussuf NM, Ismail AF, Mohamed NA, Mat Teridi MA. *Mater Lett*, 2024, 357: 135771
471 Yussuf NM, Ismail AF, Aziman ES, Mohamed NA, Teridi MAM. *Sep Purif Tech*, 2024, 330: 125205
472 Nepal D, Kang S, Adstedt KM, Kanhaiya K, Bockstaller MR, Brinson LC, Buehler MJ, Coveney PV, Dayal K, El-Awady JA, Henderson LC, Kaplan DL, Keten S, Kotov NA, Schatz GC, Vignolini S, Vollrath F, Wang Y, Yakobson BI, Tsukruk VV, Heinz H. *Nat Mater*, 2023, 22: 18–35
473 Sun Q, Aguila B, Perman J, Ivanov AS, Bryantsev VS, Earl LD, Abney CW, Wojtas L, Ma S. . *Nat Commun*, 2018, 9: 1644
474 Yu Q, Yuan Y, Feng L, Feng T, Sun W, Wang N. *Angew Chem Int Ed*, 2020, 59: 15997–16001
475 Yu Q, Yuan Y, Feng L, Sun W, Lin K, Zhang J, Zhang Y, Wang H, Wang N, Peng Q. *J Hazard Mater*, 2022, 424: 127758
476 Yuan Y, Yu Q, Wen J, Li C, Guo Z, Wang X, Wang N. *Angew Chem Int Ed*, 2019, 58: 11785–11790
477 Prince E, Kumacheva E. *Nat Rev Mater*, 2019, 4: 99–115
478 Chen H, Guo J, Wang Y, Dong W, Zhao Y, Sun L. *Adv Sci*, 2022, 9: 2202038
479 Yuan Y, Liu T, Xiao J, Yu Q, Feng L, Niu B, Feng S, Zhang J, Wang N. *Nat Commun*, 2020, 11: 5708
480 Li L, Kang K, Chee T-, Tian Z, Sun Q, Xiao C. *Adv Sci*, 2024, 11: 2308663
481 Yu W, Wei C, Zhang K, Zhang J, Ge Z, Liang X, Guiver MD, Ge X, Wu L, Xu T. *Environ Sci Technol*, 2023, 57: 5861–5871
482 Yu F, Yu S, Li C, Li Z, Song F, Xu Z, Zhu Y, Dai C, Cao X, Zhang Z, Liu Y, Qiu J. *Chem Eng J*, 2023, 466: 143285
483 Xu X, Ray R, Gu Y, Ploehn HJ, Gearheart L, Raker K, Scrivens WA. *J Am Chem Soc*, 2004, 126: 12736–12737
484 Lim SY, Shen W, Gao Z. *Chem Soc Rev*, 2015, 44: 362–381
485 Wang Z, Xu C, Lu Y, Chen X, Yuan H, Wei G, Ye G, Chen J. *Sens Actuat B-Chem*, 2017, 241: 1324–1330
486 Wang Z, Xie Y, Lei Z, Lu Y, Wei G, Liu S, Xu C, Zhang Z, Wang X, Rao L, Chen J. *Anal Chem*, 2019, 91: 9690–9697
487 Giordano MG, Seganti G, Bartoli M, Tagliaferro A. *Molecules*, 2023, 28: 2772
488 Wang Z, Lu Y, Yuan H, Ren Z, Xu C, Chen J. *Nanoscale*, 2015, 7: 20743–20748
489 Wang Z, Xu C, Lu Y, Wei G, Ye G, Sun T, Chen J. *Chem Eng J*, 2018, 344: 480–486
490 Zhang Z, Zhang D, Shi C, Liu W, Chen L, Miao Y, Diwu J, Li J, Wang S. *Environ Sci-Nano*, 2019, 6: 1457–1465
491 Shilpa AS, Thangadurai TD, Bhalerao GM, Maji S. *Talanta*, 2024, 272: 125783
492 Gong WJ, Nan HR, Peng HB, Wang YQ, Dong ZM, Zhang ZB, Cao XH, Liu YH. *MicroChem J*, 2023, 190: 108725

493 Wang D, Zhang LJ, Liu MH, Du FF, Shen ZY, He L, Wang LL. *J Hazard Mater*, 2023, 454: 131497
494 Wang Q, Zhang H, Yu D, Qin W, Wu X. *Carbon*, 2022, 198: 162–170
495 Wang Z, Xu C, Lu Y, Wu F, Ye G, Wei G, Sun T, Chen J. *ACS Appl Mater Interfaces*, 2017, 9: 7392–7398
496 Guo X, Liu Q, Liu J, Zhang H, Yu J, Chen R, Song D, Li R, Wang J. *Appl Surf Sci*, 2019, 491: 640–649
497 Pan N, Tang J, Hou D, Lei H, Zhou D, Ding J. *Chem Eng J*, 2021, 423: 130267
498 Wang Y, Zhang Y, Liu X, Sun S, Qin S, Huang J, Chen B. *Dalton Trans*, 2023, 52: 12296–12307
499 Tharwat RM, Mahmoud ME, Abdelfattah AM, Hassan SSM. *J Mol Liq*, 2023, 390: 122960
500 Mahmoud ME, Tharwat RM, Abdelfattah AM, Hassan SSM. *J Environ Chem Eng*, 2023, 11: 110497
501 Zhou Q, Jin B, Zhao P, Chu S, Peng R. *Chem Eng J*, 2021, 419: 129622
502 Dai Z, Zhao S, Lian J, Li L, Ding D. *Sep Purif Tech*, 2022, 298: 121590
503 Liu J, Zhang Z, Dong Z, Zhu X, Gao D, Cheng Z, Cao X, Wang Y, Liu Y. *J Radioanal Nucl Chem*, 2022, 331: 2093–2104
504 Li H, Qing Q, Zheng L, Xie L, Gan Z, Huang L, Liu S, Wang Z, Lu Y, Chen J. *Chin Chem Lett*, 2022, 33: 3573–3576
505 Zheng B, Liu X, Hu J, Wang F, Hu X, Zhu Y, Lv X, Du J, Xiao D. *J Hazard Mater*, 2019, 368: 81–89
506 Choi MR, Lee B. *Optical Mater*, 2022, 134: 113190
507 Eckerman K, Harrison J, Menzel HG, Clement CH. *Ann ICRP*, 2013, 42: 1–130
508 Osytek KM, Blower PJ, Costa IM, Smith GE, Abbate V, Terry SYA. *EJNMMI Res*, 2021, 11: 63
509 Kumar S, Fathima E, Khanum F, Malini SS. *Int J Radiat Biol*, 2023, 99: 459–473
510 Miousse IR, Kutanzi KR, Koturbash I. *Int J Radiat Biol*, 2017, 93: 457–469
511 Mohan S, Chopra V. *Chapter 18: Biological Effects of Radiation*. Amsterdam: Elsevier, 2022. 485–508
512 Eckerman K, Endo A. *Ann ICRP*, 2008, 38: 7–96
513 Mc Farlane JC, Beckert WF, Brown KW. *J Env Qual*, 1979, 8: 269–276
514 Carsten AL, Brooks A, Commerford SL, Cronkite EP. Genetic and somatic effects in animals maintained on tritiated water. Upton: Brookhaven National Laboratory, 1981
515 Li S, Zhang Y, Xue H, Zhang Q, Chen N, Wan J, Sun L, Chen Q, Zong Y, Zhuang F, Gu P, Zhang A, Cui F, Tu Y. *Ecotoxicol Environ Saf*, 2021, 225: 112770
516 Arcanjo C, Frelon S, Armant O, Camoin L, Audebert S, Camilleri V, Cavalié I, Adam-Guillermin C, Gagnaire B. *J Environ Radioact*, 2023, 261: 107141
517 Hagger JA, Atienzar FA, Jha AN. *Aquat Toxicol*, 2005, 74: 205–217
518 Kim SB, Shultz C, Stuart M, Festarini A. *Appl Radiat Isotopes*, 2015, 98: 96–102
519 Dallas LJ, Devos A, Fievet B, Turner A, Lyons BP, Jha AN. *J Environ Radioact*, 2016, 155-156: 1–6
520 Baiocco G, George I, Garcia-Argote S, Guardamagna I, Lonati L, Lamartinière Y, Orsière T, Rousseau B, Ottolenghi A, Jha A, Lebaron-Jacobs L, Grisolia C, Malard V. *Radiat Res*, 2020, 195: 265–274
521 Festarini A, Shultz C, Stuart M, Kim SB, Ferreri C. *Appl Radiat Isotopes*, 2019, 151: 217–225
522 Beaton ED, Gosselin I, Festarini A, Gagnaire B, Farrow F, Cavalié I, Shultz C, Kim SB, Walsh S, Chen HQ, Adam-Guillermin C, Stuart M. *Sci Total Environ*, 2019, 662: 990–1002
523 Synzynys BI, Momot OA, Mirzeabasov OA, Zemnova AV, Lyapunova ER, Glushkov YM, Oudalova AA. *KEG*, 2018, 3: 249–260
524 Kim SB, Baglan N, Davis PA. *J Environ Radioact*, 2013, 126: 83–91
525 Diabate S, Strack S. *Health Phys*, 1993, 65: 698–712
526 Bertho JM, Kereselidze D, Manens L, Culeux C, Magneron V, Surette J, Blimkie M, Bertrand L, Wyatt H, Souidi M, Dublineau I, Priest N, Jourdain JR. *Sci Rep*, 2019, 9: 19919
527 Yim MS, Caron F. *Prog Nucl Energy*, 2006, 48: 2–36
528 Nóbrega C, Marques H, Moreira T. *Physiol Plantarum*, 2020, 168: 725–735
529 Li H, Yin Y, Liu J, Lu B, Wan H, Yang L, Wang W, Li R. *J Radiat Res*, 2020, 62: 34–45
530 Shipley RA, Gibbons AP. *Can J Physiol Pharmacol*, 1975, 53: 895–902
531 Krisch RE. *Int J Radiat Biol Relat Studies Phys Chem Med*, 1976, 29: 249–254
532 Purdom CE. *Mutat Res Fundamental Mol Mech Mutagenesis*, 1965, 2: 156–167
533 Brues AM, Buchanan DL. Summary of conference on the toxicity of carbon 14 held at argonne national laboratory, Argonne National Laboratory, Illinois, 1952
534 Sassi M, Carter DJ, Uberuaga BP, Stanek CR, Marks NA. *Biochim Biophys Acta Gen Subj*, 2014, 1840: 526–534
535 Lloyd RD, Mays CW, Atherton DR. *Health Phys*, 1976, 30: 183–189
536 Amata R, Diamond GL, Dorsey A, Fransen ME. Toxicological profile for strontium. Technic Report. Atlanta: U.S. Department of Health and Human Services, 2004,
537 Akleyev AV, Kossenko MM, Silkina LA, Degteva MO, Yachmenyov VA, Awa A, Akiyama M, Veremeyeva GA, Vozilova AV, Kyozumi S*et al.*. *Stem cells*, 1995, 13: 58–68
538 Negri AE, Fernández Niello JO, Wallner A, Arazi A, Steier P. *Nucl Instruments Methods Phys Res Sect B-Beam Interact Mater Atoms*, 2013, 294: 652–655
539 Jabbar T, Wallner G, Steier P, Katzlberger C, Kandler N. *J Environ Radioact*, 2012, 112: 90–95
540 Hou X, Hansen V, Aldahan A, Possnert G, Lind OC, Lujaniene G. *Anal Chim Acta*, 2009, 632: 181–196
541 Sheppard SC, Evenden WG. *J Environ Radioact*, 1995, 27: 99–116
542 Church BW, Brooks AL. *Int J Radiat Biol*, 2020, 96: 520–531
543 Fischer T. *Med Phys*, 2008, 35: 805
544 Olsvik PA, Heier LS, Rosseland BO, Teien HC, Salbu B. *J Environ Radioact*, 2010, 101: 230–236
545 Simon O, Massarin S, Coppin F, Hinton TG, Gilbin R. *J Environ Radioact*, 2011, 102: 1039–1044
546 Gilbin R, Alonzo F, Garnier-Laplace J. *J Environ Radioact*, 2008, 99: 134–145
547 Jarvis RB, Knowles JF. *Mutat Res Genet Toxicol Environ Mutagenesis*, 2003, 541: 63–69
548 Pendleton RC, Mays CW, Lloyd RD, Church BW. *Health Phys*, 1965, 11: 1503–1510
549 Rosoff B, Cohn SH, Spencer H. *Radiat Res*, 1963, 19: 643–654
550 Boecker BB. . *Health Phys*, 1969, 16: 785–788
551 Manzanares-Acuña E, Vega-Carrillo HR, Letechipia de Leon C, Hernandez-Davila VM, Mercado GA. *Epidemiology*, 2008, 19: S222